Development of a Scaled Doubly-Fed Induction Generator for Assessment of Wind Power Integration Issues

Prepared by:

Name: **Hossein Dehnavifard**

Student Number: **dhnhos001**

Supervised by:

A/Prof Azeem Khan

Co-supervisor:

A/Prof Paul Barendse

Thesis submitted to the Department of Electrical Engineering, University of Cape Town, in complete fulfilment of the requirements for the degree of Doctor of Philosophy

November 2016

Department of Electrical Engineering

Faculty of Engineering & the Built Environment

University of Cape Town

Declaration

This dissertation is submitted to the Department of Electrical Engineering, University of Cape Town, in complete fulfilment of the requirements for the degree of Doctor of Philosophy. It has not been submitted before for any degree or examination at this or any other university. The author confirms that this thesis is based on his own work, save for which is duly referenced. Portions of this work have been published in peer reviewed journals and at referred international conference proceedings.

Acknowledgements

The research in this thesis would have taken far longer to complete without the encouragement from many others. It is a delight to acknowledge those who have supported me over the last four years.

I wish to thank my parents for their love and encouragement, without whom I would never have enjoyed so many opportunities.

I would like to thank my supervisor, Prof Mohamed A. Khan, for his guidance and relaxed, thoughtful insight and also would like to thank my co-supervisor, Prof Paul Barendse, for his support.

The days would have passed far more slowly without the support of my friends, at the machine's lab, whom I thank for putting up with my idiosyncrasies and for providing such a rich source of conversation, education and entertainment.

I am thankful for the technical support of Mr. Chris Wozniak and Mr. Philip Titus during my experimental tests in the machine's lab.

Abstract

Years of experience have been dedicated to the advancement of thermal power plant technology, and in the last decade the investigation has focused on the wind energy conversion system (WECS). Wind energy will play an important role in the future of the energy market, due to the changing climate and the fossil fuel crisis. Initially, wind energy was intended to cover a small portion of the energy market, but in the long term it should compete with conventional fossil fuel power generation.

The movement of the power system towards this new phenomena has to be investigated before the wind energy share increases in the network. Therefore, the wind energy integration issues serve as an interesting topic for authors to improve the perception of integration, distribution, variability and power flow issues. Several simulation models have been introduced in order to resolve this issue, however, the variety in types of wind turbines and the network policies result in these models having limited accuracy or being developed for specific issues. The micro-machine is introduced in order to overcome the challenges of simulation models and the costs involved in field tests. In the past, the grid integration issue of large turbo-alternators was solved by the micro-machines. A variety of tests are possible with the micro-machines and they also increase the flexibility of the system. The increased accuracy as well as the ability to carry out real-time analysis and compare actual field test data are strengths worth utilizing.

This project involves the designing and the prototyping of a scaled doubly-fed induction generator (micro-DFIG). The machine is also analysed and tested. The scaling of the micro-machine is achieved by means of a dimensional analysis, which is a mathematical method that allows machines and systems to be down-scaled by establishing laws of similitude between the reference model and its scaled model. MATLAB/SIMULINK, Maxwell and Solid Work are employed to achieve the objectives of this project.

Table of Contents

List of Figures

List of Tables

1. Introduction

When a large scale of wind energy joins the grid, the main concern is to investigate integration, distribution, transmission and power flow issues. Currently, digital computing simulations are usually employed to research the above issues and have improved in terms of computation speed and accuracy by employing advanced computers. Although the computers are advanced, dynamic models are still required to be simplified in order to maintain the balance between time, volume, and accuracy of the simulations. The current power system models are too immature to investigate the above problems, therefore, alternative methods are required. This thesis is in effort to find better solutions for the wind energy challenges within the power system by employing micro-machines.

1.1 The Wind Energy Conversion System Structure

A wind farm produces power by means of several interconnected wind turbines which are located in a region with favourable wind conditions. The steady-state and dynamic behaviour of a wind farm is determined by the aggregated characteristic responses of individual wind turbines. A wind energy conversion system (WECS) structure is illustrated to present a clear image of the source of dynamic behaviour of wind power [1], [2]. The typical design of a wind turbine is a horizontal axis wind turbine. All components of this type of wind turbine are shown in figure 1.1 and are presented as follows.

1.1.1 Tower and Foundation

The generator, gearbox, etc. are located on the tower and its foundation. The free-standing type using steel tubes, lattice towers, and concrete towers is the common design currently in use. The properties of the wind farm are important when selecting the type of tower. The minimum height of the tower is 20m, however, it is usually 1 to 1.5 times the rotor diameter. The tower stiffness must be considered in the design of the wind turbine in order to minimize the vibrations between the rotor and the tower.

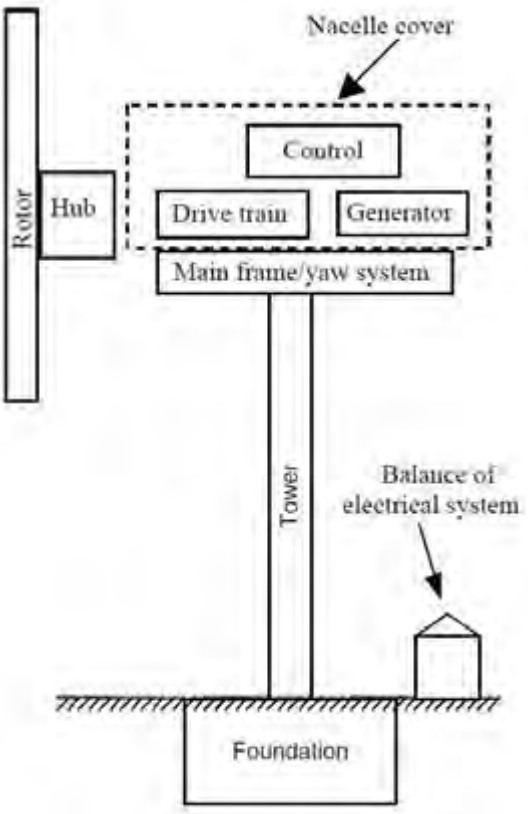

Fig. 1.1 Wind turbine components.

1.1.2 The Rotor

The wind turbine expenses and performance are approximately defined by the rotor components (the hub and the blades). Wind turbines usually employ a pitch control system particularly for large machines, but the fixed-blade pitch and stall control are still used in some medium sized turbines. Most turbines today contain upwind rotors with three blades but some still contain downwind rotors with two blades. The blades on the majority of turbines are made from composites, primarily fiberglass or carbon fibre reinforced plastics, but occasionally wood/epoxy laminates are used.

1.1.3 Drive Train

The drive train is composed of a low-speed shaft (on the rotor side), a gearbox, a high-speed shaft (on the generator side) and other components such as support bearings, one or more couplings, a brake, etc. The gearbox will increase the rotational speed of the rotor from a low value (tens of rpm) to a rate suitable for driving a standard generator (hundreds or thousands of rpm). Parallel shaft and planetary are two types of gearboxes in the WECS. Planetary gearboxes are usually adapted for larger machines due to the weight and size advantages. Furthermore, fluctuating winds and the dynamics of large rotating rotors must be considered in the design of wind turbine drive train components.

1.1.4 Generator

In general, wind turbines are divided into variable-speed and constant-speed wind turbines. If they drive at a constant or limited speed and connect directly to the grid, they are known as constant-speed wind turbines. However, if they operate at variable speeds with power electronic components, they are known as variable-speed wind turbines. The grid connected wind turbines (constant-speed) usually make use of squirrel cage induction generators (SCIG). Thus, these type of generators operate within a narrow range of speeds, slightly higher than its synchronous speed. Rugged construction, low cost, and ease of connection to an electrical network are the main advantages of this type of machine.

Due to their ability to capture the maximum amount of power from the wind energy, the variable-speed wind turbines are popular for utility-scale electrical power generation. When used with suitable power electronic converters, either synchronous or induction generators of either type can run at variable speed. The doubly-fed induction generators (DFIGs) and the permanent magnet synchronous generators (PMSG) are popular for use in variable-speed generators. Table 1.1 indicates a comparison of the features of different types of wind turbines [3].

Table 1.1 A comparison of different types of wind turbines.

Type of generator	**SCIG**	**DFIG**	**PMSG**
Aerodynamically	Less efficient	Efficient	Efficient
Electrically	Efficient	Less efficient	Less efficient
Gearbox	Included	Included	None
Converter	None	Partial	Full
Electrical Noise	Noisy	Less Noisy	Less Noisy
Aerodynamic Noise	Noisy	Noisy	Noisy
Design	Simple	Convectional	Unconventional
Weight	Heavy	Heavy	Heavy
Cost	Normal	Less Expensive	Expensive
Speed	Constant Speed	Speed Range	Variable Speed

1.1.5 Nacelle and Yaw System

The drive train components are placed in the main frame and the contents are protected from the weather by the nacelle cover. The rotor shaft is aligned with the wind by the yaw orientation system. The main frame is always connected to the tower with a large bearing. An active yaw drive is always employed for upwind turbines and

sometimes is used with downwind turbines. It is composed of one or more yaw motors which drives a pinion gear against a bull gear attached to the yaw bearing. An automatic yaw control system with its wind sensor controls this mechanism. Yaw brakes are sometimes used with this type of design to hold the nacelle in position when not yawing.

1.1.6 Controls

A wind turbine control system includes sensors, controllers, power amplifiers, etc. Three properties are considered in the control system of the wind turbines: limiting the input torque by the gearbox, maximizing the fatigue life of the structural components of the wind turbine, and maximizing the power production.

1.2 Influence of Wind Power on the Power System

Voltage fluctuations, harmonics, reactive power, power peaks and in-rush current are specifically considered in the grid power quality while the wind power integrates into the power system. These issues can be caused by the wind turbine electrical components such as the generator, transformer, etc., but also by the aerodynamic and mechanical components such as the rotor and drive train. In this thesis, the wind generator's behaviour is investigated among WECS components, throughout.

1.3 Summary of Relevant Literature

1.3.1 Micro-Machines

Micro-machines were developed in the 1950s in order to generate empirical data [4]. They are designed by down-scaling large, utility-scale machinery. The prototyped micro-machines are used for training and teaching purposes, developing a control system, power system stability studies and the testing of theoretical assumptions and approximations used in various analytical calculations. Recently, investigation of the transient behaviours of power plant and power system have become the other additional applications of the micro-machines [5], [6].

Due to the micro-machine's capability to test under exact operating conditions, they are used to research steady-state and transient phenomena in electrical power systems even though the digital technology is advanced [7]–[12]. In fact, the time constant regulators (TCRs) have been created in order to increase the simulation accuracy run by the micro-machines under transient conditions [5], [13]. Simulated turbine generators [14], parameter identification for generators and validation of digital models of power system [15], [16] are also cited as applications of micro-machines.

1.3.2 Dimensional Techniques

Dimensional analysis is a critical technique in designing micro-machines. This technique considers a relationship between the machine's structures and its behaviour. Dimensional analysis usually assists the scaling process to create scaling factors in order to design a micro-machine. Scaling of a transformer is reported as first scaling by the elementary physical approach [14]. The electric machines' dynamic models are more complex than transformers due to their structures. Therefore, the result of geometrical scaling for electric machines is inaccurate. In [10], it is presented that physical similarities between the reference machine and micro-machine does not guarantee similarity in the machines' characteristics under the same conditions. In addition, it is presented that boundary and initial conditions also affect the size of the physical model in the scaling process. In [8], operating under low temperatures is recommended in order to reduce the complexity of the micro-machine by increasing the conductivity of the machine's conductors. The authors of this paper employed liquid nitrogen in order to achieve their objective. In [12], it is reported that reduction in the machine's size increases its losses and the micro-machine's characteristics are defined by its equivalent circuit parameters. Therefore, the dynamic responses of micro-machine and reference machine will be the same if the resistances and the reactances of both machines become equal in the per-unit system. Brechten and his colleagues recommend a novel approach to developing micro-machines by defining equations which describe relations between the micro-machines and the reference machine. These defined equations are constrained by geometrical infeasibility. A dynamic-response-control, known as Model Reference Following Controller (MRFC), is developed in [12]. MRFC adapts two pulse width modulators (PWMs) to feed the two rotor windings in order to control a micro-synchronous machine.

1.3.3 Investigation of Wind Power Behaviour by Micro-Machines

It is known that synchronous generators have the major share in the electricity generation within the power system. Their behaviours under various conditions have been investigated for decades [17], [18]. While the wind energy in the power system continually increases, the WECS usually uses variable speed generators with power electric convertors such as DFIGs and PMSGs. The behaviour of these types of generators require more research because they are new in the grid. Therefore, numerical modelling has been employed to simulate and investigate the WECS's behaviour under faulty conditions [19]–[21]. However, these simulations can be heavy and time consuming when they are based on the accurate model of the wind turbine. They can also lead to

lower accuracy of dynamic results when a simplified model of wind turbines is used. As noted, the micro-machines can assist in investigating this new phenomena behaviour in the grid. If the wind generators are scaled based on the relationship between the physical dimensions and the machine's behaviour under dynamic conditions, then the scaled-generator or the micro-machine will behave in a similar manner under the same conditions. In fact, the scaled-machine behaves the same as the reference machine under the transient condition and its behaviour towards the grid can be researched with acceptable accuracy and within reasonable time.

1.4 Aim and Objectives

Development of a scaled doubly-Fed induction generator for assessment of wind power integration issues is the aim of the research and the objectives are as follows:

- Develop a scaling methodology for a utility-scale DFIG.
- Develop a design methodology for the detailed design of the scaled DFIG.
- Analyse the design of the DFIGs with numerical techniques.
- Prototype, test and compare the scaled machine's performance to that of the utility-scale DFIG.
- Analyse specific grid integration issues with the laboratory-based system and compare with results from actual and power system simulations.

1.5 Research Questions

The research questions related to the thesis are as follows:

- How can a DFIG be down-scaled with inherent non-linear magnetic and electrical properties?
- How can a Micro-Machine be designed to have the same dynamic characteristics as a utility-scale DFIG?
- Which grid integration issues require more accurate models of DFIG systems than those available in order to perform meaningful analysis?
- Can a Micro-Machine be used to analyse specific grid integration issues with DFIGs more accurately?

1.6 Research Output and List of Publications

The research output and list of publications are as follow:

- Design, Prototype and Test a micro-DFIG.

- H. Dehnavifard, M. Khan, and P. Barendse, “Development of a 5kW Scaled Prototype of a 2.5 MW Doubly-Fed Induction Generator,” *IEEE Trans. Ind. Appl.*, 2016.
- H. Dehnavifard, A. C. Wozniak, M. A. Khan, and P. S. Barendse, “Determination of parameters of doubly-fed induction generators,” in *2016 XXII International Conference on Electrical Machines (ICEM)*, pp. 2769–2774, 2016.
- H. Dehnavifard, X. M. Hu, M. A. Khan, and P. S. Barendse, “Comparison between a 2.5 MW DFIG and CDFIG in wind energy conversion systems,” in *2016 XXII International Conference on Electrical Machines (ICEM)*, no. 3, pp. 238–244, 2016.
- H. Dehnavifard, M. A. Khan, and P. Barendse, “Development of a 5kW scaled prototype of a 2.5 MW Doubly-fed induction generator,” in 2015 IEEE Energy Conversion Congress and Exposition (ECCE), 2015, pp. 990–996.
- H. Dehnavifard, A. D. Lilla, M. A. Khan, and P. Barendse, “Design and optimization of DFIGs with alternate voltage and speed ratings for wind applications,” in 2014 International Conference on Electrical Machines (ICEM), 2014, pp. 2008–2013.
- A. D. Lilla, H. Dehnavifard, M. A. Khan, and P. Barendse, “Optimization of high voltage geared permanent-magnet synchronous generator systems,” in 2014 International Conference on Electrical Machines (ICEM), 2014, pp. 1356–1362.

1.7 Organisation and Scientific Contribution of the Thesis

In this project, it is assumed that DFIGs are employed in the WECS. Therefore, a micro-DFIG is developed to behave similarly to the utility-scale machine in order to investigate wind power issues. To design a micro-DFIG, the dimensional analysis technique is employed. This technique’s constraints are justified for DFIGs because of their specific design. For instance, DFIGs have 3-phase windings on their rotor, as opposed to synchronous machines. Finite Element methods (FEMs) are adapted to prove the similarity of both machines’ behaviours under transient conditions. Finally, the machine is prototyped and tested.

The thesis is completed as follows:

Chapter 1: Introduction

Chapter one defines the wind turbine and its components to present the effective elements on output dynamic behaviour. It gives a literature survey on the micro-machines and dimensional analysis. It also discusses micro-machine’s advantages in order to investigate the wind energy in the power system.

Chapter 2: Induction Machine Design Considerations

Chapter two covers a literature review on induction machine design trends and focuses on wound rotor induction machines. It includes market interest towards electrical machines and in particular, wind generators. Also, it sheds light on unknown aspects of machine design and is an effort to illustrate the important points regarding induction machines. To conclude, it presents the areas which require further investigation.

Chapter 3: Wound Rotor Induction Machine Design

Chapter three explains the machine's design theoretically with sizing equations and empirical data. It also presents a reference DFIG analytical design along with its 2D finite element analysis (FEA) simulation.

Chapter 4: Wind Energy Conversion System with DFIG

Chapter four describes a WECS component which includes DFIGs with different speeds and voltages. It presents the cost and efficiency of the WECS's components while the generator voltage and speed change within a limit. It investigates a better DFIG specification based on WECS's cost and efficiency.

Chapter 5: Wind Power Integration Issues

Chapter five investigates the wind power integration issues. It describes how the power system will react if there is a fault in wind power. It discusses the possibility of using the micro-machines to develop a better understanding of the wind energy integration issues.

Chapter 6: Dynamic Model of DFIG

Chapter six presents the common mathematical modelling of induction machines. It seeks to define the most important elements on transient behaviour of DFIGs by ignoring time as a variable. These elements are considered in the dimensional analysis in order to maintain the dynamic behaviour of the reference DFIG in the scaled-machine.

Chapter 7: Micro-Machines and Scaling

Chapter seven begins with a literature review about micro-machines and the scaling process. It presents a dimensional analysis which is adjusted for wound rotor induction machines. The micro-DFIG is presented in this chapter and ultimately, it is verified through FEA.

Chapter 8: Prototyping and Identification of micro-DFIG

The process of the manufacturing of the micro-DFIG is illustrated in chapter eight. The test rig is also discussed. At the end, the micro-DFIG is tested under blocked-rotor and no-load condition to identify its equivalent circuit.

Chapter 9: Transient Response of micro-DFIG

In chapter nine, FEA is used to simulate the DFIGs under transient conditions through various scenarios. The micro-machine is tested under similar conditions. The FEA and experimental results are satisfactory and meet the objectives.

Chapter 10: Conclusion and Recommendations

The conclusions based on the FEA results and the micro-DFIG's results at the transient-state are made in chapter 10.

2. Induction Machine Design Consideration

Induction machines (IMs) are the most popular electric machines in industry. These machines are rugged and do not require separate DC field power. They are very economical, reliable, and are available in a wide power range, from fractional horse power (FHP) to multi–megawatt capacity. Induction machine design, structural analysis, efficiency and the state-of-the-art features are discussed in this chapter. The objective is to review what has been accomplished in these years in terms of the design and manufacturing of induction machines.

2.1 Introduction

IMs were invented with a wound rotor in 1889 and later using a squirrel cage rotor. As with synchronous machines, induction machines have 3-phase windings on their stator. Their rotor slots can be filled with 3-phase windings or by solid bars. These types of electric machines are known to have robust construction, simple design and lower cost. IMs can be operated at variable speeds, which is in contrast with synchronous machines. Also, their connection process to the grid is relatively simple. They usually operate at a low lagging power factor and often require power factor correction capacitors to improve their operating power factor [22], [23].

Squirrel cage induction machines have their rotor slots filled by solid conductive bars. These machines are the most common type of induction machines due to the simplicity and robustness of their design and relatively low cost. This type is widely used in stand-alone wind power generation schemes.

Wound rotor induction machines have 3-phase windings on the rotor and are consequently more expensive and less robust than squirrel cage machines. Wound rotor machines are preferred due to their ability to produce a high starting torque. If wound rotor induction machines are fed through their rotor, they are called doubly-fed induction machines. These machines can deliver power to the grid through their stator and rotor [3], [24], [25]. In fact, this is an advantage of wound rotor that it has the ability to extract rotor power but comes at the added cost of power electronics in the rotor circuit [9], [22], [26]. An emerging application for doubly-fed induction generators (DFIGs) are in wind energy conversion systems (WECSs). This is mainly due to its simplicity and low cost in relation to competing wind generator technologies like the permanent

magnet synchronous generators (PMSGs) [1], [18], [27]. However, they require a gearbox for low speed operation, particularly in wind energy applications [3], [9].

2.2 Current Utilisation of Induction Machines

Electric motors are the main energy conversion devices used in the modern world. In developed countries, there are more than 3kW of installed electric motors per capita [28]. Figure 2.1 shows the estimated share of global electricity demand by end-use applications [29]. The figure shows that electric motors consume approximately 46% of generated electricity in 2015. This means that if the efficiency of electric motors increases by a small percentage on average, it will ultimately lead to significant energy savings. The estimated number of electric motors installed in 2012 was 48.1 million units and this estimate is expected to grow to approximately 60.8 million units by 2017 [30]. The ratings of IMs vary from tens of watts to 400MW [3], [31]–[34].

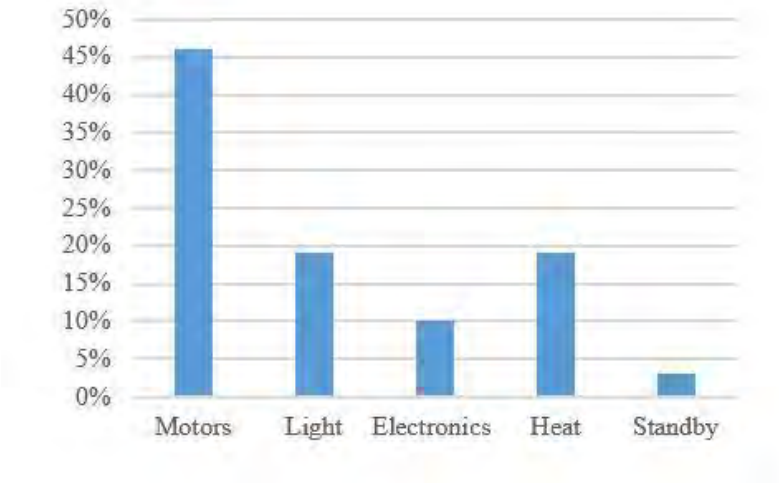

Fig. 2.1 Estimated share of global electricity demand by end-use application in 2015.

As mentioned previously, induction motors are popular due to their rugged design and moderate cost. Furthermore, they are typically connected directly to the grid through protective devices such as relays and circuit breakers. In domestic applications, low power induction motors are typically fed from a single-phase main supply. Home appliances, account for approximately 79% of the residential energy consumption globally, as shown in figure 2.2 [34]–[37].

Global revenue from the manufacturing of IMs was 250 million dollars in 2014 and it is forecasted to be between 300 and 350 million dollars in 2017 [28]. In fact, the electric motors market will grow by 40% by 2017. Moreover, IMs can be supplied through converters to provide variable speed operation of motorised systems. In fact, more than 30% of the installed induction motors globally are powered through variable speed drives

[3]. The demand for variable speed drives has increased by 10% annually since 2010, while the average annual growth in the electrical machines market was at a rate of 5% over the same period [28]. It is predicted that more than half of the electric machines will be controlled by a variable speed drive in the next decade, whilst IMs would dominate up to 60% of the new market.

An emerging market for induction machines is in the wind energy sector, which has been growing gradually since 1997. By the end of 2014, 423GW of electricity generated was by wind farms in 80 countries, which primarily used induction generators. These machines compete with permanent magnet generators in the market. There are, however, no accurate market share details for different systems (DFIG and PMSG) due to a lack of manufacturer information. Table 2.1 illustrates the wind generator suppliers by their share market percentage for 2014.

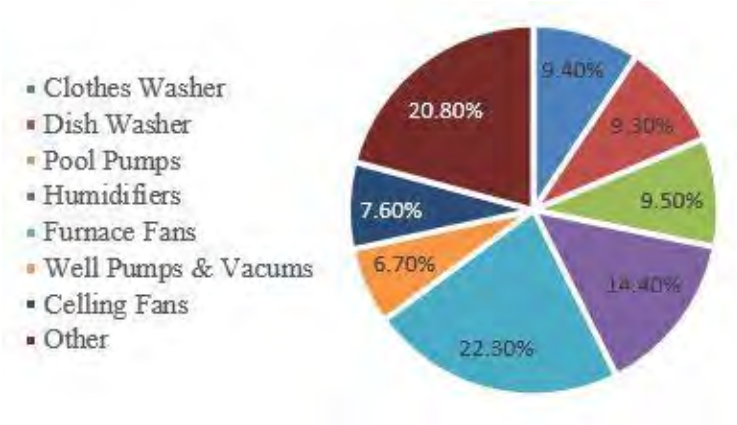

Fig. 2.2 Household motor energy consumption in terawatt-hours.

Table 2.1 Wind turbines' suppliers of 70 percent of the market share.

Manufacturer	**Generator types and drive train**		**Market share (≅70%)**
GE (US)	IG[1], DFIG[2]	PMSG[3]	11.8%
Vestas (Denmark)	IG, DFIG	PMSG	11.8%
Siemens (Germany)	IG, DFIG	PMSG	11%
Enercon (Germany)	--	PMSG EESG[4]	7.2%
Suzlon Group (India)	IG, DFIG, SCIG[5]	--	6.6%
Gamesa (Spain)	IG, DFIG	PMSG	6.4%
Goldwind (China)	--	PMSG	6.0%
GuoDian United (China)	IG, DFIG	--	3.5%
Sinovel (China)	IG, DFIG	--	2.7%
Sewind (China)	IG, DFIG	PMSG	2.3%

[1] Induction Generator
[2] Doubly Fed Induction Generator
[3] Permanent magnet synchronous Generator
[4] Electrical excited synchronous generator
[5] Squirrel Cage Induction Generator

2.3 Essential Knowledge for Design of an Electrical Machine

The design of an electrical machine involves the selection of electrical, magnetic and insulation materials, and the detailed dimensioning of the magnetic circuit and electrical circuits. This is carried out through detailed consideration of the design equations for the specific machine under investigation. In general, there are a number of possible design solutions that will meet the user specifications for the design, but it is the designer's task to find the optimum solution, which will be based on necessary trade-offs encountered throughout the design process. The desired solution must have important features such as high efficiency at rated speed, high power and torque density, tolerable temperature rise, and ultimately low cost. Finally, the durability and reliability of the machine must be considered in the design process. The manufacturing conditions form part of the design challenges [3], [38], [39]. The design process also requires knowledge of the following areas related to the machine type [40]:

- National and international standards
- Specifications (that deals with machine ratings, performance requirements etc., of the consumer)
- Cost of materials and labour
- Manufacturing constraints

The desired design values will be achieved by iterative methods in order to overcome the design complexities. Therefore, computers play an important role to evaluate aspects of the design with sufficient accuracy throughout the design process. Moreover, laboratory testing of a prototype can be used to validate the numerical results and assess if the design specifications were achieved [41], [42].

2.4 Selection of Materials

Induction machines have magnetic circuits which permeate the revolving magnetic fields, and also electric circuits which have alternating currents. The electric circuits have a different purpose from the magnetic circuits, and are insulated from each other. The magnetic, electric, and insulation materials are defined by their characteristics and their losses [39], [43].

2.4.1 Insulation

Insulation materials are used to prevent short circuits between conductors, and between conductors and the laminated cores in electrical machines. The insulation material is selected based on the electrical circuit of the machine, but is required to be

compatible with the cooling system and the magnetic circuits of the machine. In fact, the insulation helps to withstand inter-turn, phase-to-phase and phase-to-ground faults. In the stator and rotor, the laminations are insulated from one-another by a special coating which minimizes eddy current losses in the core. It is cited that bearing and shaft voltages and currents are reduced by insulating the bearing housing. This helps to prevent premature bearing damage. This is especially prevalent in PWM converter fed IMs, where there are additional common mode high frequency capacitor currents [44]. In addition, PWMs causes the applied current and voltage to become non-sinusoidal. This means the current peaks result into raising the insulations' temperature. The voltage peaks and the voltage transient also causes the insulation stress. These effects will accelerate insulation ageing [45]. Moreover, the insulation has to withstand the expected operating temperature. There is a slow deterioration of insulation by internal chemical reactions and contamination which causes cracks in the enamel, varnish or resin and thus reduces the dielectric strength of the insulation [26], [46]. Flexible sheet materials such as cellulose and polyester film proposed in [39], [47] are used to provide a slot to phase insulation for class "A" temperatures. In high-temperature IMs (class "F", "H"), glass cloth paper treated with special varnish is used for a slot to phase insulation [32], [34], [39].

2.4.2 Laminations and Magnetic Material

The permanent magnet dipoles inside the material define the magnetic properties of the material. As known, hysteresis is a property of magnetic materials which may cause energy loss in electric machines. The alloys of iron, nickel, cobalt plus silicon-steels are known as soft magnetic materials due to having low hysteresis. These materials include micro-domains whose sizes are between 10^{-4} and 10^{-7}m. When completely demagnetized, these domains have random orientations and therefore the material has zero remanence in all finite samples. The result of dipoles varies within the magnetic material and creates B-H curves for each material [48]–[50]. Magnetic materials can be categorised by their B-H curves.

Annealed iron (soft) is desirable to make a core for rotating machinery due to its high level of a magnetic field tolerance (until 2.6 Tesla) without saturating. Soft iron can boost the magnetic field concentration up to 50000 times more than air core. This material has a high conductivity which causes high eddy current loss and undesirable heating. Two methods are usually employed to decrease the conductivity of the iron: alloying with silicon; and lamination [51].

Silicon-steel is an iron with up to 6.5% silicon and it is usually manufactured in a cold-rolled with less than 2mm thickness [52]. The maximum thickness of lamination in the

electrical machines' cores is 1mm [3]. The silicon-steel's mechanical property depends on its silicon concertation. Silicon ultimately reduces core losses by decreasing iron conductivity. Basically, it decreases the induced eddy currents and narrows the hysteresis loop. Then, the machine's core will be laminated by the plates made of silicon-steel. These laminations are coated to decrease conductivity between plates. The coating protects the laminations from oxidation and acts as a lubricant while die cutting [34]. It is reported for IMs of fundamental frequency up to 300Hz, that 0.5mm thick silicon steel laminations lead to reasonable core losses of approximately 2 to 4W/kg at 1T and 50Hz. For higher fundamental frequency, thinner laminations are required [52]–[54].

2.4.3 Electrical Conductors

In general, copper conductors are used for electrical machine windings. The type of conductor, either circular or rectangular depends on the machine's rating. Wound rotor induction machines (WRIMs) have three phase windings on both their stator and rotor. The size of the conductors in three phase windings depends on the current density. Also, it is reported that current density affects the cooling system, service duty cycle, and the targeted efficiency. The current density lies between 3.5 to 6A/mm^2 for high efficiency WRIMs. It is possible to twist several elementary conductors (6 to 8) in parallel to reduce the skin effect to acceptable levels [23], [38], [55].

2.5 The Induction Machine Design Process

Several design approaches are available in literature, but majority start the process with design specifications and pre-assigned values of flux densities and current densities. Then, the stator bore diameter (D_{is}), stack length (L_i), number of stator and rotor slots, stator outer diameter (D_{out}), stator and rotor slots' dimensions are determined by means of various approaches. Typically, the design algorithms iterate until an acceptable efficiency and power factor have been achieved. If the results of the design process are unsatisfactory, the whole process will be restarted from the initial state [3], [27], [31], [39], [56], [57]. Due to the ability to simulate the geometric variations and irregularities, saturations and eddy current effects with a high degree of accuracy, using finite element method (FEM) to design electrical machines is popular. Radial flux machines are usually simulated in 2D while axial flux machines require simulating in 3D to trace the flux lines as well as the flux densities axially [19], [58]–[61]. In [21], the authors developed a finite element (FE) based analysis by employing reduced models for both stator and rotor. This model is fast and accurate enough that can be used for designing a large induction motor. The optimization of the machine design is a multivariable and multimodal optimization

problem. Traditionally, a combination of analytical and empirical methods are used for convectional design optimization. However, the emerging trend of design optimization is based on FEM analysis combined in the optimisation loop. The evaluation of alternate designs becomes simple and accurate by using FEM models. However, the simulation time becomes lengthy when attempting to increase the accuracy of FEM calculations [62], [63].

Madescu and Boldea present a practical nonlinear model which can be attached to the industrial design tools for induction motors. Their main aim was to develop a two-dimensional model which divides the machine into five circular cross-sectional domains [57]. A canonical particle swarm optimization (PSO) technique is employed to develop a fast and efficient multi-objective optimization design method for induction machines [64]. Less design iterations are required in this method than traditional design methods. Computer aided design (CAD) approach is presented for the design of an efficient and compact DFIG. The designed DFIG is validated by means of finite element (FE) analysis. The designed DFIG developed by the CAD program is then compared with a conventionally designed DFIG of the same rating. The comparison involved the active volume of the machine, airgap harmonics and efficiency at variable speeds [65], [66]. There appears to be a need for the development of better approaches for the design of wound rotor induction machines, as most of the literature and commercial machine design software focuses on squirrel cage IMs due to the interest of manufacturers.

2.5.1 Main Induction Machine's Dimensions

Sizing equations for an electrical machine are presented in [22], [23], [26], [40]. The authors describe various techniques to calculate the stator inner and outer diameters, core length, equivalent slot dimensions, flux density as well as the number of poles. The stator diameter and core length are the main dimensions of electric machines. There are two different methods to calculate the length and diameter for IMs: 1- based on output coefficient design concept (C_0) and 2- based on the rotor shear stress. The following equation can be used to calculate the stator inner diameter (D_{is}) for the machine [39], [56]:

$$D_{is} = \sqrt{\frac{Q}{L_i n_s C_0}} \qquad 2.1$$

where p_1 is the number of pole pairs, Q is the input power, L_i stator length, n_s is the synchronous speed, and C_0 is the output constant. Boldea and Lipo recommended the rotor shear stress to calculate the inner stator diameter (D_{is}) [25], [31]. Therefore,

$$D_{is} = \sqrt[3]{\frac{2 \times T_e}{\pi \times \lambda \times f_{xt}}} \qquad 2.2$$

where T_e is electromagnetic torque,λ the aspect ratio and f_{xt} is the rotor shear stress for induction generators. The aspect ratio is defined as the ratio of the stator length (L_i) to diameter (D_{is}):

$$\lambda = \frac{L_i}{D_{is}} \qquad 2.3$$

The ratio between the length and diameter of the machine will determine the power factor and the cost of materials of IMs. In several references, methods are proposed to ensure that the target operating characteristics are achieved [3], [9], [26], [39], [40], [67]. The authors propose that the ratio of stack length to pole pitch ($\frac{L}{\lambda}$) may reduce costs if ($1.5 < \frac{L}{\lambda} < 2$), improve power factor if ($1.0 < \frac{L}{\lambda} < 1.25$), improve efficiency if ($\frac{L}{\lambda} = 1.5$), and it is better to use ($\frac{L}{\lambda} = 1$) in order to design DFIGs. The value of the ratio ($\frac{L}{\lambda}$) was suggested to be between 0.6 and 2, depending on the size of the machine and the characteristics desired. Figure 2.3 indicates the acceptable range for the stack aspect ratio for the number of pole pairs [27]. It is reported that an increased stack length leads to additional winding losses of up to 10 percent [24], [68], [69].

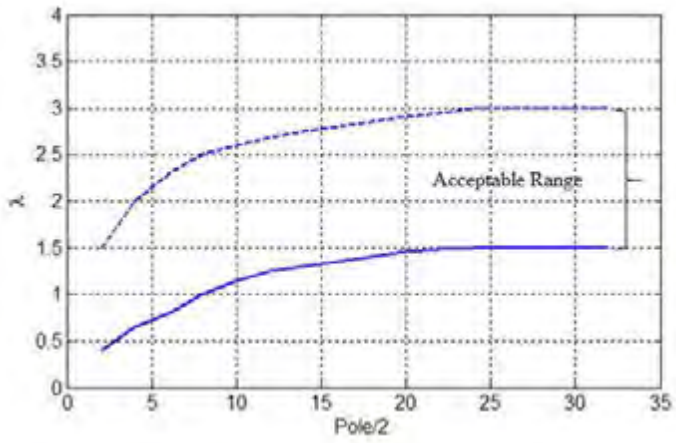

Fig. 2.3 IMs empirical stack aspect ratio versus number of pole pairs.

When choosing the diameter of the IM's stator, the peripheral speed is considered. It is suggested that the peripheral speed should not exceed about 30m/s [37], [70].

2.5.2 Standard Frames

Standard induction motor frames determine the overall mechanical structure of the machine. The frame includes: the stator, bearings, end cover, and terminal box. It provides safety, the ability to withstand twisting forces and shock when transmitting the torque, as well as ventilation. Apart from a few special machines, the manufacturers of

all modern machines for industrial applications provide a series of standard frames which cover a wide range of power ratings [71], [72]. As the airgap of an induction machines is relatively small, the frame structure must be rigid in order to keep the stator and the rotor concentric, otherwise, it can cause unbalanced magnetic pull [67], [72]. The frame may be die-cast or fabricated. Machines with rating of approximately 50kW usually have their frames die-cast in a strong silicon aluminium alloy and in some cases with the stator core cast in. The process of die-casting has an advantage in that it facilitates the use of a thicker cross-section frame in places where greater mechanical strength is required. The die-cast frames do not require machining [34], [73]. The casing of small machines is usually a single unit and comes on a base plate. The large-sized machines' frames are made up of a few steel plates. Depending on the design, the frame can be adapted and modified. In machines with radial ventilating ducts, the stator core is placed inside the frame on axial ribs, thereby providing an annular space for air between the core and the frame [39], [43], [53].

2.5.3 Stator Structure of Induction Machines

The stator consists of a cylinder made of laminations. The stator laminations are packed and placed into a frame. The stator core is laminated in segments for large machines in order to avoid wasting steel. Depending on type of silicon-steel the outer arch length of each segment can be between 0.3 and 0.8 m [74]. This will give an economical balance between the cost of dies, the cost of assembly and the amount of left-over scrap material after cutting the laminations from steel strips. Long cores are divided into a number of stacks. Radial ventilating ducts are sandwiched between them for efficient cooling. The width of a single stack of core should not exceed 0.5 to 0.6 m [39], [73], [75]. The slot geometry is designed according to the IM's power ratings. The slot geometry has an important effect on the operating performance of IMs. The slots can be open or semi-enclosed depending on the type of conductors (round or rectangular) (figure 2.4).

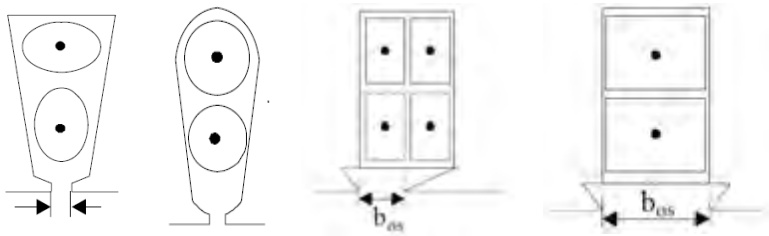

a b c

Fig. 2.4 Slot geometrics to locate coil windings: a) semi-closed, b) semi-open, c) open [3].

Due to decreasing flux pulsation in the rotor tooth which increases core losses, only one side (stator or rotor) is an open slot [76], [77]. The winding coils can be formed before they are inserted into open-slots. The windings are more accessible when a need arises for removing individual coils. In addition, decreasing the leakage reactance is one of the merits of open slots. The coils must be formed after they are inserted in the semi-enclosed slots. The semi-enclosed slots are used for the induction motor because they result in smaller values of magnetizing current. As mentioned, the semi-enclosed slots will have a lower tooth pulsation loss and a much quieter operation as compared to open slots [78], [79]. Also, wedges are inserted at the openings of open-slots or semi-open-slots to protect the windings from centrifugal forces and they are usually made up of wood or Bakelite. It is recommended that a large number of narrow slots can minimize tooth pulsation losses and noise in small IMs with open type slots [33]. It is reported in various sources that in small IMs where round conductors are used, the tapered slot with parallel sided tooth arrangement is useful, as it gives the maximum slot area for a particular tooth flux density. In large and medium sized IMs, where strip conductors are preferred, parallel sided slots with trapped teeth are used [3], [26], [79]. The large number of stator slots will result in a small width of stator teeth, which may lead to the teeth becoming mechanically weak. Moreover, the thin stator and rotor teeth may result in excessive flux density levels in the teeth and higher iron losses. The narrow teeth would be better to support at the radial ventilating ducts by welding the laminations [40], [70], [80]. It is reported that having approximately equal tooth width and slot width would help to have uniform flux density in the tooth. Also, the deep slots result in a large value of leakage reactance [3], [25]. Moreover, the leakage reactance also increases if the number of slots per pole per phase decreases, which in turn reduces the cost of the winding due to the lower number of coils. On the other hand, the large number of slots causes leakage flux and hence the leakage reactance decreases, which results in a higher overload capacity. The cost also increases with a larger number of slots due to increasing number of coils. Therefore, it is good practice to use as many slots as economically possible [18], [27], [39]. Usually, the slot space factors in IMs lie between 0.25 and 0.4mm. High voltage machines have lower space factors due to the large thicknesses of insulation [74], [78].

2.5.4 Rotor Structure of Induction Machines

The rotor core is laminated as a single plate in small machines and a segmental plate in large machines. The rotor core pack is keyed to the shaft by a ring. The ring keeps the plates together and the key transfers torque to the shaft and it usually makes the rotor

core skewed. The simplest way to reduce the harmonics is by skewing, which however lowers the power factor and overload capacity of the machine. Therefore, it is better to mention here that a large airgap length can decrease the harmonic torques, but it also reduces the power factor and overload capacity on the IM [25], [40].

Depending on the size of the machine, radial and axial ventilating ducts are inserted in the rotor to provide adequate air circulation. The number of radial ventilating ducts in the rotor is usually equal to that of the stator [3], [18], [26], [39]. There are reports on the relationship between rotor eccentricity and shaft arms and stiffeners. It has been cited that if the rotor has not been placed on the shaft carefully or the shaft has not been installed centrally (inside the stator), it will create a parasitic harmonic, vibration and noise [3], [9], [22].

Generally, windings with an integer number of slots per pole per phase are used for the rotor and cannot be equal to the number of slots per pole per phase in the stator. Different policies are available in literature to select the number of slot per pole per phase for each squirrel cage and wound rotor induction machines [18], [23], [81]. For instance, it is recommended that the number of slots per pole per phase (q) must be an integer in order to produce completely symmetrical windings in WRIMs. However, it is recommended that fractional slot windings be used on the rotor for small WRIMs in order to reduce the harmonic content of the airgap flux density [31], [39].

In order to achieve a small airgap in IMs, the shaft should be short and stiff. In fact, even a small deflection would create noticeable irregularities in the airgap which would lead to the production of an imbalanced magnetic pull. In the case of short shafts, the diameter of bearings should be about two-thirds of the shaft maximum diameter [38], [39]. Roller bearings are used for horizontal shaft machines and thrust bearings are used for vertical shaft machines. The forces act radially in horizontal shaft machines while the axial load acts downwards in vertical shaft machines. Radial loads in this case can be caused either by the dynamic unbalance of the rotor or by the unbalanced magnetic pull of the rotor towards the stator [3], [34], [43].

The slip rings are made up of either brass or phosphor bronze. They are pressed together on the body of reinforced thermo-setting resin carried on a mild steel hub. The slip rings are located either between the core and bearing or on the shaft extension. When the slip rings are on the shaft extension, the shaft is made hollow to allow the three connections from the rotor to the slip ring to pass through the bearings. The brushless induction machine is designed to reduce the ohmic losses. Brushes are, however, still used in modern machines [24], [39], [82]. Runcos and Mauricio investigated a 350kW brushless doubly-fed 3-phase induction machine with its wound rotor circuit

connected to flat-plane rotary transformers. They reported the merits of eliminating brushes and slip rings by means of rotary transformers. In addition, they presented a rotary transformer design and demonstrated the operation of a 90-kW brushless doubly-fed three phase IM [83]. The design and performance analysis of a medium-speed brushless doubly-fed induction generation for a wind turbine drivetrain was investigated by Abdi. It was shown that the medium speed brushless DFIG in combination with a two stage gearbox, offers a low-cost, low-maintenance and more reliable drivetrain for wind turbine applications [84].

2.5.5 Airgap

The length of the airgap in an induction machine should be mechanically as small as possible in order to minimise the magnetizing current and improve the operating power factor. A large airgap can reduce the flux pulsation loss, however, it creates a small eccentricity and an unbalanced magnetic pull [24], [25], [48]. Several empirical equations are presented to calculate the airgap length [25], [56]. Say suggested equation 2.4:

$$g = 0.2 + 2\sqrt{D_{is}.l_i} \tag{2.4}$$

where g is the airgap. Lipo presented a few methods and he ultimately derived equation 2.5:

$$g = 3 \times 10^{-3}\tau\,(2p_1)^{\frac{1}{2}} \tag{2.5}$$

It is reported that a large airgap length would be better to facilitate cooling in induction machines. The variation of reluctance in the path of the zig-zag leakage flux is the reason for the noise in IMs. A large airgap length reduces the zig-zag leakage flux, which reduces value of the leakage reactance as well as the noise level of the machine [22], [71], [75], [85]. The flux density in the airgap should be moderate in order to limit the magnetizing current, which will result in a poor power factor. However, in induction motors the flux density in the airgap should be such that there is no saturation in any part of the magnetic circuit. Moreover, a large flux density in the airgap causes high iron loss, thus reducing the efficiency of the machine [48], [86].

2.5.6 Winding Structure

In general, the winding system is designed by assigning coils to the slots for different phases, establishing the direction of currents in the coil sides, calculating the number of turns for various coils, and finally sizing conductors for the slots. The number of coils is determined by the number pole pairs and the number of phases. Moreover, a large number of poles result in a poor power factor and also regulating the number of poles

can affect the magnetization current and the flux densities. Also, the number of turn per coil is assigned based on the flux density in the airgap and the conductor size depends on the operating current density. The large number of turns per coils produces a large winding mmf, which decreases the overload capacity of IMs.

The number of turns per coil is calculated as follows:

$$W_1 = \frac{K_E \frac{V_{SN}}{\sqrt{3}}}{2\sqrt{2} f k_f K_{W1} B_g \tau l_i} \qquad 2.6$$

where K_E is the back emf factor ($0.97 < K_E < 0.98$), V_{SN} is the stator phase voltage, f is the frequency, K_{W1} is the winding factor and B_g is the assumed airgap flux density, and k_f is filling factor. An important consideration in a three phase winding is to produce equal resistance and leakage inductance per phase, in order to ensure a balanced winding. The windings of electrical machines are restricted from movement in the radial direction. The wire bands of rotors and solid bands (retaining rings) are methods that are used for the carrying of rotor windings [87], [88].

Figure 2.5 illustrates lap and wave windings which are used for induction machines [3], [25], [38], [74]. Single-layer windings employ full pitch coils (y = τ) to produce a fundamental mmf with pole pitch "τ" and it would be practical to use an integer number of slots per pole per phase. "y" is the number of slots which are covered. A single-layer winding is appropriate for lower power IMs. Double-layer windings are shown in figure 2.6, which allow chorded (or fractional pitch) coils (y < τ) such that the end connections of coils are shortened and thus copper loss is reduced.

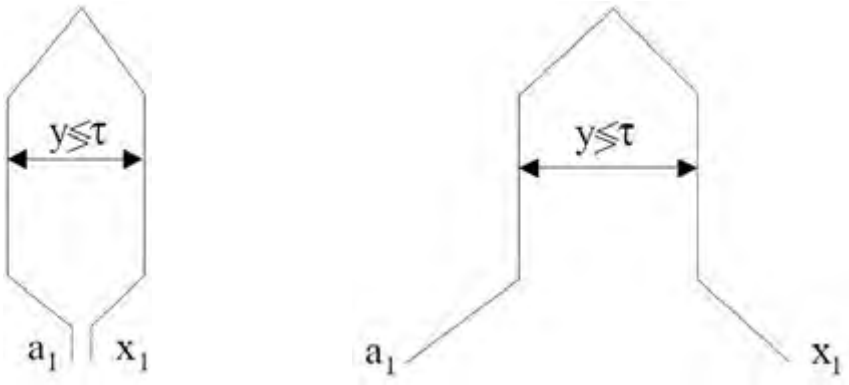

a b

Fig. 2.5 Lap a) and wave b) single turn coils [3].

It is recommended that the double layer lap type winding with diamond-shaped coils is generally used for stators and the use of single-layer mesh windings is suggested for small machines with a small number of slots and having a large number of turns per phase. The

three phases of the winding can be connected in either star or delta, depending on the starting methods to be employed [18], [25], [56], [74], [79].

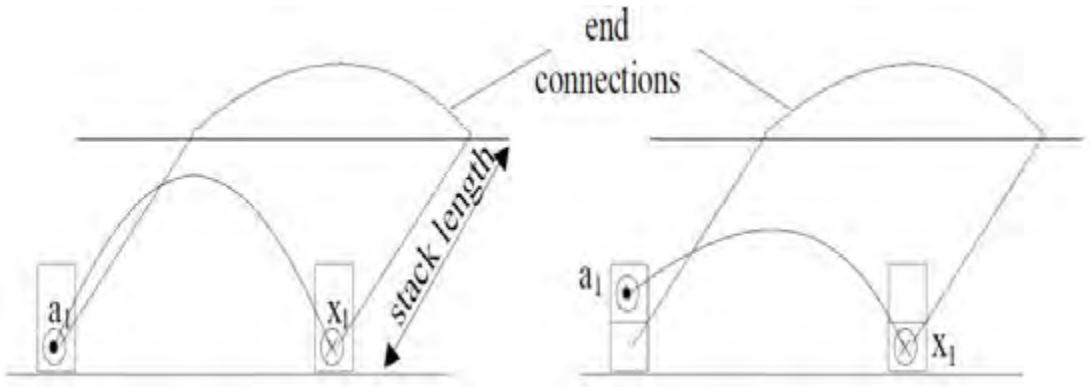

a b

Fig. 2.6 Single-layer a) and double-layer b) coils (windings) [31].

Fractional slot windings with two pole symmetry ($q = \frac{2n+1}{2}$) are investigated thoroughly in [87]–[89], where the authors suggest that $q = \frac{3}{2}$ for low power IMs. In general, fractional slot windings reduces copper weight and space harmonic content in IMs.

Pole-changing windings have been considered since the sixties. A method known as "the 3 equation principle" is presented in [90] for various pole count combinations. This is also a kind of symmetric method with a well-defined methodology. Alternating the number of poles in IMs is presented in [91]–[93] by changing the direction of the current in the windings.

When sinusoidal three-phase currents are supplied to the stator windings of an ideal machine, a sinusoidally distributed revolving mmf waveform is produced in the airgap of the machine. If the coils of a winding were to be placed in the airgap (in a slot-less machine) and distributed sinusoidally, then perfect sinusoidal distribution of mmfs would be possible. However, the airgap in this scenario would be large and this leads to the low power factor and efficiency [27], [39], [79], [94].

As known, the value of mmf depends on the size of the machine, the voltage of the stator winding, the type of ventilation and the overload capacity desired. A medium voltage high power machine is designed with a small value of Ampere-Turns [40], [79], [87]. The voltage induced in the rotor is at its maximum when the rotor of the machine is at rest. Therefore, to keep the rotor voltage at an acceptable level, the ratio of effective stator to rotor turns must be properly selected [18], [25], [26]. For a wound rotor IM, the rotor voltage on open circuit between the slip rings should not exceed 500 volts for small machines. The voltage is limited to a low value to protect the operator from the machine

if the brush gear is not perfectly protected. Moreover, it is easier to insulate the rotor windings with a low rotor voltage. The voltage in medium and large size machines can go up to 4kV [39], [95].

2.6 Cooling System and Thermal Modelling

The cooling system is designed for the efficient transfer of heat from the electrical machine's housing to the surroundings of the machine. Thermal models are considered when designing a cooling system. The thermal model of induction machines depends on the level and location of the losses, machine geometry and the method of cooling. Several thermal models have been recommended for IMs with regards to heat removal methods, temperature distribution and insulation tolerance [3], [25], [39], [40], [56]. Some thermal considerations will be discussed in this section.

2.6.1 Cooling System

The cooling system of an IM can be either natural or forced, depending on the rating of the IM. A natural air cooling system transfers the heat to the ambient air through a fan. A forced cooling system is designed to transfer the heat to a secondary heat exchange medium. In general, an air cooling system is preferred for electrical machines due to its simplicity [39], [96], [97]. Ventilators ducts are radial channels that are located at the regular interval along the axial length of the machine. Figure 2.7 shows the radial and axial ventilating channels. Radial and radial-axial cooling ducts are usually recommended for medium and large machines [24], [27], [98].

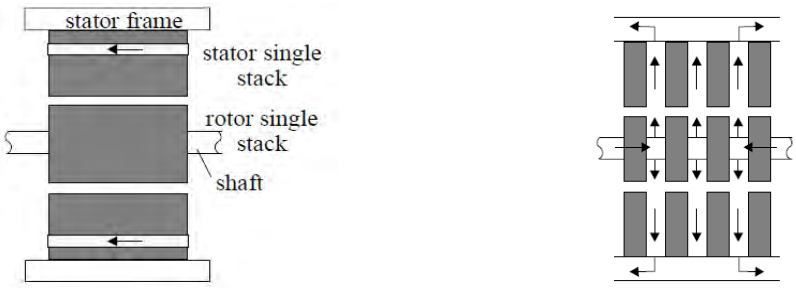

Fig. 2.7 a) single stack magnetic core IMs with axial ventilations b) multiple stack magnetic core IMs with axial and radial ventilations [3].

It is reported in the literature that large machines can have a smaller rotor diameter as well as better efficiency if they make use of an axial cooling system because their winding resistances will be lower. This allows larger machines the ability to handle larger power losses, without exceeding the thermal rating of the active materials used in the machine.

2.6.2 Thermal Modelling

Thermal circuit models and distributed models are described in [99], [100]. The conduction method of heat transfer essentially implies that thermal energy flows from a heat source to a heat sink. Generally, the heat source and the heat sink in IMs are windings and the ambient air, respectively. In IMs, the thermal energy flow is defined from the windings in the slots, through the conductor insulation and slot liner insulation, to the laminated core teeth. Convection heat transfer takes place between the surface of a solid body and a fluid. Convection depends on the velocity of the fluid, fluid properties, the solid body geometry and orientation. IMs are designed with a frame which has fins to allow heat transfer by convection. The insulated laminations reduces the transfer of heat along the axial direction, which therefore enhances heat conduction, convection, and radiation in a radial direction [3], [43], [98]. The conductor's insulation is designed for specific maximum temperatures. It is reported that the manufacturers test IM by keeping it at locked rotor conditions in order to determine the max temperature rise [43], [87]. A realistic thermal equivalent circuit for IMs at steady state and transient conditions is proposed in figure 2.8.

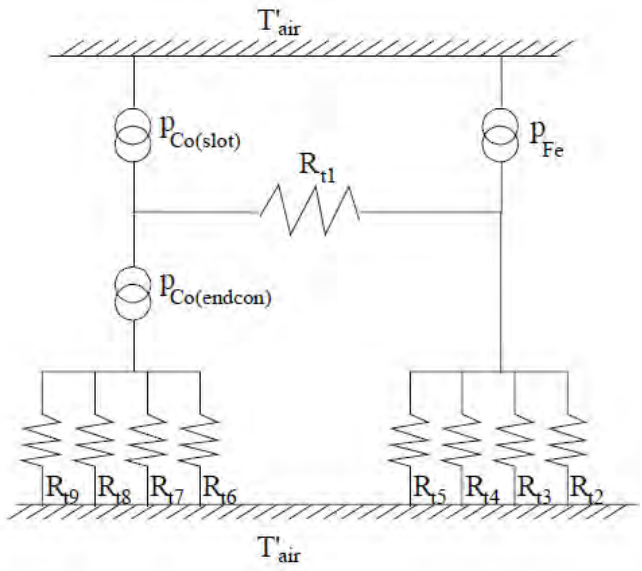

Fig. 2.8 Thermal equivalent circuit for stator or rotor windings [101].

The authors investigated a thermal equivalent circuit with finite element analysis software. The issue of heat flow in 2-dimensional coordinates is solved by using a finite element formulation with arc-shaped elements in the r-θ plane of a cylindrical co-ordinate system [102]. In 1995, Bellenda proposed a lumped parameters dynamic model for the analysis of the thermal behaviour of the induction machine, based on the machine's geometrical dimensions. He presented an approach to estimate the thermal behaviour of induction machines designed for the propulsion system of Electric Vehicles

[101]. Bolietti presented a simplified thermal model for a wound rotor induction motor in [103]. The lumped parameters and the analytical equations were used to compute the thermal model of a 3 kW motor. The model estimates the temperature with a tolerance of less than 7 percent.

The design of smaller induction motors with higher efficiency is the main concern of manufacturers. It is important to note that the temperature rise of an induction motor increases when their size decreases. This issue requires more attention in design and manufacturing of the machine. Therefore, the thermal sensitivity analysis of Total Enclosed Fan Cooled (TEFC) induction machines is presented in [104]. The thermal parameters of classical IMs were modified for TEFC IMs and their influences on the machine's temperature rise was shown.

2.7 Losses and Efficiency

In IMs, the conventional losses include the load dependent losses (stator copper losses , rotor copper losses and stray losses) and the load independent losses (the core losses, the friction and windage losses) [105]. Stator copper loss is the dominant loss in induction motors due to the finite stator winding resistance of the machine for a given current. The optimal design of the slot fill is a large slot (wide and deep) in the stator core that can assist in reducing copper losses by using thicker conductors and easy ventilation. However, this reduces the volume of the stator magnetic material, causing it to saturate and increase the core loss, thus a good compromise should be reached [3], [27], [34], [40], [71]. Copper losses in the rotor cause heating in the rotor conductive bars or windings. These losses can be reduced by using large rotor bars or conductors for the winding, which have lower resistance [25], [39], [98]. Also, thinner insulation can be used when the cross-sectional area of the conductor increases and the voltage is the same. Here, the material cost and slot space must be considered.

Zheng found the rewinding process as an opportunity to increase the efficiency of wind generators. He suggested a surrogate model to optimize a DFIG based on wind farm specific information and the DFIG's previous performance. Therefore, the windings will be optimized to match maximum efficiency [106]. Core losses are as a result of hysteresis and eddy currents in the magnetic structure of the IM. These losses are in both the stator and the rotor. Using modern steels which typically have high permeability and also low loss per kg will reduce these losses [107]. Thin laminations which are well insulated from each other reduce the eddy current path associated with the pulsating magnetic field in an IM and thus reduce the eddy current losses [3], [25], [38], [108]. Augusto presented detailed mathematical models of hysteresis [109], which was based on models presented

by Mayergoys in [110]. Yanase proposed a simple method for predicting the magnetic losses of electrical steel sheets in [111]. Pillay developed a model based on the three-term loss separation formula to predict lamination losses in induction motors. This model estimates the core losses by employing the flux density waveforms in different sections of a machine from FEM. The model results are verified by measured data from an 11kW induction machine [112]. The losses under an arbitrary induction waveform with or without minor loops can be estimated by this method under sinusoidal excitation. A new mathematical model of core losses in ferromagnetic steel, based on a minimal amount of experimental data, is described in [113]. This new model has a hysteresis loss coefficient that varies with frequency, eddy current coefficient and excess losses that are a function of induction. The new model is validated successfully on a large number of different samples of non-grain oriented fully and semi-processed steel alloys. Roy illustrates a modelling technique to estimate the core losses for wound rotor induction machine based on Mircea's method [114]. It was shown that 10 to 20% of the total losses are incurred in the magnetic materials of induction machines. The drag losses associated with the rotor and fan, and the mechanical friction due to the motor bearing together cause friction and windage loss. These losses are minimized by the good structural design of the rotor and fan, such as proper bearing selection with appropriate lubrication. Proper bearing alignment during assembly also helps to reduce these losses. If the bearing are not well positioned, there may be increased losses and premature bearing failure [105], [115].

Stray load losses are additional losses which are slightly more difficult to quantify and model. The stray load loss causes an increase in temperature and consequently decreases the torque of the machine. Some approximate equations for IMs have been presented in the references to predict stray losses [108], [116]–[118]. The process of repair and rewinding of electric machines affects the efficiency and particularly stray load loss. Cao analysed this effect in [119], [120]. Sana presented analytical methods to calculate the winding and the slotting effect on losses in a three phase induction machine in [121], [122]. These methods allow for the distinction between contributions from the stator and the rotor slot openings to the dynamic losses and, consequently, to the total iron losses.

2.8 Conclusion

As mentioned, IMs are the most popular among electric motors used in industry today. Moreover, a strong emerging application for IMs is in the wind energy sector. This chapter outlined the important considerations associated with the design of induction

machines. In particular, the active materials and insulation properties were discussed. The design and optimisation process of IMs were also considered in some detail. In addition, different sections of IMs were introduced with their tasks in details. The performance of IMs was also considered, in respect to losses, efficiency and thermal behaviour. In conclusion, WRIMs' design require more investigation to have better efficiency due to their application in the WECSs.

3. Wound Rotor Induction Machine Design

The design considerations for induction machines were discussed in the previous chapter. This chapter will describe the design algorithm by illustrating the sizing equations and analytical calculations for the wound rotor induction generator (WRIG). Three main operation modes are considered for the electromagnetic design in the WRIGs: generator at the power grid, generator to the autonomous load and brushless AC exciter (generator with rotor electric output). Here, the WRIG's rotor is assumed to be excited by a converter and the power can be delivered to the grid through either the stator or rotor.

3.1 Introduction

A machine model, an optimized method and other objective functions with a computer program are used to achieve the machine electromagnetic design. Electromagnetic design factors of WRIGs are named as follows: stator and rotor cores sizing, stator and rotor winding design, magnetization current calculation, equivalent circuit parameter determination, and efficiency computation.

3.2 Stator Design

The interior diameter of the stator depends on a factor known as shear rotor stress (f_{xt}) [25], [31], [38]. This shear rotor stress increases with torque and varies between 1.5 and 6N/cm^2 [123]. The shear rotor stress is used to calculate the stator interior diameter (D_{is}). To calculate D_{is}, the electromagnetic torque has to be estimated at maximum speed on the basis of the input power of the machine and expected efficiency. The electromagnetic power (S_{gN}) is as follows:

$$S_{gN} \approx \frac{S_{SN} + S_{RN}}{\eta_N} \tag{3.1}$$

where,

S_{gN}: Electromagnetic power;

S_{SN}: Power on stator side at unity power factor;

S_{RN}: Power on rotor side at unity power factor;

η_N: Expected efficiency;

The corresponding electromagnetic torque T_e is [40], [97]

$$T_e = \frac{S_{gN}}{2\pi\frac{f_1}{p_1}(1+|S_{max}|)} \quad 3.2$$

where,

f_1: Frequency;

p_1: The number of pole pairs;

S_{max}: Maximum slip;

The maximum slip is different with rated slip. S_{max} is used in order to design the machine based on maximum rotational speed. Therefore, the stator diameter D_{is} can be expressed as [39], [56]:

$$D_{is} = \sqrt[3]{\frac{2\times T_e}{\pi\times\lambda\times f_{xt}}} \quad 3.3$$

$$\lambda = \frac{l_i}{D_{is}}; \qquad 0.2 < \lambda < 1.5 \quad 3.4$$

where,

λ: The stack length ratio;

l_i: The stack length;

The stack length ratio is smaller corresponding to the larger number of poles.

The external stator diameter D_{out} based on the maximum airgap flux density per given magneto-motive force (mmf) is approximated in table 3.1 [3], [31], [38]. These values are measured in order to avoid saturation of the yoke.

Table 3.1 Outer to Inner Stator Diameter [31].

Number of pole pairs	2	4	6	8	≥10
D_{out}/D_{is}	1.65-1.69	1.46-1.49	1.37-1.40	1.27-1.30	1.24-1.20

The rated stator current at unity power factor in the stator I_{SN} is

$$I_{SN} = \frac{S_{SN}}{\sqrt{3}V_{SN}} \quad 3.5$$

where,

V_{SN}: Rated stator voltage;

The airgap flux density (B_g) is usually assigned between 0.65 and 0.8 and the airgap electromagnetic force (emf) E_S per phase is as follows [3], [39], [71]:

$$E_S = K_E \frac{V_{SN}}{\sqrt{3}}; \qquad \mathrm{K}_E = 0.97\ (0.97 < \mathrm{K}_E < 0.98) \tag{3.6}$$

where,

K_E : emf coefficient;

The pole pitch τ is calculated as follows:

$$\tau = \frac{\pi D_{is}}{2p_1} \tag{3.7}$$

The number of turns per phase is dependent on the emf per phase (E_S), pole pitch (τ), and winding factor (K_{W1}). The fundamental winding factor is calculated as follows [3], [25], [39]:

$$K_{W1} = \frac{sin\frac{\pi}{6}}{q_1 sin\frac{\pi}{6q_1}} sin\frac{\pi}{2}\frac{y}{\tau}; \qquad \frac{2}{3} \leq \frac{y}{\tau} \leq 1 \tag{3.8}$$

where,

q_1: The number of slots per pole per phase in the stator, which an integer for an integral slot winding machine.

$\frac{y}{\tau}$: The stator coil span/pole pitch ratio;

The number of turns (W_1) per phase is [3], [38]:

$$W_1 = \frac{E_S}{2\sqrt{2} f_1 W_1 K_{W1a} B_g \tau l_i} \tag{3.9}$$

Number of turns per coil (n_{c1}) is calculated as follows:

$$n_{c1} = \frac{W_1}{\left(\frac{2p_1 q_1}{a_1}\right)} \tag{3.10}$$

where, a_1 is the number current paths in the stator winding.

The stator slot pitch (τ_S) is:

$$\tau_S = \frac{\pi D_{is}}{m\ 2p_1 q_1} \tag{3.11}$$

where,

m: The number of phases;

The number of stator slots (N_s) is:

$$N_s = 2p_1 q_1 m \tag{3.12}$$

The stator conductor cross section (A_{cos}) is as follows:

$$A_{cos} = \frac{I_{SN}}{a_1 . j_{cos}} \quad 3.13$$

where,

j_{cos}: The stator current density;

The cooling system and cross-section of the conductors depend on the selected current densities in the stator and rotor of the machine. The useful slot area A_{su} is:

$$A_{su} = \frac{z_1 n_{c1} A_{cos}}{k_f} \quad 3.14$$

where,

z_1: The number of layers per slot in the rotor;

k_f: The slot fill factor;

In general, slot width (W_S) is 45 to 50 percent of slot pitch for WRIGs. The rectangular slot useful height (h_{SU}) is:

$$h_{SU} = \frac{A_{su}}{W_S} \quad 3.15$$

The airgap length (g) is [3], [38], [39]:

$$g = (0.1 + 0.012\sqrt[3]{S_{SN}})10^{-3} \quad 3.16$$

If the flux density in the stator's back iron (core) is assigned as B_{CS} then the height of the stator back iron (h_{CS}) is:

$$h_{CS} = \frac{B_g \tau}{\pi B_{CS}} \quad 3.17$$

The magnetically required outer diameter of the stator D_{outm} is

$$D_{outm} = D_{is} + 2(h_{SU} + h_{SW} + h_{cs}) \quad 3.18$$

where,

h_{SW} : The stator slot wedge, if used in the design;

As known, the flux and current density distribution in a conductor (or a group of conductors) flowed by a.c. currents and surrounded by a magnetic core with some airgaps can lead to skin effects. The skin effect increases the conductor's effective resistance at higher frequencies where the skin depth is smaller, as a result decreasing the effective cross-section of the conductor. The skin effect factor is calculated using a sequence of equations. Initially, it requires the calculation of a chording ratio, β [3], [25], [38]:

$$\beta = \sqrt{\frac{\omega_1 \mu_0 \sigma_{co}}{2} \frac{a_{ce}}{W_S}} \quad 3.19$$

where,

β: Chording ratio;

ω_1: Angular speed;

μ_0: Permeability of free space;

σ_{co}: Electrical conductivity;

a_{ce}: Conductor cross-sectional area;

The resistance ($\varphi(\xi)$) and slot leakage inductance ($\psi(\xi)$) correction coefficients are required to calculate the skin effect factor.

$$\varphi(\xi) = \xi \frac{sinh2\xi + sin2\xi}{cos2h\xi - cos\xi}$$
$$\psi(\xi) = 2\xi \frac{(sinh\xi + sin\xi)}{cosh\xi + cos\xi} \quad 3.20$$

where, $\xi = \beta \times h_c$ and h_c is conductor thickness. Furthermore, skin effect coefficient (K_{Rme}) is [3], [27], [39]:

$$K_{Rme} = \varphi(\xi) + \frac{m_e^2 - 1}{3} \psi(\xi) \quad 3.21$$

where m_e is the number of conductor strands. Furthermore, the additional skin effect coefficient (K_{rad}) is [3], [25], [38]:

$$K_{rad} = 4\beta^4 . h_c^4 (\frac{l_i}{l_{turn}})^2 n_{cn}^2 \frac{(1 + cos\gamma)^2}{4}$$
$$\gamma = \left(1 - \frac{y}{\tau}\right) \frac{\pi}{2} \quad 3.22$$

where l_{turn} is the coil length. The total skin effect factor (K_R) is [3], [25], [38]:

$$K_R = 1 + (K_{rme} - 1) \frac{l_i}{l_{turn}} + K_{rad} \quad 3.23$$

The total skin effect factor is very important in the large machines due to their loss calculations.

3.3 Rotor Design

The rotor design is based on maximum speed and power delivered, P_{RN}, at the maximum corresponding rotor voltage ($V_{RN} \leq V_{SN}$). In addition, the unity power factor in the stator is assumed to design the WRIG. Therefore, all the reactive power is provided

by the rotor. Consequently, the rotor also provides magnetization of the current in the WRIG.

For $V_{RN} = V_{SN}$ at S_{max}, the turns ratio between the rotor and stator K_{RS} is obtained [3], [31] by considering equations 3.6 and 3.9 as follow:

$$K_{RS} = \frac{W_2 K_{W2}}{W_1 K_{W1}} = \frac{1}{|S_{max}|} \quad 3.24$$

where,

W_2: The rotor number of turns per phase;

K_{W2}: The rotor winding factor;

The rated stator current referred to the rotor side (I'_{SN}) is:

$$I'_{SN} = \frac{I_{SN}}{K_{RS}} \quad 3.25$$

The rated magnetization current (I'_m) depends on the machine power and the number of poles. The referred magnetization current can be expressed as:

$$I'_m = K_m I'_{SN} \quad 3.26$$

where, K_m is the magnetization current coefficient and it varies between 0.1 and 0.3. The magnetization current coefficient is initially assumed to calculate the rotor current, however, it will ultimately be adjusted through the final calculation. The actual rotor current (I^R_{RN}) at maximum slip is [3], [31]:

$$I^R_{RN} = \sqrt{I'^2_{SN} + I'^2_m} = I'_{SN}\sqrt{1 + K^2_m} \quad 3.27$$

The rotor power factor $cos\varphi_{2N}$ is:

$$cos\varphi_{2N} = \frac{P_{RN}}{\sqrt{3}\, V_{RN} I^R_{RN}} \quad 3.28$$

The rotor winding factor (K_{W2}) is calculated similarly to the stator winding factor [3], [25], [39].

$$K_{W2} = \frac{sin\frac{\pi}{6}}{q_2 sin\frac{\pi}{6q_2}} sin\frac{\pi}{2}\frac{y_R}{\tau} \quad 3.29$$

Where, q_2 is the number of the rotor slots per pole per phase. Hence, the number of the rotor slots (N_r) is:

$$N_r = 2p_1 q_2 m \quad 3.30$$

The rotor turns per phase (W_2) is [3], [38]:

$$W_2 = \frac{W_1 K_{W1} K_{RS}}{K_{W2}} \quad 3.31$$

The number of turns per coil (n_{c2}) is:

$$n_{c2} = \frac{W_2}{\left(\frac{2p_1 q_2}{a_2}\right)} \quad 3.32$$

where a_2 is the number of current paths in the rotor winding. Also, the rotor slot pitch (τ_R) is calculated in a similar to stator slot pitch as:

$$\tau_R = \frac{\pi D_{is}}{m 2 p_1 q_2} \quad 3.33$$

The rotor conductor cross-section (A_{cor}) is:

$$A_{cor} = \frac{I_{RN}}{a_2 . j_{cor}} \quad 3.34$$

where, j_{cor} is the rotor current density. The rotor useful slot area (A_{ru}) is:

$$A_{ru} = \frac{z_2 n_{c2} A_{cor}}{k_f} \quad 3.35$$

where,

z_2: The number of layers per slot in the rotor;

The rotor slot width (W_R) is usually between 45% and 55% of the rotor slot pitch for WRIGs. Then, the rotor slot's height (h_{RU}) is:

$$h_{RU} = \frac{A_{ru}}{W_R} \quad 3.36$$

The minimum rotor teeth width (W_{tRmin}) is [3], [25], [27], [39]:

$$W_{tRmin} = \frac{\pi(D_{is} - 2(g + h_{RU} + h_{RW}))}{N_R} - W_R \quad 3.37$$

where, h_{RW} is the rotor slot wedge. Then, the maximum rotor teeth flux density (B_{tRmax}) is:

$$B_{tRmax} = \frac{B_g \tau_R}{W_{tRmin}} \quad 3.38$$

If B_{cr} is assigned as the rotor core flux density, the rotor back iron radial path (h_{CR}) is:

$$h_{CR} = \frac{B_g \tau}{\pi B_{cr}} \quad 3.39$$

Consequently, the maximum shaft diameter (D_{IR}) is:

$$D_{IR} = D_{IS} - 2(g + h_{RU} + h_{RW} + h_{CR}) \quad 3.40$$

If the shaft diameter passes its maximum value, then the flux density increase in the rotor core and rotor teeth. This results to increase in core loss and might also cause saturation either in the rotor core or rotor teeth.

3.4 Magnetization Current

So far the stator and rotor designs are discussed. This section illustrates analytical computations for the magnetization current. The flux path in the rotor and stator of a typical wound rotor induction machine is shown in Figure 3.1. Applying Ampere's Circuit law along half of the contour of the main flux, yields the following [3], [25], [38]:

$$F_m = (F_{AA'} + F_{AB} + F_{BC} + F_{A'B'} + F_{B'C'}) \quad 3.41$$

where,

$F_{AA'}$: The airgap mmf;

F_{AB}: The stator teeth mmf;

F_{BC}: The stator yoke mmf;

$F_{A'B'}$: The rotor teeth mmf;

$F_{B'C'}$: The rotor yoke mmf;

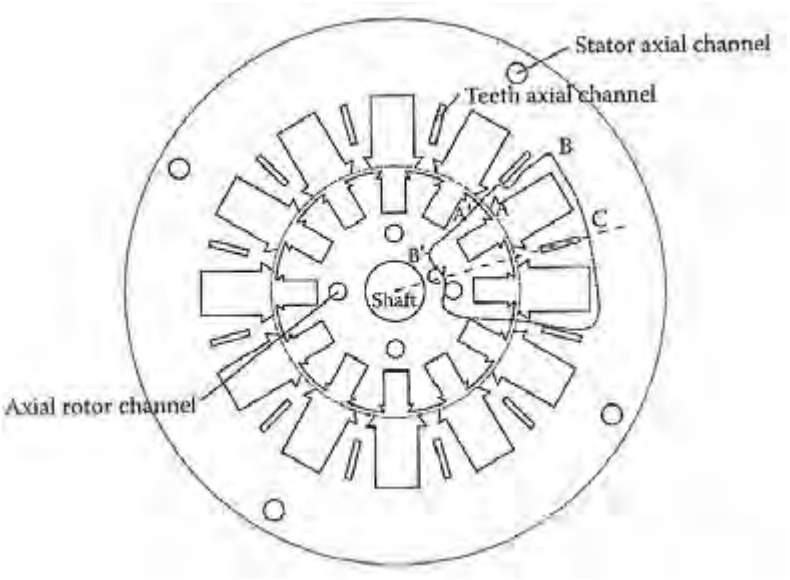

Fig. 3.1 Main flux path [31].

Carter's coefficient is used to determine a modified effective airgap length due to the effects of slot openings in a machine. The Carter's coefficient for an induction machine is the product of that for the stator and rotor of the machine, which can be expressed as [3], [25], [38], [39]:

$$K_C = K_{C1}K_{C2} \tag{3.42}$$

$$\text{where, } K_{C1,C2} = \frac{1}{1-\gamma_{1,2}\frac{g}{2\tau_{s,r}}} \text{ and } \gamma_{1,2} = \frac{\left(\frac{2W_{S',R'}}{g}\right)^2}{5+\frac{2W_{S',R'}}{g}} \tag{3.43}$$

The equivalent slot openings, with magnetic wedges, $W_{S'}$ and $W_{R'}$ are:

$$W_{S'} = \frac{W_S}{\mu_{RS}} \text{ and } W_{R'} = \frac{W_R}{\mu_{RR}} \tag{3.44}$$

where, μ_{RS} and μ_{RR} are the relative permeabilities of the magnetic wedges associated with the stator and rotor slots respectively. The airgap mmf can therefore be expressed as [3], [25], [38], [39]:

$$F_{AA'} = gK_C\frac{B_g}{\mu_0} \tag{3.45}$$

The flux densities in the stator core and teeth are required to calculate their respective mmfs. The stator core flux density is assigned as B_{CS} and the flux density in the teeth (B_{ts}) is:

$$B_{ts} = B_g \times \frac{\tau_S}{W_{ts}} \tag{3.46}$$

Table 3.2 shows magnetization curve data of silicon-steel lamination at 50Hz with 0.5mm thickness which it has 3.5% silicon. This lamination is simply used as an illustrative example. From table 3.2, the field intensities for B_{ts} and B_{CS} can be determined. As a result, the stator teeth (F_{AB}) and core (F_{BC}) mmfs are:

$$F_{AB} = H_{ts}(h_{su} + h_{sw}) \tag{3.47}$$

$$F_{BC} \approx H_{CS}.l_{csav} \tag{3.48}$$

where H_{CS} is selected from table 3.2 according to the stator core flux density and l_{csav} is the average length of stator core flux path.

$$l_{csav} \approx \frac{2}{3}\frac{\pi(D_{out}-h_{cs})}{2.2p_1} \tag{3.49}$$

The average rotor teeth flux density is required to calculate the mmf in the rotor tooth portion. This can be expressed as follows:

$$B_{trt} = B_{g1} \times \frac{\tau_R}{W_{tR}},\ B_{tRm} = B_{g1} \times \frac{\tau_R}{W_{tRm}} \text{ and } B_{tRb} = B_{g1} \times \frac{\tau_R}{W_{tR}}$$
$$B_{tR} = \frac{B_{tRt}+B_{tRb}+4B_{tRm}}{6} \tag{3.50}$$

where,

B_{tRt}: The top rotor tooth flux density;

B_{tRm}: The middle rotor tooth flux density;

B_{tRb}: The bottom rotor tooth flux density;

H_{tr} is drived from table 3.2 and the rotor teeth mmf ($F_{A'B'}$) is:

$$F_{A'B'} = H_{tr}(h_{RU} + h_{RW}) \quad 3.51$$

The rotor back iron mmf is calculated similar to that of the stator core, as:

$$F_{B'C'} = H_{CR}.l_{CRav} \quad 3.52$$

where, H_{CR} is selected from table 3.2 according to rotor core flux density and l_{CRav} is the average length of the rotor core flux path [27], [31], [38]:

$$l_{CRav} = \frac{2}{3}\frac{\pi(D_{shaft}+h_{CR}+0.01)}{2.2p_1} \quad 3.53$$

the no-load rotor current (I_{R0}) is [3], [31]:

$$I_{R0} = F_m \frac{\pi.p_1}{3W_2.K_{W2}\sqrt{2}} \quad 3.54$$

Table 3.2 Lamination magnetization curve $\mathbf{B_m}(\mathbf{H_m})$.

$B[T]$	$H[\frac{A}{m}]$	$B[T]$	$H[\frac{A}{m}]$
0.05	22.8	1.05	237
0.1	35	1.1	273
0.15	45	1.15	310
0.2	49	1.2	356
0.25	57	1.25	417
0.3	65	1.3	482
0.35	70	1.35	585
0.4	76	1.4	760
0.45	83	1.45	1050
0.5	90	1.5	1340
0.55	98	1.55	1760
0.6	106	1.6	2460
0.65	115	1.65	3460
0.7	124	1.7	4800
0.75	135	1.75	6160
0.8	148	1.8	8270
0.85	162	1.85	11170
0.9	177	1.9	15220
0.95	198	1.95	22000
1.0	220	2.0	34000

As considered, the rated magnetization current is determined by assigning K_m. After sizing the stator and the rotor, the magnetization mmf can be recalculated as follow:

$$K_m = \frac{I_{R0}}{I'_{SN}} \tag{3.55}$$

If the K_m become greater than the assigned value, the design process requires to be repeated by assigning new assumptions. However, the smaller K_m leaves more room for saturation in the stator teeth that can be used for the cooling system.

The saturation factor (K_S) accounts for all iron mmfs as divided by the airgap mmf. The saturation factor is expressed as follow:

$$K_S = \frac{F_{AB}+F_{BC}+F_{A'B'}+F_{B'C'}}{F_{AA'}} \tag{3.56}$$

For normal IMs, the saturation factor should be $K_S \leq 1$ and if it is $1 < K_S < 1.6$, then the IM is mildly saturated [3].

3.5 Reactances and Resistances

The main WRIG parameters are the magnetization reactance X_m, the stator and rotor resistance R_s and R_r, and leakage reactances X_{sl} and X_{rl}, referred to the stator. The magnetization reactance expression is [25], [31], [38]:

$$X_m = \omega_1 L_m \tag{3.57}$$

where magnetization inductance (L_m) is:

$$L_m = \frac{6\mu_0(W_1 K_{WS})^2 \tau l_i}{\pi^2 p_1 g K_C (1+K_S)} \tag{3.58}$$

The stator resistance R_S per phase is [3], [31], [39]:

$$R_S = \rho_{co100^\circ} \frac{W_1.2}{A_{cos}} \left(l_i + l_{fs}\right) \frac{1}{a_1} \tag{3.59}$$

where, l_{fs} is the end winding length as shown in figure 3.2 and ρ_{co100° is copper resistivity at 100C°, which can be expressed as [31], [97]:

$$l_{fs} = 2(l_l + l_{l'}) + \pi h_{st} = 2\left(l_l + \frac{\beta_s \tau}{2cos\alpha}\right) + \pi h_{ts} \text{ and } \beta_s = \frac{y}{\tau} \tag{3.60}$$

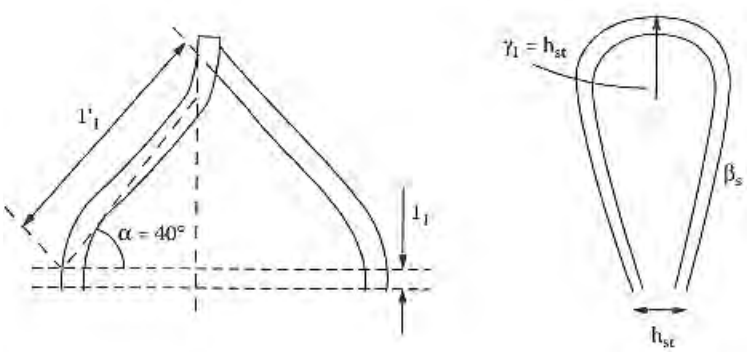

Fig. 3.2 Stator coil end connection [31].

The stator leakage reactance (X_{sl}) is:

$$X_{sl} = \omega_1 L_{sl} \tag{3.61}$$

where L_{sl} is the stator leakage inductance [3], [25], [31].

$$L_{sl} = \mu_0 (2n_{c1})^2 l_i (\lambda_s + \lambda_{end} + \lambda_{ds}) \frac{N_s}{m\, a_1{}^2} \tag{3.62}$$

The slot permeance coefficient (λ_s), the end connection permeance coefficient (λ_{end}) and the differential leakage permeance coefficient (λ_{ds}) are [3], [25], [31], [38]:

$$\lambda_s = \frac{h_{su}}{3W_s} + \frac{h_{sw}}{W_s'} \tag{3.63}$$

$$\lambda_{end} = 0.34\, q_1 \frac{l_{fs} - 0.64\beta_s \tau}{l_i} \tag{3.64}$$

$$\lambda_{ds} = 0.9\tau_s\, (q_1\, K_{W1})^2\, K_{01} \frac{\sigma_{ds}}{K_C\, g} \tag{3.65}$$

where, σ_{ds} is the stator differential leakage coefficient which depends on number of slots per phase per pole and chording ratio β as illustrated in figure 3.3. The term λ_{ds} generally includes the zigzag leakage flux.

The rotor end connection length l_{fr} can be determined in a similarly manner to that of the stator [3], [31], [38]:

$$l_{fr} = 2\left(l_l + \frac{\beta_r \tau}{2cos\alpha}\right) + \pi(h_{RU} + h_{RW}); \tag{3.66}$$

and the actual rotor resistance (R_R^R) at 100C° is:

$$R_R^R = \rho_{co100°} \frac{2.W_2}{A_{cor}} \left(l_i + l_{fr}\right) \tag{3.67}$$

L_{rl}^R is rotor leakage inductance is [3], [31], [38]:

$$L_{rl}^R = \mu_0 (2n_{c2})^2 l_i (\lambda_{SR} + \lambda_{endR} + \lambda_{dR}) \frac{N_R}{m} \tag{3.68}$$

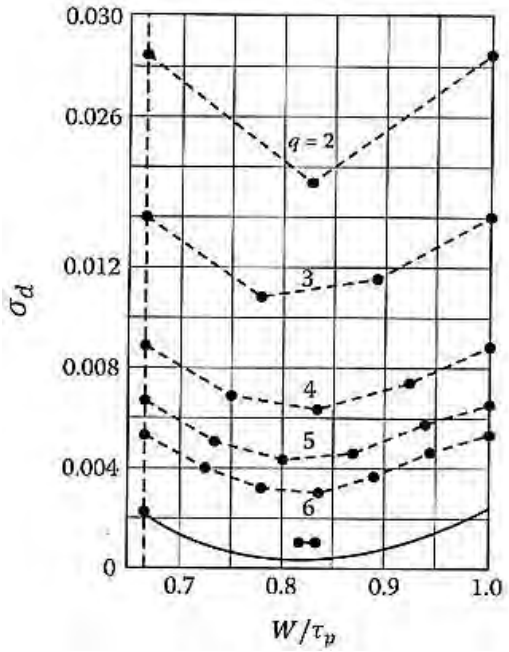

Fig. 3.3 Differential leakage Coefficient $\boldsymbol{\sigma_d}$.

Similar to the stator, the rotor slot permeance coefficient (λ_{SR}), end connection permeance coefficient (λ_{endR}) and differential leakage permeance coefficient (λ_{dR}) are as follows:

$$\lambda_{SR} = \frac{h_{RU}}{3W_R} + \frac{h_{RW}}{W_R'} \tag{3.69}$$

$$\lambda_{endR} = 0.34 q_2 \frac{l_{fr} - 0.64\beta_r \tau}{l_i} \tag{3.70}$$

$$\lambda_{dR} = 0.9\tau_R \, (q_2 K_{W2})^2 K_{02} \, \frac{\sigma_{dR}}{K_C g}; \; K_{02} = 1 - 0.033 \left(\frac{W_R'}{g\tau_R}\right); \tag{3.71}$$

where, the rotor differential leakage coefficient (σ_{dR}) is determined the same as σ_{dS} from figure 3.3. Therefore, the actual rotor leakage reactance is:

$$X_{rl}^R = \omega_1 {L_{rl}}^R \tag{3.72}$$

The turns ratio (K_{RS}) can be used to transfer these value to the stator side. The rotor resistance is usually larger than the stator resistance due to greater current density.

3.6 Electrical Losses and Efficiency

The equivalent circuit can be used to determine the power flow (depends on the machine operating mode) and also calculate efficiency. Stator (P_{cos}), rotor (P_{cor}) and slip rings (P_{sr}) losses are calculated as follows:

$$P_{cos} = 3K_R R_S I_{SN}^2 \tag{3.73}$$

$$P_{cor} = 3R_R^R I_{RN}^2 \quad 3.74$$

$$P_{sr} = 3V_{SR} I_R^R \quad 3.75$$

where,

V_{SR}: Voltage drop between the brush and slip-ring;

The stator and rotor core losses are calculated by means of classical core loss formulations developed by Steinmetz. To calculate the stator fundamental core losses, the stator teeth and back iron weight G_{ts} and $G_{cs}$are required [3], [25], [31]:

$$G_{ts} = \left\{\frac{\pi}{4}\left[\left(D_{is} + 2(h_{su} + h_{sw})\right)^2 - D_{is}^2\right] - N_s \times (h_{su} + h_{sw}) \times W_s\right\} l_i \gamma_{iron} \quad 3.76$$

$$G_{cs} \approx \pi(D_{out} - h_{cs}) \times h_{cs} \times l_i \times \gamma_{iron} \quad 3.77$$

The fundamental core losses of the stator may be effected by mechanical machining. These impacts are considered by using as K_t (1.6 to 1.8) as tooth fudge factor and K_y (1.3 to 1.4) as yoke fudge factor [3], [25], [31].

$$P_{irons} = P_{\frac{10}{50}}\left(\frac{f_1}{50}\right)^{1.5}\left(K_t B_{ts}^2 G_{ts} + K_y B_{cs}^2 G_{cs}\right) \quad 3.78$$

The rotor core losses may be calculated in a similar manner [3], [31], [38].

The stray load losses include the surface and pulsation additional core losses (P_{ad}). These losses depend on the ratio of the slot opening on the airgap in the stator and in the rotor. These losses can be counted as 5% of the stator rated power. Thus, the total electrical losses ($\sum P_e$) are:

$$\sum P_e = P_{cos} + P_{cor} + P_{irons} + P_{ironr} + P_{ad} + P_{sr} \quad 3.79$$

The mechanical losses (friction and windage losses) are negligible, however, they can count less than 5% of the total power.

The electrical efficiency is:

$$\eta_e = \frac{P_{SN} + P_{RN}}{P_{SN} + P_{RN} + \sum P_e} \quad 3.80$$

3.7 Analysis of the Reference-DFIG

The main design equations of a wound rotor induction generator were presented in the preceding sections of this chapter. Several approaches can be used to conduct analytical design of the machine. In this section, a reference machine is presented with specifications in table 3.3 from [31]. The design details of the reference-DFIG are illustrated in appendix A. Ansys Maxwell 2D is used to validate the design of the machine.

The rotor of the machine is assumed to be excited by a converter and the rated speed is assumed to be 1750rpm.

Table 3.3 The reference-DFIG specifications.

Specification	Symbol	Quantity
Power[MW]	P	2.5
Efficiency[%]	η	95.8
Voltage[V]	V_{SN}	690
Poles	$2.p_1$	4
Phase	m	3
Synchronous Speed[rpm]	n_{1N}	1500
Frequency[Hz]	f_1	50
Maximum Slip	S_{max}	±0.25
Electromagnetic power[MW]	$S_{gN} = \frac{P}{0.96}$	2.604
Stator power[MW]	S_{SN}	2
Rotor power[MW]	$S_{RN} = S_{SN}\lvert S_{max}\rvert$	0.5

The current densities, flux lines, and flux densities are illustrated in figures 3.4 and 3.5, respectively.

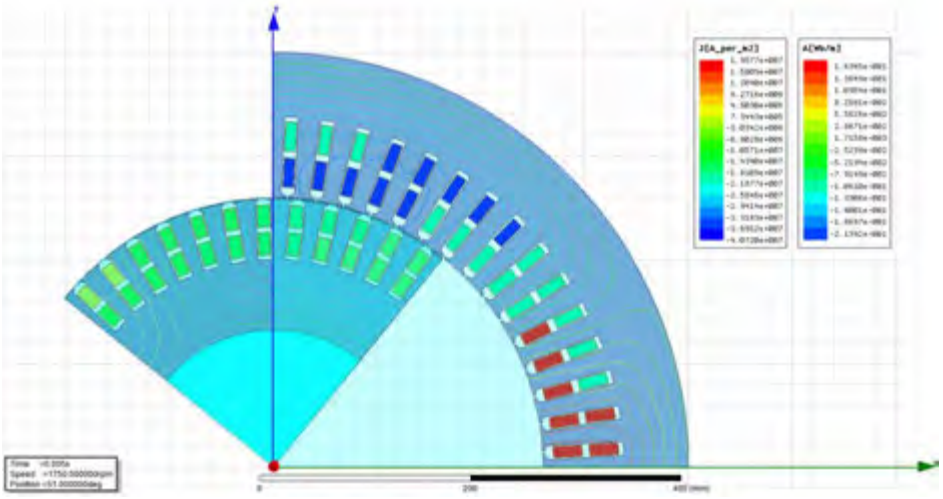

Fig. 3.4 The flux lines and the current densities in the stator and the rotor of the reference-DFIG.

The mean current densities in the stator and rotor are assigned as $6.5A/mm^2$ and $8A/mm^2$ respectively, based on normal air cooling system. The mean stator and rotor flux density are $1.8T$ and $1.5T$, respectively. The DFIG's behaviour is defined according its stator's outputs. The 3-phase stator current and voltage graphs are shown in figures 3.6 and 3.7. The peak current and voltage are approximately 1000A and 690V in steady-state, respectively.

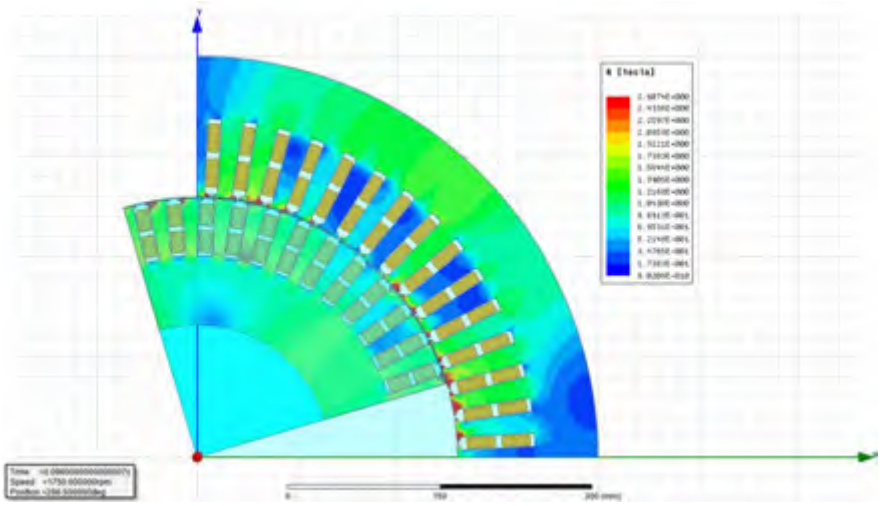

Fig. 3.5 The flux densities in the stator and the rotor of the reference-DFIG.

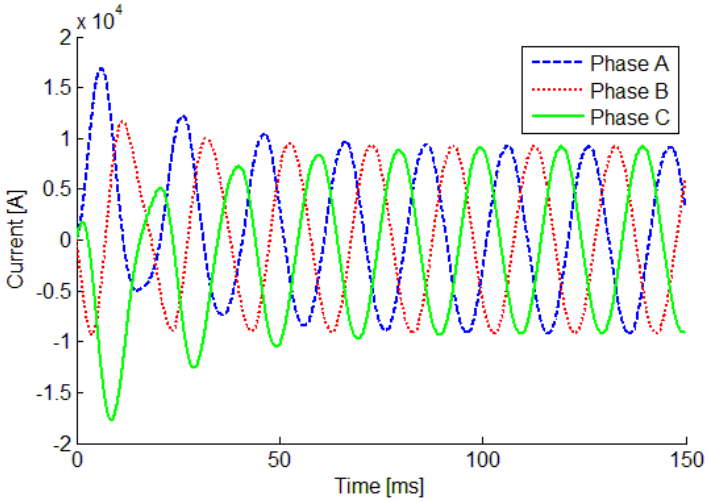

Fig. 3.6 The reference-DFIG 3-phase stator current.

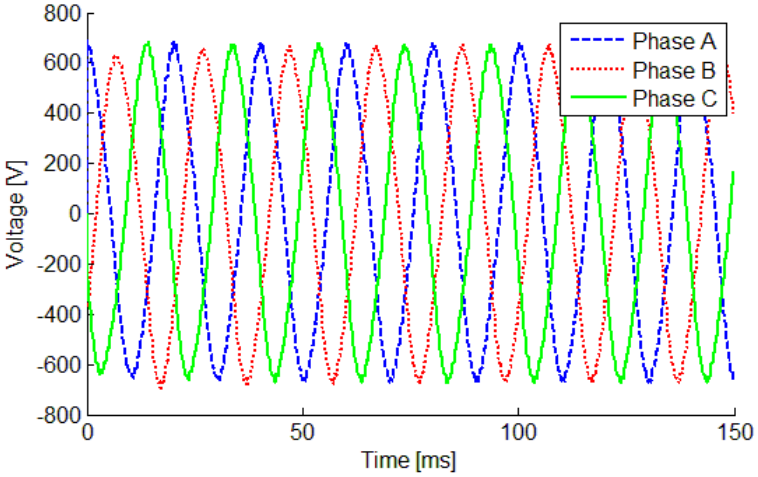

Fig. 3.7 The reference-DFIG 3-phase stator voltage.

3.8 Conclusion

The main design equations of a wound rotor induction machine were presented in this chapter. This included the sizing detailed design equations, loss calculations and equivalent circuit parameters. The design of a reference-DFIG is presented and validated by means of numerical finite element analysis (FEA). The reference-DFIG will be used in the reminder of the thesis to design and then compare with the micro-DFIG.

4. Wind Energy Conversion System with a DFIG

The design algorithm and sizing equations have been presented in the previous chapter. As noted, the design algorithm begins with several assumptions according to the initial specifications. Therefore, it is important to uncover the optimum specifications of the generator such as voltage, speed, and rated power in the wind energy conversion system (WECS). This chapter begins by illustrating the trends of wind generators output power since they have been manufactured in order to picture their current status. Then, it continues by discussing the advantages and disadvantages of different speeds (different number of poles) and voltages (low and medium voltages) of the WECS components to discover the optimum alternatives at present.

4.1 Introduction

It is evident that direct-drive generators are ideal for the wind energy system due to the challenges caused by the drive-train in terms of cost and efficiency for the system. However, research in the area of direct-drive DFIGs has shown that the technology is not feasible for wind applications due to winding constraints of the design [31]. In addition, wind generators can connect to the grid without transformers if they can generate the power at medium voltage or even high voltage. This will decrease the current value and reduce the generator copper losses, which will improve the efficiency of WECS [1], [124], [125]. Consequently, the question will arise regarding which combination is best if it is possible to design and prototype each part of the WECS (generator, gearbox, converter, etc.).

4.2 Wind Energy System Output Power Trend

Wind turbines are available with horizontal and vertical axes in the market. The trend of wind turbines output power from 1980 to 2014 is shown in figure 4.1. The figure indicates commercial turbines in utility-scale, land-based, and offshore wind farms. It also presents that a typical land-based turbine has a rating of between 1.5 MW and 1.8 MW, and offshore turbines have a rating from 3.6 to 5.0 MW, in 2005. Wind generators on a scale of 7.5 to 10 MW are considered for offshore projects more recently. Ultimately, it shows that the structural cost of wind turbines encourage manufacturers to prototype wind generators with larger output power over time [126].

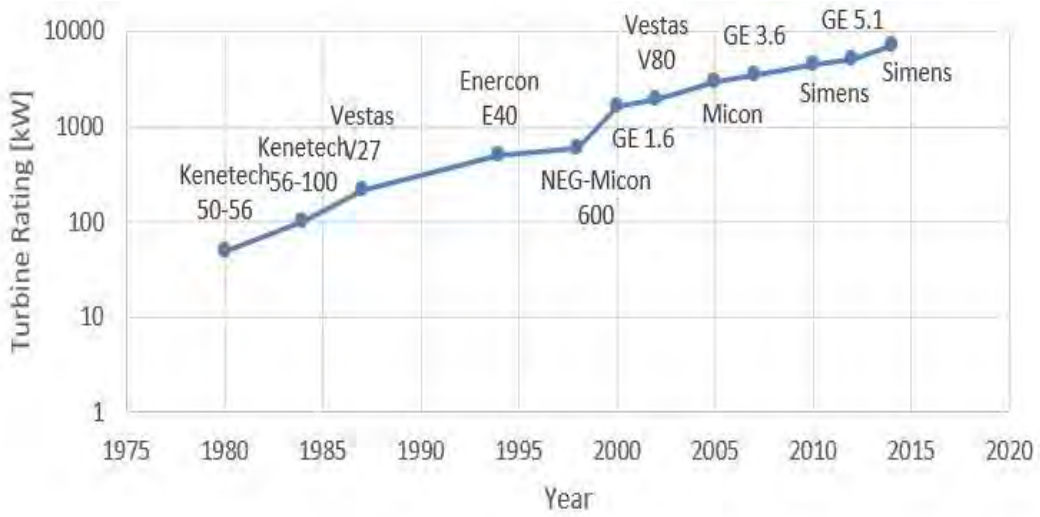

Fig. 4.1 Wind turbine rating growth.

4.3 Wind Energy System Topologies

Fixed and variable speeds are two operation methods for wind turbines. Fixed speed wind turbines are simple, robust and reliable. In addition, they are less expensive when compared with variable speed wind turbines. Conversely, their disadvantages include an uncontrollable reactive power consumption, mechanical stress and limited power quality control. Electrical power fluctuation may transmit to the grid through fixed speed wind turbines. This may cause large voltage fluctuations in weak grids. As a result, significant line losses will occur [1], [127], [128]. The variable-speed wind turbines are capable of having a maximum efficiency over a wide range of wind speeds. This means that the rotational speed ω of the wind turbine will be able to adjust to the wind speed v in the variable speed wind turbine in contrast to the fixed wind turbine. In contrast with a fixed-speed system, a variable-speed system keeps the generator torque fairly constant and the variations in wind are absorbed by changes in the generator speed. Increased energy captured, better power quality and less mechanical stress make variable speed wind turbines attractive for the industry. The disadvantages of variable wind turbines are losses in power electronics, the use of more components and the increased cost of equipment because of the power electronics.

4.4 Wind Turbine Components

The properties of WECS components will be present in the sections to follow in order to investigate the optimum combination.

4.4.1 Gearbox

The wind turbine's rotor turn speed is low, thus, its drive train includes a gearbox which will justify the input speed in order to achieve the rated operation speed of the generator. It is important to avoid under-designing the gearbox and adjust the design according to its operating conditions. The gearbox is usually heavy and expensive compared to the other components of the wind turbine. Gearboxes are divided into two basic types for WECS: (1) parallel-shaft gearboxes and (2) planetary gearboxes [1], [129]–[131]. Parallel gearboxes have two or more parallel shafts which carry the gears. For instance, a single-stage parallel gearbox has two shafts which each have a gear. These shafts are known as low-speed and high-speed shafts. The gear on the low-speed shaft is larger than that of the high-speed shaft. Moreover, the low-speed shaft is usually connected to the rotor and the high-speed shaft to the generator in the WECS. On the other hand, planetary gearboxes have coaxial input and output shafts. In this gearbox, the loads on each gear are reduced because there are multiple pairs of gear teeth meshing at any time. It causes the gearbox to be relatively light and compact. A planet carrier includes at least 3 identical small gears which are stiffly connected to the lower speed shaft. These small gears are known as planet in the career and they are assembled on short-shaft. These planets mesh with a large-diameter internal or ring gear and a small-diameter sun gear. The sun gear is connected to a high-speed shaft [132]. Ultimately, the gearbox is designed to have a lower cost. Hence, the number of stages in a gearbox is important, primarily because it affects the size, weight, and in the end, the cost of the gearbox. Also, the maintenance of the gearbox becomes more difficult when the number of stages increases. The gearbox's cost should not cause a reduction in the reliability of the gearbox. A single-stage planetary gear configuration is considered in this chapter.

$$G_{gear} = 3.2\frac{T_m\, F_s\, F_w}{1000} \tag{4.1}$$

Where T_m is the output torque of gearbox (*N.m*) and F_s is the service factor considering surface damage and failure in metal fatigue. The weight factor F_w is given as [133]:

$$F_w = \frac{1}{Z} + \frac{1}{Z\, r_w} + r_w + r_w^2 + 0.4\frac{1 + r_w}{Z} \times (r_{ratio} - 1)^2 \tag{4.2}$$

Where Z in the planetary wheel number in the stage; the wheel ratio $r_w = \frac{r_{ratio}}{2} - 1$, and r_{ratio} is single-stage gear ration. The cost of a single-stage gearbox C_{gear} is roughly estimated by the weight G_{gear} and specific cost c_{gear} as [133]:

$$C_{gear} = c_{gear}\, G_{gear} \tag{4.3}$$

The losses in a gearbox can be divided into two different parts: these include gear teeth losses and bearing losses, which depend on the rotational speed. The main losses in a

gear box are proportional to the shaft speed.

$$P_{gear} = k_g \, P_N \frac{n_r}{n_{rN}} \qquad 4.4$$

Where k_g is a constant for the speed-dependent losses (in this case, it is 1.5 % for single-stage gearbox), P_N is the rated power of wind turbines, n_{rN} is the rated rotor speed. Table 4.1 shows the coefficients for a single-stage gearbox.

Table 4.1 Single-stage planetary gearbox modeling

Single-stage gearbox	
Gearbox service factor F_s	1.25
Planet wheel number Z	8
Cost per weight c_{gear} [$/kg]	8
Losses percentage at the rated power k_g	1.5%

4.4.2 Converters

Today, variable-speed wind turbine generator systems may use many different types of converters. The power converters are a combination of basic elements such as diodes and electronic switches, such as conventional or switchable thyristors and transistors. The converters are characterized as either grid-commutated or self-commutated converters [134]. A thyristor is a common type of grid-commutated converter. It is highly reliable and well-priced, but it generates current harmonics and consumes reactive power. Typical self-commutated converters consist of either gate turn-off (GTO) thyristors or transistors. The advantage of self-commutated converters is their high switching frequencies. Harmonics can be filtered out more easily and thus their disturbances to the network can be reduced to low levels [135], [136]. As indicated in table 4.2, the common switching frequency of an IGBT is between 2 and 20 kHz. In contrast, GTO converters are limited to about 1kHz [137], [138].

Table 4.2 Switches: maximum ratings and characteristics.

	Switch type				
	GTO[6]	IGCT[7]	BJT[8]	MOSFET[9]	IGBT[10]
Voltage [V]	6000	6000	1700	1000	6000
Current [A]	4000	2000	1000	28	1200
Switching frequency [kHz]	0.2-1	1-3	0.5-5	5-100	2-20
Drive requirements	High	Low	Medium	Low	Low

Self-commutated converters are divided into current source converters (CSCs) and voltage source converters (VSCs). These converters are able to control both the

[6] Gate Turn-Off
[7] Integrated Gate Commutated Thyristors
[8] Bipolar Junction Transistors
[9] Metal Oxide Semiconductor Field Effect Transistors
[10] Insulated Gate Bipolar Transistors

frequency and the voltage. VSCs and CSCs are able to provide smooth switched voltage and current waveforms, respectively. They can be used with different policies: six-step, pulse amplitude modulated (PAM) or pulse width modulated (PWM). By using the PWM technique, the low-frequency harmonics are eliminated and the frequency of the first higher-order harmonics lie at approximately the switching frequency of the inverter or rectifier. Generally, a power electronic system is adapted to adjust the generator voltage and frequency in the variable-speed wind turbine. The system includes devices such as soft-starters, rectifiers, inverters and frequency converters. There are various methods to merge a rectifier and an inverter into a frequency converter. There are five applicable technologies for controlling variable speed machines: back-to-back, multilevel, tandem, matrix and resonant.

It is clear that the back-to-back converter configuration is fitted to current WECSs (figure 4.2). However, the control strategy is gradually moving toward the matrix and multilevel converter. The back-to-back PWM converter of a DFIG consists of a rotor-side voltage converter (RSC) and a grid-side converter (GSC) [139]. With the rotor-side converter, it is possible to control the torque or the speed of the DFIG as well as the power factor at the stator terminals, while the main objective for the grid-side converter is to keep the DC-link voltage constant regardless of the magnitude and direction of the rotor power. The grid-side converter works at the grid frequency and the rotor-side converter works at different frequencies, depending on the wind speed [140]. The matrix converters are better in terms of efficiency and lifetime compared to back-to-back converters with the DC link capacitor [141], [142]. However, protection in a fault situation, higher conduction losses, and the limitation of the output voltage converter are the disadvantages of the matrix converter [143], [144].

The losses of the converter can be divided into switching losses and conducting losses. The switching losses of the switches are the turn-on and turn-off losses. For the diode the switching losses mainly consist of turn-off losses, i.e., reverse-recovery energy. The turn-on and turn-off losses for the switches and the reverse-recovery energy loss for a diode can be found from data sheets. The conducting losses arise from the current through the transistors and diodes [8]. Here, the losses of converter is calculated as follow:

$$P_{convN} = k_c \, P_N \tag{4.5}$$

The converter cost can also be calculated by their cost coefficient which varies by the market rate. Table 4.3 illustrates the converter coefficient which is employed in this chapter.

Table 4.3 Back-to-back converter modeling.

Converter coefficients	
Converter losses percentage k_c	3%
Specific cost of power electronic system [$/kW]	28
Specific cost of sub electrical system [$/kW]	38

4.4.3 Generator

Several types of generators may be used in wind turbines such as the squirrel cage induction generator (SCIG), the wound rotor induction generator (WRIG) or the synchronous generator and the permanent magnet synchronous generator (PMSG). However, the PMSGs and the doubly-fed Induction generators (DFIGs) dominate the market due to their many advantages.

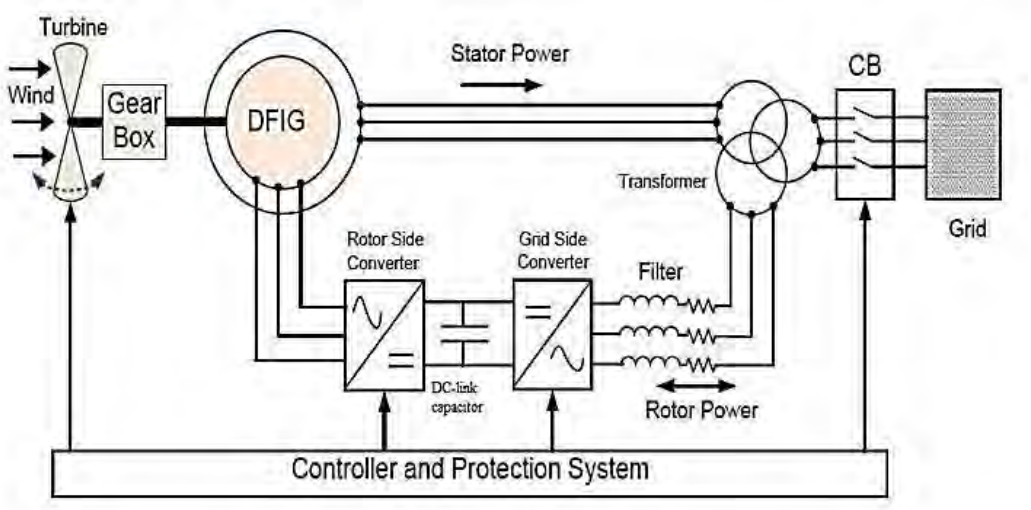

Fig. 4.2 Typical back-to-back arrangement of the converter circuits to control power flow.

PMSGs are suggested for use in wind turbines because of their property of self-excitation, which allows an operation at a high power factor and a high efficiency [145]. The efficiency is higher in the permanent magnet (PM) machines than in IMs, as the excitation is provided without any energy supply. Permanent magnet materials are rare and as a result, they are expensive. Also, it is difficult to work with permanent magnets materials due to their sensitivity to heat, shock and stress. PM machines are required to be driven by a full-scale converter in order to adjust their voltage and frequency to the grid, which ultimately will increase the cost. The disadvantage of the PMSGs is the difficulty during start-up, synchronization and voltage regulation [18], [146]. Also, their synchronous nature can cause a very stiff performance in the case of an external short-circuit and unsteady wind speed [147].

As mentioned earlier, the DFIG consists of a WRIG with the stator windings directly connected to the constant-frequency 3-phase grid and with the rotor windings mounted

to a bidirectional back-to-back IGBT voltage source converter. The capability of controlling the reactive power as well as controlling active and reactive power separately are the DFIG's advantages. The DFIGs are also able to deal with active power and reactive power through their rotor by the grid-side converter as well as their stator. However, the grid-side converter might become costly for a weak grid with voltage fluctuations because they are designed based on the maximum slip in order to transfer an amount of reactive power between the grid and the DFIG. Thus, the cost of the converter increases when the speed range becomes wider. The DFIG requires slip rings which decrease its efficiency [1], [148].

4.5 Analytical Result and Comparison

4.5.1 Analytical Results

A 736 kW, 4 pole, 4 kV, delta-connected wound rotor induction generator (WRIG) was adapted from [3]. The WRIG is redesigned and optimized by means of an analytical design algorithm and optimized with a genetic-algorithm. The design and optimization procedure was validated by providing specifications for a machine similar to that presented in [3]. The reference design and that of [3] are presented in table 4.2. It shows five alternative wind generator designs (A, B, D, E, and F) which were generated by the above mentioned design and optimization procedure. These designs are variations of the reference design (c) and details for comparison are provided in table 4.2. In particular, output power is the same, but the number of the poles and output voltages are different. Table 4.2 includes three sections for comparison, namely the generator specifications, system weight and components costs. The generator specifications present details of the DFIGs designs such as bore diameter, axial length, airgap diameter, slot dimensions, etc. As shown, the bore diameter increases when the speed decreases. This is expected since the rated torque must increase with a drop in rated speed. This is achieved by increasing the airgap diameter, since $T \sim D^2 L$. The system weight shows the mass of the different parts of the machine such as the stator, rotor, and gearbox. The copper mass of the winding reduces when voltage increases and speed decreases. The gearbox weight increases when speed reduces and the insulation expense will increase with voltage. The last part of table 4.2 shows the cost of the wind generator and efficiency of the machines. The active material cost increases along with the active material mass when the speed decreases and voltage increases. In table 4.2, the initial cost showed wind turbine installation, winding, and cables expense generally. The cables in the low-voltage (LV) system contain simple insulation materials but they are more complicated for medium voltage (MV) systems. These cables have a coated copper and a variety of insulations.

Moreover, the terminations of these MV cables are more difficult than that of LV cables and are usually performed by higher skilled labour. However, the total cost impact on installation and maintenance of these cables is minor and covered in the initial costs. Moreover, the annual energy was calculated based on the gearbox's maintenance, generator insulation failure and an average wind profile.

Table 4.4 The comparison of analytical design features for a 736 kW generator.

	Generator System					
Machine name	A	B	C	D	E	F
Synchronous speed n [rpm]	1800 (4 poles)			900 (8 poles)		
Voltage (on stator)[V]	690	2000	4000	690	2000	4000
Airgap diameter [m]	0.0015	0.0015	0.0015	0.0025	0.0025	0.0025
Bore diameter [m]	0.581	0.565	0.472	0.663	0.839	0.795
Outer diameter [m]	0.894	0.856	0.75	0.911	1.07	1.02
Inner diameter [m]	0.344	0.337	0.261	0.5	0.65	0.62
Axial length [m]	0.285	0.34	0.361	0.396	0. 310	0.37
Stator slot height [m]	0.0529	0.0684	0.075	0.0529	0.0629	0.693
Stator slot width [m]	0.02	0.01	0.01	0.02	0.01	0.01
Stator tooth width [m]	0.0307	0.0147	0.011	0.0089	0.0083	0.0073
Rotor slot height [m]	0.0404	0.0379	0.0417	0.0393	0.0390	0.0392
Rotor slot width [m]	0.021	0.105	0.105	0.021	0.105	0.105
Rotor tooth width [m]	0.0547	0.019	0.014	0.0221	0.0113	0.0102
	System Weight					
Stator's Iron [kg]	808	695	713	585	869.5	781
Rotor's Iron [kg]	404	327	294	255	426	545
Stator's Copper [kg]	1.2	0.37	0.271	0.991	0.393	0.221
Rotor's Copper [kg]	4.2	1.87	1.66	3.44	1.52	1.24
Single-stage gearbox [kg]	402	403.2	401.2	810.5	812.65	812.65
Total weight [kg]	1619	1427	1410	1655	2110	2140
	Component Cost					
Generator active material [$]	6840	6230	6550	7300	7520	7810
Initial [$]	18310	15960	12690	25530	20120	17610
Annual Energy cost [$]	37570	37710	33640	36530	39770	38630
Total cost [$]	62720	59900	52880	69360	67410	64050
Efficiency %	93.1	94.1	95.2	93.8	95.6	93.6
Power factor	0.91	0.9	0.912	0.862	0.9	0.9

4.5.2 Comparison

Figure 4.3 shows the characteristics of the stator current versus the shaft torque. The mechanical part of the generator involves the shaft torque. As seen in figure 4.3, the torque is proportional to the stator current. Conversely, all machines have similar output power and it would be more efficient to generate electricity at maximum torque in a wider range of stator current in order to control output power. It is indicated that the

wider graph of the stator current has better capabilities in terms of the generator's load [135]. Low-speed machines are heavier. As a result, these machines require more torque to produce the same electrical power. Figure 4.4 shows the efficiency versus the shaft torque and a similar trend is observed for increasing torque.

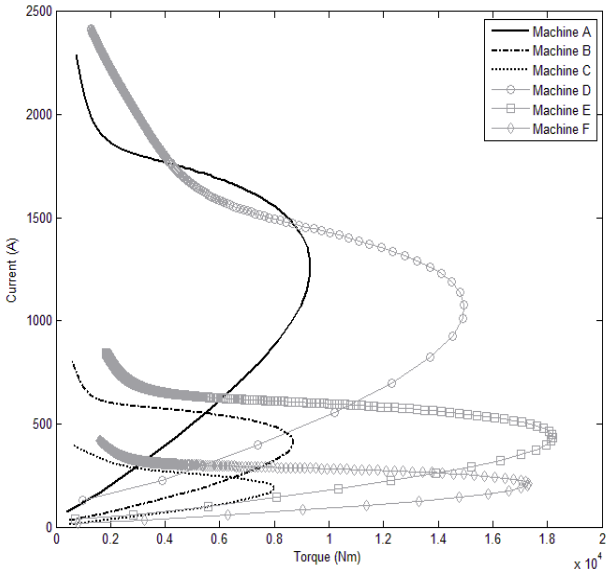

Fig. 4.3 The stator current versus torque for machines A, B, C, D, E, and F.

The torque versus slip characteristics of machines A, B, C, D, E, and F in figure 4.5 show that as the pole number increases, the peak torque increases. The height of the torque versus the slip is dependent on the leakage reactance, while the width depends on the stator and rotor resistance. The magnetization current can reduce the short-circuit current and hence prevent the insulation failure in the generator. Figure 4.6 shows that the magnetization inductance is higher for high-speed machines than for low-speed machines. The magnetization inductance range is usually between 3.5 to 5 p.u. for an IM with a rating of 700 kW power for the wound rotor [27]. Low-speed machines are in this range and high-speed machines lie slightly out of the limitations. As shown in figure 4.7, the rotor and stator resistance in the low-speed machines is more than that of the high-speed machines. This implies that low-speed machines have higher copper loss. Moreover, considering figure 4.5 again, the maximum torque reduces by decreasing the rotor resistance for each speed.

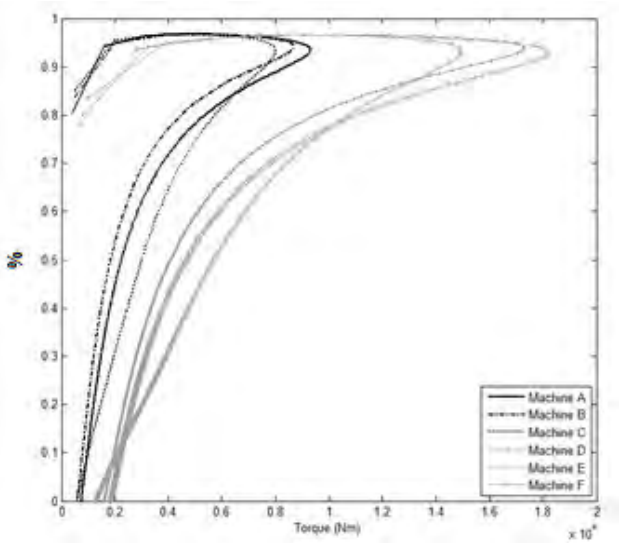

Fig. 4.4 The efficiency versus torque for machines A, B, C, D, E, and F.

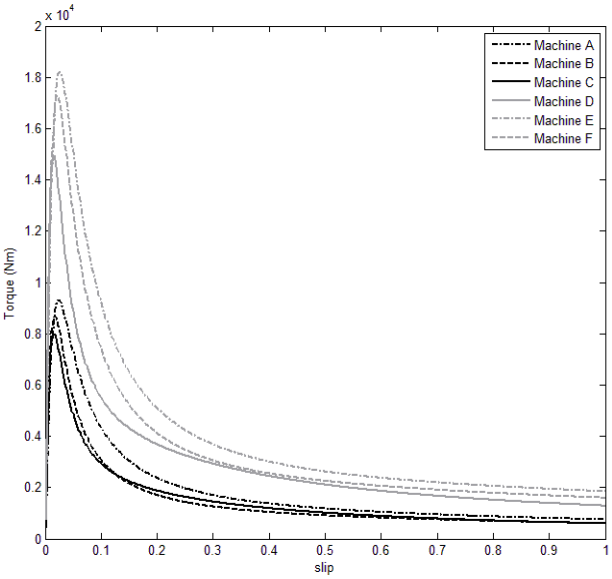

Fig. 4.5 The torque versus slip for machines A, B, C, D, E, and F.

4.6 Conclusion

Variations in the designs of a 736 kW induction machine are presented in this chapter. Several aspects are compared and discussed for each design configuration. The MV system achieves a significant capital cost advantage over the traditional LV system. In particular, a substantial reduction in the cost of cables and transformers is observed for MV systems compared to LV systems. The cost of converters also decreases dramatically for MV machines. The perceived technical risk in the development of MV converter systems is a concern for turbine manufacturers and operators. It is important to note that many of the historic technical problems have been overcome in recent years by technological advances. The weight of a gearbox increases dramatically with an increased

power rating of the turbine. In fact, the gearbox weight will scale approximately with the cube of the radius, as does the weight of the rotor. Since planetary gearboxes are lighter than parallel-shaft boxes, there is a weight advantage to be gained by using them.

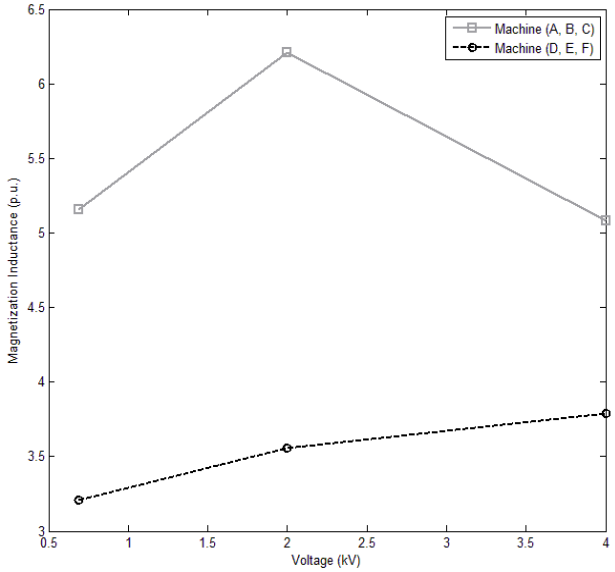

Fig. 4.6 The magnetization inductance versus voltage.

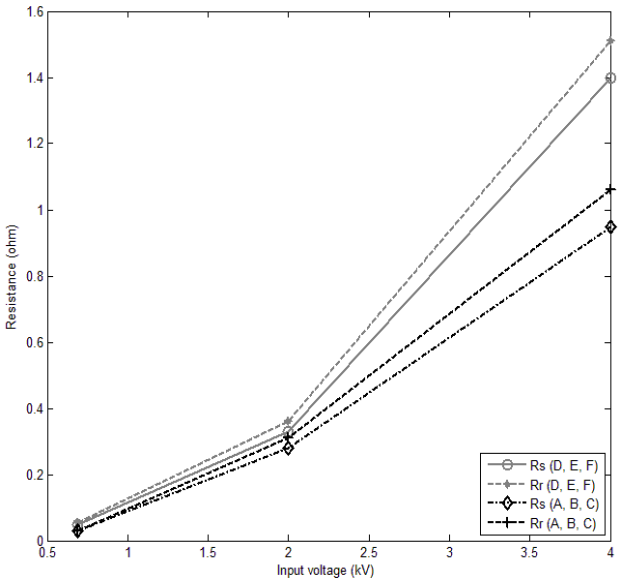

Fig. 4.7 The stator and the rotor resistance versus voltage.

On the other hand, due to their greater complexity, they also cost more than would be indicated by their reduced weight. Machines C and E are the most efficient of the high-speed and low-speed machines, respectively. The results show that the quality of the power generated by low-speed machines is better than that generated by high speed machines. As a conclusion, it would be better to compromise between the quality, efficiency and cost in different circumstances.

5. Wind Power Integration Issues

The main goal of the power system is to supply the network's energy demand. In order to increase the penetration of wind energy in the power system, due to green energy obligations, it must adjust with power system conditions. Thus, the wind energy must satisfy the system's conditions before joining the network. The wind power fluctuates naturally and its fluctuation will migrate to the power system with wind energy integration. This chapter presents the wind energy integration issues with the introduction of aggregated modelling to investigate these issues. The advantages and disadvantages of the aggregation's models are also presented. Finally, a single machine equivalent is discussed.

5.1 Introduction

When nuclear energy was introduced to the market, integration posed a challenge due to the inflexibility of nuclear energy. Hence, the flexibility of the system must be great enough to add the nuclear source to the grid. Also, wind power is fairly new to the system and more recently governments have made the decision to increase renewable energy shares in the market, particularly wind energy, due to its advantages. The increasing wind energy shares are evident with the current technology and do not require a major redesign of the existing system. However, it is essential to predict the behaviour of wind farms while integrating to the power system [36], [129], [130].

5.2 The Wind Farm in the Power System

The equation 5.1 indicates the voltages and the currents in a power system,

$$v(t) = V_M \cos(\omega t)$$
$$i(t) = I_M \cos(\omega t - \theta) \quad 5.1$$

where,

$v(t)$: Voltage;

V_M: Maximum voltage;

$\omega = 2\pi f$;

f : Frequency;

$i(t)$: Current;

I_M: Maximum current;

θ: Phase shift between voltage and current.

The power can be calculated by the voltages and the currents as follows:

$$p(t) = v(t)i(t) = V_M \cos(\omega t)\, I_M \cos(\omega t - \theta) \qquad 5.2$$
$$= P[1 + \cos(2\omega t)] + Q\ sim\ (2\omega t)$$

where, P and Q represent active and reactive power, respectively. Essentially, the voltage and the current waves must have a constant amplitude and $120°$ phase shift between them to transfer 3-phase symmetric power to the grid. The impedance in all transmission lines, cables and transformers in the feeding grid is represented by Z in figure 5.1. The figure also indicates a local load at the point of connection of the wind farm [149].

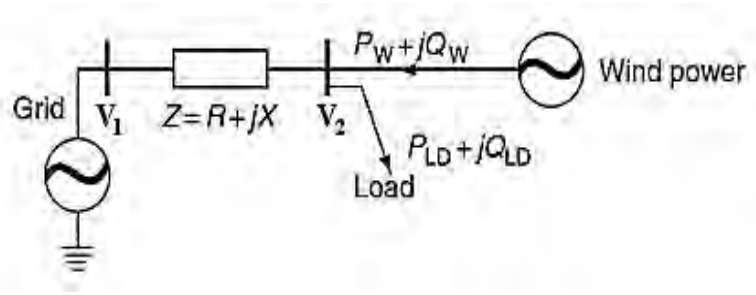

Fig. 5.1 The grid connection of wind power.

V_1: RMS value of the voltage on the grid side;

V_2: RMS value of the voltage on the load side;

P_w: Wind power active power;

Q_w: Wind power reactive power;

P_{LD}: Local load active power;

Q_{LD}: Local load reactive power.

If there is a short-circuit failure at the wind farm connection point, then the short-circuit power (P_{sc}) can be calculated through equations 5.3 and 5.4. The short-circuit increases the current in the impedance Z, while P_{sc} flows towards short-circuit point. It is important to understand how the grid reacts.

$$V_1 - V_2 = \sqrt{3}\, Z.I \qquad 5.3$$

$$P_{sc} = \frac{{V_1}^2}{Z^*} \qquad 5.4$$

Under the normal conditions, the amount of current in impedance Z depends on the wind energy generation due to its voltage (V_2) fluctuation. It must be recognized that there is no space for wind energy in the weak system (with large impedance) as much as there is for the stronger system (with small impedance) [150], [151]. As seen in equation 5.2, the voltage V_2 in figure 5.1 can be calculated as:

$$V_2 = \left\{ -\frac{2a_1 - {V_1}^2}{2} + \left[\left(\frac{2a_1 - {V_1}^2}{3} \right) - ({a_1}^2 + {a_2}^2) \right]^{\frac{1}{2}} \right\}^{\frac{1}{2}} \quad 5.5$$

where,

a_1: $-R(P_W - P_{LD}) - X(Q_W - Q_{LD})$,

a_2: $-X(P_W - P_{LD}) + R(Q_W - Q_{LD})$.

Equation 5.5 shows that the reactive power generation in the wind farm, Q_W, has an impact on the voltage V_2. The local load and the feeding grid impedance are important parameters in this incident.

5.3 Integration to the Power System

Figure 5.2 illustrates the power from the network (P_G), industries and residential demands (P_D), and a wind power station that delivers power, P_W. The impedances ($Z_1 - Z_3$) represent the impedances in the transmission lines and transformers between the different places in figure 5.2.

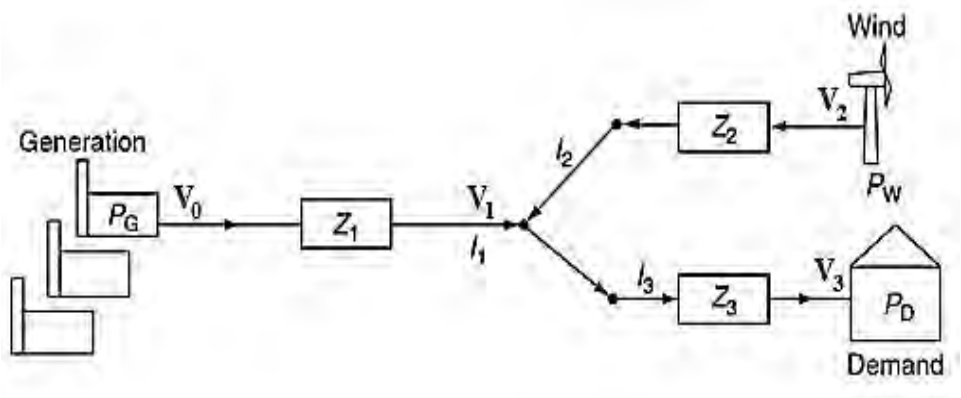

Fig. 5.2 Illustrative power system.

It is clear that the energy cannot disappear in the system. Therefore,

$$P_G = P_D + P_L - P_W \quad 5.6$$

where,

P_G: The power production in the grid side;

P_D: The power consumption in the residential load;

P_L: The electrical losses in the impedances;

P_W: The wind energy.

The energy demands must be supplied by the power system. It is noted that the grid power, wind energy and other power sources must be balanced against the energy demands. Furthermore, the voltage level and the reactive power must be considered in the transmission system. Hence, it is essential to investigate the dynamic behaviour of wind farms in case of system faults in more detail.

5.4 The Effect of Wind Turbines on the Grid

Wind farms are located in remote areas and they connect to the grid through high-voltage (HV) or medium-voltage (MV) distribution systems. Usually, the wind turbines employ transformers and they may connect to the HV system. It is, however, often more efficient sometimes to connect them directly by MV transmission lines to more nearby loads. As mentioned, wind farms influence the steady-state voltage and reactive power consumption of the network. The integrated wind power must respect the power system's rules which are as follows:

- *Steady-state voltage*

The power system is designed to keep the voltage level as steady as possible. The voltage variations of the system must be within the standard limits whenever the wind turbines are directly connected to the MV system. These limits are set by the official wind farm planning considerations [126], [152].

- *Reactive power consumption*

The reactive power is an important factor in the power system. There is a demand for reactive power from the reactive component operating in the network. The wind farms also consume reactive power for their transformers and the transmit lines when they are feeding active power to the grid. Reactive power consumption can decrease the power factor at the conventional power stations [127]. It will increase in the classic constant speed wind turbines (SCIG), as well as variable speed wind turbines (DFIG) with thyristor-based converters. However, the wind turbines with IGBT-based converters (DFIG) will not consume reactive power [3], [153], [154].

5.5 The Network Impact on the Wind Turbine

Weak grids may have an effect on aspects of the wind turbines such as performance, safety, etc. [127], [152], [155]. These impacts are as follows:

- *Power performance*

The wind turbine's power performance can be affected by outages, frequency, and voltage imbalance.

- *Safety*

The safety of the wind turbine would be compromised when it is connected to weak grids. For example, grid abnormalities in the voltage and the frequency may cause trip relay and overheating of the generator.

- *Structural lifetime*

The weak grid increases the mechanical stress on the wind turbine. Hence, the lifetime of the mechanical components will be reduced.

- *Reactive power consumption*

As stated above, wind farms trade the reactive power with the power system. This will affect the power system and wind farms. So, it will influence the power factor of the wind turbine.

5.6 Dynamic Performance of Wind Turbines

The regimen of energy generation has been changed by the WECS. Wind farms have different characteristics from large power plants. Wind farms can recover and return to being online within a few seconds following a disconnection due to mechanical failure. On the other hand, thermal power stations require hours to be able to resynchronize themselves to the network after a failure. One should also note that these types of stations may contribute for several seconds substantially in a short-circuit in order to ensure network protection and maintain voltage levels [156], [157]. Wherever wind energy dominates in the local network and conventional generation from large power stations is simultaneously reduced, significant voltage drops and frequency fluctuations are more likely if the short-circuit capacity is reduced. This leads to both a voltage instability and damage to the network protection systems. The understanding of the dynamic behaviour of the wind turbines is vital in network failures in order to find the new grid requirements and adjust the network regulation mechanism [1], [158].

5.7 Aggregated Modelling of Large Wind Farms

An aggregated model of a wind farm must consider each wind turbine individually, their mutual interactions, the internal transmission lines and the wind farm grid connection. It must also reduce the wind farm model and implement it in detailed models of the large power system. The covering of these two issues is the main objective of an aggregated model [18], [136]. An aggregated model is used to analyse the power system's stability. In this chapter, the focus is on the impact of a large wind farm on a large power system which implies that a single machine can represent a large wind farm [159].

5.7.1 Aggregated Modelling Issues

As previously noted, the mutual interaction between wind turbines within a large wind farm is considered by the aggregated model. The model is able to indicate the risk of combing the electricity produced by different wind turbines within the wind farm [1]. A grid disturbance from the external network may initiate the interaction problem within the wind farm. Thus, a group of wind turbines might be separated from the others. The potential of mutual interaction is higher amongst the wind turbines with converter-controlled generators. Also, the issue of the wind turbines equipped with induction generators and blade-angle control is cited [160], [161]. The aggregated model may assist in designing the internal network of the wind farm and estimation of its reactive compensation [162]. For large wind farms, analysing and investigating the control coordination between control systems of wind turbines is possible by the wind farm's aggregated models [163]. Aggregated models of large wind farms can also be used to evaluate relay settings during short-circuit faults or other disturbances in the internal network of a wind farm. Instead of a complete model of all wind turbines, the behaviour of the wind farm (at the point of common coupling to the grid) can be represented by an equivalent model derived from the aggregation of wind turbines into an equivalent wind turbine. A few aggregate wind farm models have been proposed in the literature, reducing computational effort and simulation time during transient stability analysis. In [136], a single-machine aggregate wind turbine model is developed for the entire wind power plant. References [161] and [164] propose an equivalent model with constant incoming wind speeds. An aggregate model is introduced in [165] which considers variable incoming wind speeds. A method has been presented to separate wind farms for parallel analysis in a super-computer and is given in [166]. The references are associated with two issues. On one hand, some research is based on simplified wind turbine models which lead to lower accuracy of dynamic results. On the other hand, some studies rely on simplified wind models which may decrease the simulation time but will increase the

application difficulty in order to create a new set of equivalent wind turbines and their variables whenever wind speed or wind direction change.

5.7.2 A Single Machine Equivalent

Whenever the power system falls into transient condition, the wind farm in the system also gets affected. The wind turbines evidently will respond coherently to the transient incident. It means the simulated behaviour of a wind turbine will be similar to the wind farm dynamic response, if they both operate at the rated operational point of the wind farm. The wind turbines with converters (DFIG and PMSG) would be at risk of a converter blocking at the rated operation due to the machine and the grid-side converter currents are being closest to their respective relay settings [136]. The arrangement of the control system of converters must be considered within the wind farm to decrease the risk of mutual interaction among the wind turbines. Therefore, the analysis of voltage stability for a wind farm can be done simply by a single machine equivalent [159], [167]. To show a single wind turbine model as a wind farm, the power capacity of the wind farm will be the power capacity of the equivalent machine and the power generated in the wind farm will be equal to the power produced in the equivalent machine [1], [159]. The reactive power of the equivalent machine is also zero at the connection point [168]. It is worth noting that the dynamic behaviour of speed and voltage are separated because the active and the reactive power controls are dependent on each other [136]. As known, the risk of mutual interaction for PMSG and DFIG may be neglected if the converter tuning is efficient [169].

5.8 Conclusion

In this chapter the basic integration issue is discussed. The main interest is shown on the short-circuit failure nearby the wind farm due to the wind farm behaviour being unknown which is explained and analysed with its effects on the grid. The aggregation is introduced as a tool to solve the issue and it helps reduce the complexity of the issue. A few aggregated models and their properties are presented. It is shown that they have difficulties in analysing the wind energy in the power system due to their constraints. A single machine is also considered to represent a wind farm in the system. However, it appears that prototyping a single machine equivalent is not feasible.

6. Dynamic Model of DFIG

As previously noted, a dimensional analysis technique is required when designing a micro-machine using a reference machine. This technique is justified by the objective of the scaling process, which is to achieve similar behaviour in both machines under transient conditions. Therefore, the scaling factors will essentially be defined by the parameters which generate the machine's behaviour. The d-q model of a DFIG under normal and short-circuit conditions is presented in this chapter in order to disclose the parameters in the steady and transient states.

6.1 Introduction

In general, illustrating the operation of 3-phase induction machines by an equivalent circuit or number of equations is known as modelling. An accurate dynamic model of a wind generator is required in order to do research on steady-state and transient characteristics of wind energy systems. In other words, this model assists in the discovery of effective parameters on the steady and transient behaviours of the machine under transient conditions. Therefore, the relationship between the identified parameters and the machine's equivalent circuit elements must be taken into account in the scaling process [3], [170].

6.2 Space Vectors in the Stator Reference Frame

An induction machine is illustrated in figure 6.1 to present the space vectors concept. For simplicity, the stator will be analysed and then the same concept will be used for the rotor. There are two assumptions necessary to explain this concept; firstly, each phase winding is assumed to have only one turn and secondly, all vectors indicated in bold letters and a superscript present a particular reference frame. The winding's axis is presented perpendicular to the plane in which the coil lies. The stator reference frames (stationary) are:

d_s: The direct axis aligned along the horizontal geometrical axes of the stator.

q_s: The quadrature axis aligned along the vertical geometrical axes of the stator.

The direct axis is physically referenced along the axis of the phase-A winding of the stator. Currents entering the coil ends marked A, B, C (in figure 6.1) have been defined as being positive. The currents are negative when entering ends A', B' and C' [170], [171]. Figure 6.2 illustrates that the phases are spatially displaced by 120°. If the currents entering the

coils are provided from the grid, with radian frequency ω, the currents can be indicated as follows:

$$i_{as}(t) = I_s \cos(\omega t) = I_s Re\{e^{j\omega t}\} \quad 6.1$$

$$i_{bs}(t) = I_s \cos\left(\omega t - \frac{2\pi}{3}\right) = I_s Re\left\{e^{\left(j\omega t - \frac{2\pi}{3}\right)}\right\} \quad 6.2$$

$$i_{cs}(t) = I_s \cos\left(\omega t + \frac{2\pi}{3}\right) = I_s Re\left\{e^{\left(j\omega t - \frac{2\pi}{3}\right)}\right\} \quad 6.3$$

where I_s illustrates the magnitude of stator current. Figure 6.3 presents the currents over two periods.

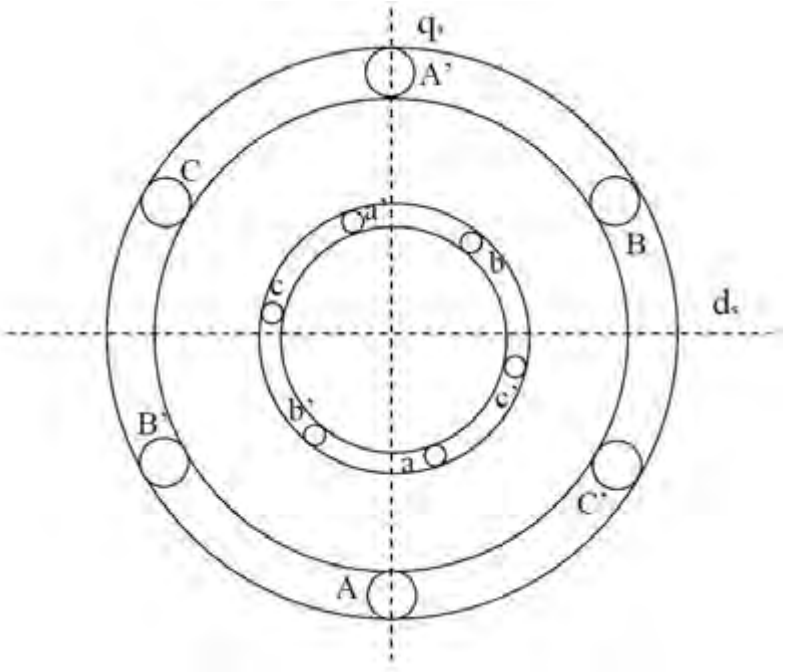

Fig. 6.1 The cross section of the stator and the rotor of 3 phase, 2-pole induction machine.

A magneto-motive force will be produced along the winding's axis when the current flows in a phase. These currents can be indicated as vectors in the winding's axis direction. The magnitude of the current vector is proportional to the instantaneous value of the current while the direction lies along the axis of the winding. These arrangements are known as space vectors [171]–[174]. Figure 6.4 presents the phase current space vectors (at $\omega t = 0$) with the resultant current space vector, which is gained by vector addition of the instantaneous phase current space vectors.

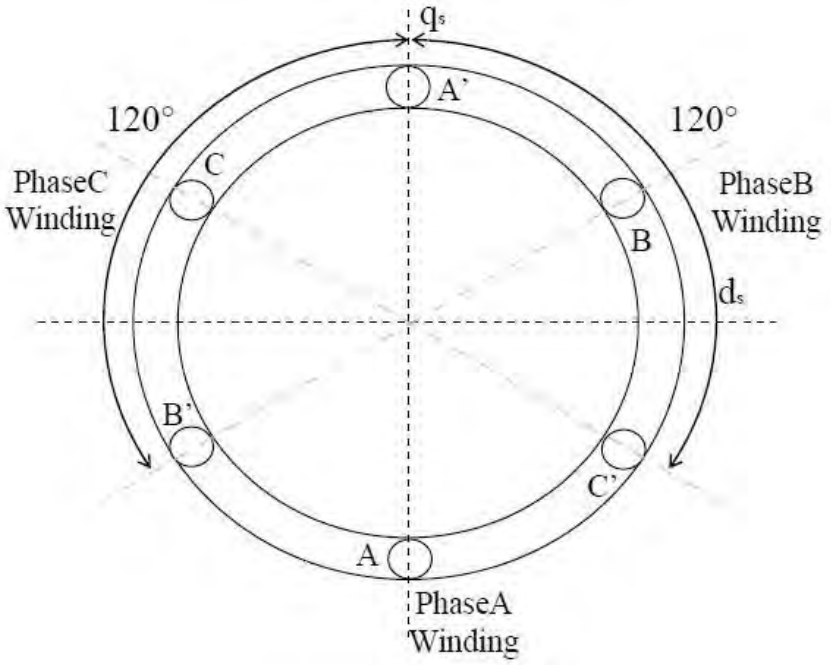

Fig. 6.2 The 3-phases located with 120° displacement.

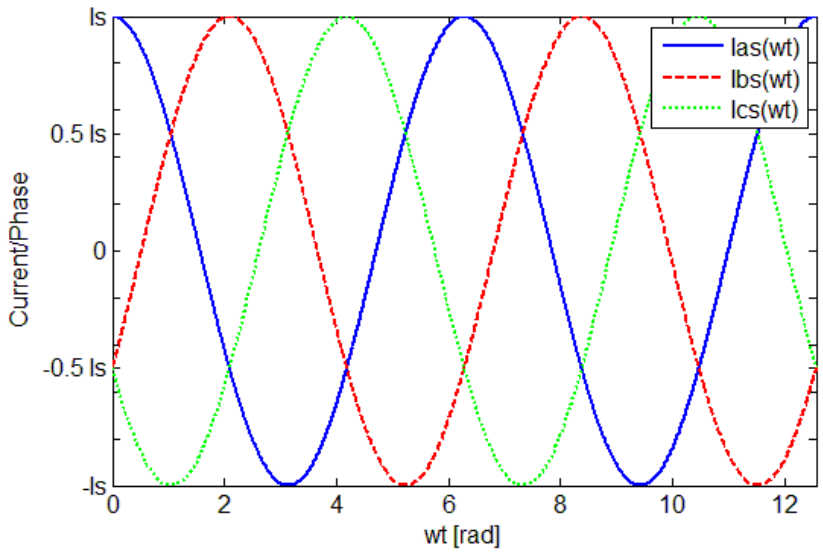

Fig. 6.3 The balanced 3-phase stator currents.

Each phase current space vector may also be presented in complex form and the final gained.

$$i_{as} = i_{as}e^{j0}, i_{bs} = i_{bs}e^{j\frac{2\pi}{3}}, i_{cs} = i_{cs}e^{j\frac{4\pi}{3}} \quad 6.4$$

$$i_s^s = i_{as} + i_{bs} + i_{cs} \quad 6.5$$

$$i_s^s = \frac{3}{2} I_s e^{j(\omega t)} \quad 6.6$$

At $\omega t = 0$;

$$i_{as}(0) = I_s;\ i_{bs}(0) = -\frac{1}{2}I_s; i_{cs}(0) = -\frac{1}{2}I_s \quad 6.7$$

$$i_s^S = I_s e^{j0} - \frac{1}{2}I_s e^{j\frac{2\pi}{3}} - \frac{1}{2}\ I_s e^{j\frac{4\pi}{3}} \quad 6.8$$

$$i_s^S = 1.5\ I_s e^{j0} \quad 6.9$$

which is presented in figure 6.4. At $= \frac{\pi}{3}$;

$$i_{as}\left(\frac{\pi}{3}\right) = \frac{1}{2}I_s;\ i_{bs}\left(\frac{\pi}{3}\right) = \frac{1}{2}I_s; i_{cs}\left(\frac{\pi}{3}\right) = -I_s \quad 6.10$$

$$i_s^S = \frac{1}{2}I_s e^{j0} + \frac{1}{2}I_s e^{j2\frac{\pi}{3}} - I_s e^{j4\frac{\pi}{3}} \quad 6.11$$

$$i_s^S = 1.5\ I_s e^{j\frac{\pi}{3}} \quad 6.12$$

which is indicated in figure 6.5. θ_s shows the angular position of the final stator current space vector. It is clear from figures 6.4 and 6.5 that the final vector current is $1.5\ \mathrm{I}_s$ and rotates with angular frequency ω.

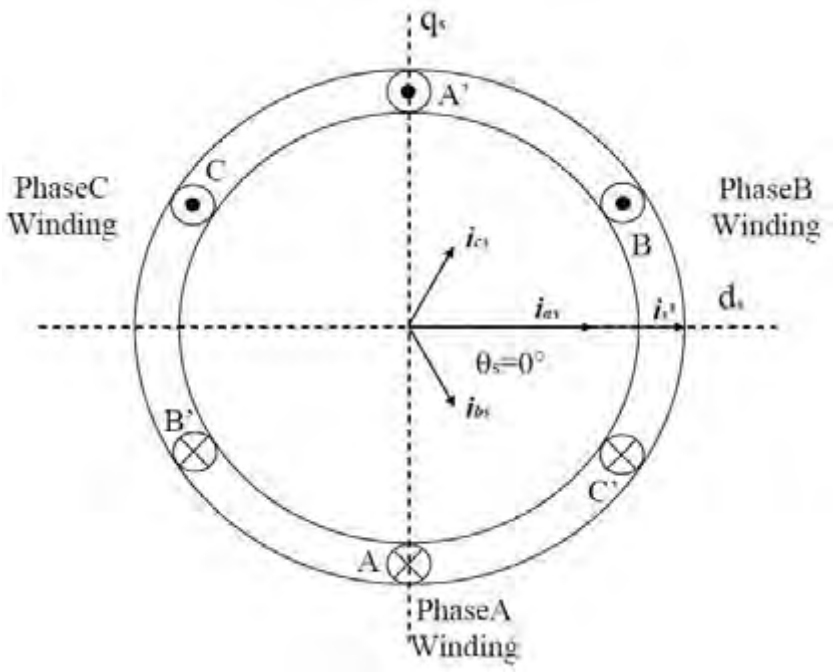

Fig. 6.4 The space vectors for the stator current at $\boldsymbol{\omega t = 0}$.

The implication of space vectors can also be distributed to all other parameters (i.e. voltage (v), flux linkage (ψ), mmf, etc.) [170], [171]. This means that a 3-phase induction machine is able to transform into an equivalent 2-phase induction machine through space vectors.

$$v_s^s = v_{as}e^{j0}\, v_{bs}e^{j2\frac{\pi}{3}} v_{cs}e^{j4\frac{\pi}{3}} \quad 6.13$$

$$\psi_s^s = \psi_{as}e^{j0}\, \psi_{bs}e^{j2\frac{\pi}{3}} \psi_{cs}e^{j4\frac{\pi}{3}} \quad 6.14$$

6.3 Transformations between the 3-phase and 2-phase Quantities

Thus far, the complex plane of the stator currents of induction machines have been presented. It is formed by the quadrature and direct axis. Using Euler's Identity $e^{j\omega t} = \cos(\omega t) + jsin(\omega t)$, the resultant stator current space vector may be decomposed into its quadrature and direct components. This is indicated below by substituting equation 6.4 into 6.5.

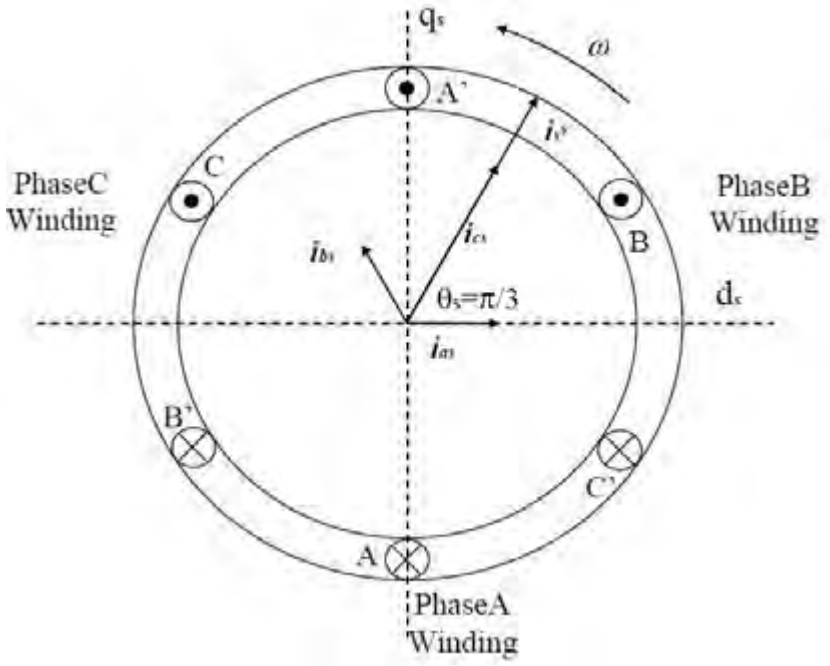

Fig. 6.5 The space vector for the stator current at $\boldsymbol{\omega t = \pi/3}$.

$$i_s^s = i_{as}e^{j0} + i_{bs}e^{j2\frac{\pi}{3}} + i_{cs}e^{j4\frac{\pi}{3}} \quad 6.15$$

$$i_s^s = i_{as}[\cos(0) + \mathrm{jsin}(0)] + i_{bs}\left[\cos\left(\frac{2\pi}{3}\right) + \mathrm{jsin}\left(\frac{2\pi}{3}\right)\right] + i_{cs}\left[\cos\left(\frac{4\pi}{3}\right) + \mathrm{jsin}\left(\frac{4\pi}{3}\right)\right] \quad 6.16$$

$$i_s^s = \left(i_{as} - \frac{1}{2}i_{bs} - \frac{1}{2}i_{cs}\right) + j\left(\frac{\sqrt{3}}{2}i_{bs} - \frac{\sqrt{3}}{2}i_{cs}\right) \quad 6.17$$

$$i_s^s = i_{ds} + ji_{qs} \quad 6.18$$

This may be indicated in matrix form as follows:

$$\begin{bmatrix} {i_{ds}}^s \\ {i_{qs}}^s \end{bmatrix} = \begin{bmatrix} 1 & -\frac{1}{2} & -\frac{1}{2} \\ 0 & \frac{\sqrt{3}}{2} & -\frac{\sqrt{3}}{2} \end{bmatrix} \begin{bmatrix} i_{as} \\ i_{bs} \\ i_{cs} \end{bmatrix} \quad 6.19$$

The derived expression is referred to as the Clarke Transform [171], [175]. The 3-phase quantities were shown in the stator reference frame by the resulting matrix. The inverse of the matrix above can easily be solved for and the expression in (6.20) is known as the Inverse Clarke Transform [175].

$$\begin{bmatrix} i_{as} \\ i_{bs} \\ i_{cs} \end{bmatrix} = \begin{bmatrix} \frac{2}{3} & 0 \\ -\frac{1}{3} & \frac{1}{\sqrt{3}} \\ -\frac{1}{3} & -\frac{1}{\sqrt{3}} \end{bmatrix} \begin{bmatrix} {i_{ds}}^s \\ {i_{qs}}^s \end{bmatrix} \quad 6.20$$

6.4 Transformations of Space Vectors between Different Reference Frames

i_s^s was referenced to a plane perpendicular to the rotor shaft and stationary to the stator. It can, however, also be referenced to other planes, with their orthogonal axis rotating at various speeds. For instance, the rotor reference frame will be explained as follows:

6.4.1 Rotor Reference Frame

The rotor current frequency is proportional to the slip, as shown:

$$\omega_{slip} = s\omega = \frac{d\theta_{slip}}{dt} \quad 6.21$$

$$s = \frac{\frac{\omega}{p_1} - \omega_r}{\frac{\omega}{p_1}} \quad 6.22$$

θ_{slip}: Slip angular position;

ω_{slip}: Slip angular frequency;

ω_r: Rotor angular frequency;

s: Slip;

p_1: Number of pole pairs;

The rotor reference frame is defined by having its real and imaginary axis aligned with the vertical and horizontal geometrical axis of the rotor. The real axis (direct axis, d_r), is physically referenced along the axis of the phase-A coil of the rotor. θ_0 is known as the angular position ($\theta_0 = \int \omega_0 \, dt$) and ω_0 is referred to as the angular speed at which the rotor reference frame rotates relative to the stator reference frame ($\omega_0 = p_1\omega_r$). The

currents in the rotor result in a final current space vector, which is indicated i_r (figure 6.6). θ_{slip} is the angular position of i_r relative to the rotor reference frame and may be calculated from the slip frequency (i.e. $\theta_{slip} = \int \omega_{slip}\, dt$). The resultant rotor current space vector relative to the rotor reference frame can be illustrated as follows:

$$i_r^r = 1.5\, I_r\, e^{j\theta_{slip}} \tag{6.23}$$

where I_r is magnitude of the rotor current. As noted, the angle change between the stator and rotor reference frame must be included (figure 6.6). Thus using Euler's Identity, $e^{j\omega t} = \cos(\omega t) + jsin(\omega t)$, the equivalent rectangular representation is:

$$i_r^s = i_r^r e^{j\theta_0} = \left(i_{dr}^r + \mathrm{j}i_{qr}^r\right)\left(\cos(\theta_0) + jsin(\theta_0)\right) = \left(i_{dr}^r \cos(\theta_0) - i_{qr}^r sin(\theta_0)\right) + j\left(i_{qr}^r \cos(\theta_0) + ji_{dr}^r sin(\theta_0)\right) \tag{6.24}$$

Representing the above in matrix form

$$\begin{bmatrix} i_{dr}^s \\ i_{qr}^s \end{bmatrix} = \begin{bmatrix} \cos(\theta_0) & -\sin(\theta_0) \\ \sin(\theta_0) & \cos(\theta_0) \end{bmatrix} \begin{bmatrix} i_{dr}^r \\ i_{qr}^r \end{bmatrix} \tag{6.25}$$

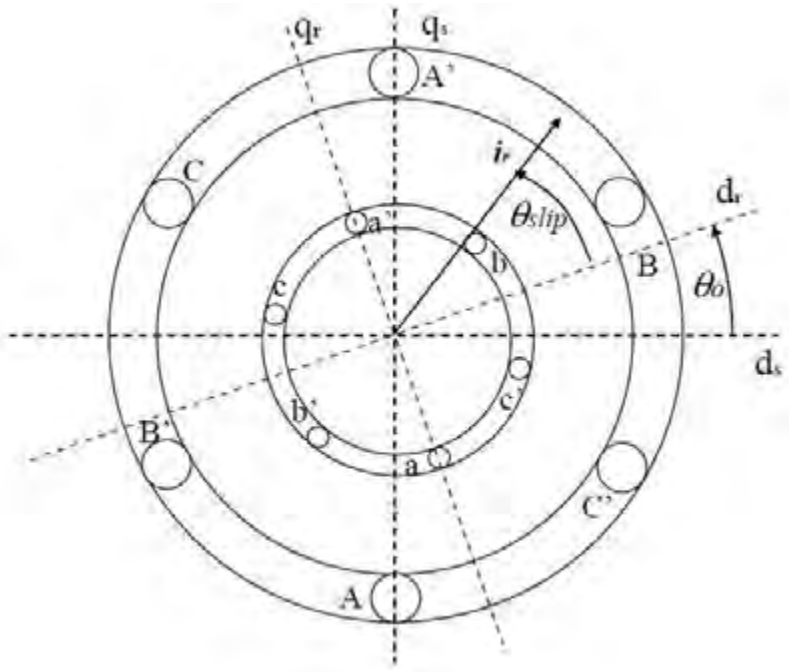

Fig. 6.6 The final rotor current space vector relative to the stationary and rotor reference frames.

The inverse of the above expression is as follows:

$$\begin{bmatrix} i_{dr}^r \\ i_{qr}^r \end{bmatrix} = \begin{bmatrix} \cos(\theta_0) & \sin(\theta_0) \\ -\sin(\theta_0) & \cos(\theta_0) \end{bmatrix} \begin{bmatrix} i_{dr}^s \\ i_{qr}^s \end{bmatrix} \tag{6.26}$$

6.4.2 Synchronous Reference Frame

Here, the purpose of transformation is to conveniently analyse behaviour of induction machines. It is essential to convert AC quantities to DC quantities due to alternating quantities being difficult to work with, and thus transformations to various reference frames are required to enable the conversion. The synchronous reference frame rotates at synchronous speed, ω, and the direct axis is referenced along the peak of the flux density in the airgap [170], [171]. The immediate angle shaped between the synchronous reference and the stationary reference frame is ωt (figure 6.7). The resultant stator current space vector seems to rotate at ω and stationary when perceived from the stationary reference frame and the synchronous reference respectively. It may then be decomposed into its two time invariant components; in the direction of its real and imaginary axes. The relationship between the synchronous and the stator reference frames are as follows (the resultant stator current space vector in the synchronous reference frame is i_s^e):

$$i_s^s = i_s^e e^{j\omega t} \tag{6.27}$$

$$i_s^e = i_s^s e^{-j\omega t} \tag{6.28}$$

Similarly,

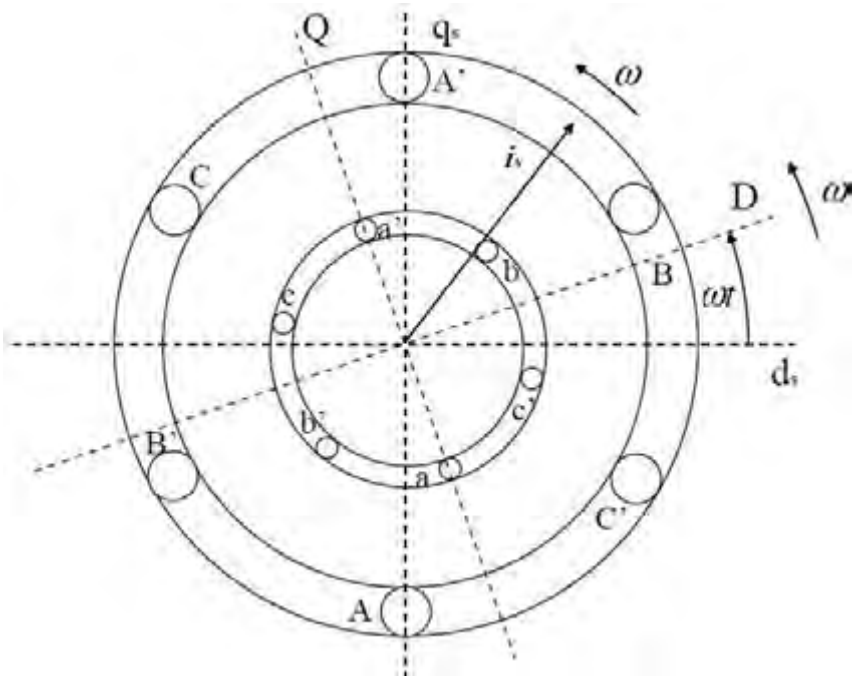

Fig. 6.7 Final stator current space vector relative to the stationary and synchronous reference frames.

$$v_s^s = v_s^e e^{j\omega t} \tag{6.29}$$

$$\psi_s^s = \psi_s^e e^{j\omega t} \tag{6.30}$$

The equivalent rectangular co-ordinates are as follows:

$$i_{ds}^s + j i_{qs}^s = \left(i_{Ds}^e + j i_{Qs}^e\right)\left(\cos(\omega t) + j sin(\omega t)\right) = \left(i_{Ds}^e \cos(\omega t) - i_{Qs}^e sin(\omega t)\right) + j\left(i_{Ds}^e \sin(\omega t) + j i_{Qs}^e cos(\omega t)\right) \tag{6.31}$$

$$i_{Ds}^e + j i_{Qs}^e = \left(i_{ds}^s + j i_{qs}^s\right)\left(\cos(-\omega t) + j sin(-\omega t)\right) = \left(i_{ds}^s \cos(\omega t) - i_{qs}^s sin(\omega t)\right) + j\left(-i_{ds}^s \sin(\omega t) + j i_{qs}^s cos(\omega t)\right) \tag{6.32}$$

Representing the above in matrix form:

$$\begin{bmatrix} i_{Ds}^e \\ i_{Qs}^e \end{bmatrix} = \begin{bmatrix} \cos(\omega t) & \sin(\omega t) \\ -\sin(\omega t) & \cos(\omega t) \end{bmatrix} \begin{bmatrix} {i_{ds}}^s \\ {i_{qs}}^s \end{bmatrix} \tag{6.33}$$

whereby the above expression is referred to as the Park Transform [167], [171]. The inverse is:

$$\begin{bmatrix} {i_{ds}}^s \\ {i_{qs}}^s \end{bmatrix} = \begin{bmatrix} \cos(\omega t) & -\sin(\omega t) \\ \sin(\omega t) & \cos(\omega t) \end{bmatrix} \begin{bmatrix} i_{Ds}^e \\ i_{Qs}^e \end{bmatrix} \tag{6.34}$$

which is known as the Inverse Park Transform. Thus the transformation between different reference frames integrates the theory of relativity. The solution policy of the problem determines the choice of the reference frame.

6.5 Dynamic Model of the Induction Machine in the Stationary Reference Frame

The windings may be presented as interconnected resistor-inductor circuit elements in induction machines. Figure 6.8 illustrates such a circuit while voltage, current and flux vectors are employed instead of time variant ac signals [65], [171], [176], [177].

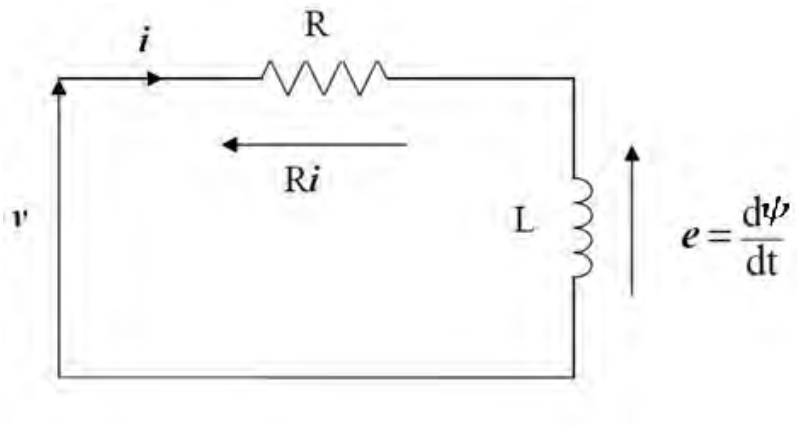

Fig. 6.8 Equivalent circuit representing the stator or rotor winding.

The stator winding voltage is represented as follows:

$$v_s^s = R_s i_s^s + \frac{d\psi_s^s}{dt} \tag{6.35}$$

The rotor winding voltage is represented as follows:

$$v_r^r = R_r i_r^r + \frac{d\psi_r^r}{dt} \tag{6.36}$$

The following substitutions refer the rotor equivalent equation to the stator,

$$v_r^r = v_r^s e^{-j\theta_0} \tag{6.37}$$

$$i_r^r = i_r^s e^{-j\theta_0} \tag{6.38}$$

$$\psi_r^r = \psi_r^s e^{-j\theta_0} \tag{6.39}$$

$$\frac{d\psi_r^r}{dt} = \frac{d\left(\psi_r^s e^{-j\theta_0}\right)}{dt} \tag{6.40}$$

Differentiation by parts, we get

$$\frac{d\psi_r^r}{dt} = \frac{d\psi_r^s}{dt} e^{-j\theta_0} + \frac{d(e^{-j\theta_0})}{dt}\psi_r^s = \frac{d\psi_r^s}{dt} e^{-j\theta_0} - j\frac{d\theta_0}{dt}\psi_r^s e^{-j\theta_0} \tag{6.41}$$

whereby,

$$\omega_0 = \frac{d\theta_0}{dt} \tag{6.42}$$

thus,

$$\frac{d\psi_r^r}{dt} = \frac{d\psi_r^s}{dt} e^{-j\theta_0} - j\omega_0\psi_r^s e^{-j\theta_0} = e^{-j\theta_0}\left(\frac{d\psi_r^s}{dt} - j\omega_0\psi_r^s\right) \tag{6.43}$$

Substituting equations 6.38, 6.39, 6.44 into equation 6.37, we get

$$v_r^s e^{-j\theta_0} = R_r i_r^s e^{-j\theta_0} + e^{-j\theta_0}\left(\frac{d\psi_r^s}{dt} - j\omega_0 \psi_r^s\right) \quad 6.44$$

dividing by $e^{-j\theta_0}$

$$v_r^s = R_r i_r^s + \frac{d\psi_r^s}{dt} - j\omega_0 \psi_r^s \quad 6.45$$

Interchanging $\frac{d}{dt}$ with p

$$v_s^s = R_s i_s^s + p\psi_s^s \quad 6.46$$

$$v_r^s = R_r i_r^s + \psi_r^s(p - j\omega_0) \quad 6.47$$

The flux vectors have to appear in terms of currents and inductances in order to express the above voltage equations in terms of the stator and the rotor current vector. Thus, the equations 6.46 and 6.47 will transfer as follows,

L_{ls} : Leakage stator inductance

L_{lr} : Leakage rotor inductance

L_m : Mutual inductance

whereby,

$$L_s = L_{ls} + L_m \quad 6.48$$

$$L_r = L_{lr} + L_m \quad 6.49$$

$$\psi_s^s = L_s i_s^s + L_m i_r^s \quad 6.50$$

$$\psi_r^s = L_m i_s^s + L_r i_r^s \quad 6.51$$

Substituting equations 6.50 and 6.51 into equations 6.46 and 6.47 respectively, the voltages are expressed as follows:

$$v_s^s = (R_s + pL_s)\, i_s^s + pL_m i_r^s \quad 6.52$$

$$v_r^s = (p - j\omega_0)L_m i_s^s + (R_r + (p - j\omega_0)L_r) i_r^s \quad 6.53$$

This can be re-written as follows:

$$v_{ds}^s = (R_s + pL_s) i_{ds}^s + pL_m i_{dr}^s \quad 6.54$$

$$v_{qs}^s = (R_s + pL_s) i_{qs}^s + pL_m i_{qr}^s \quad 6.55$$

$$v_{dr}^s = pL_m i_{ds}^s + \omega_0 L_m i_{qs}^s + (R_r + pL_r) i_{dr}^s + \omega_0 L_r i_{qr}^s \quad 6.56$$

$$v_{qr}^{s} = -\omega_0 L_m i_{ds}^{s} + pL_m i_{qs}^{s} - \omega_0 L_r i_{qr}^{s} + (R_r + pL_r) i_{dr}^{s} \qquad 6.57$$

This may be expressed in matrix form as follows:

$$\begin{bmatrix} {v_{ds}}^{s} \\ {v_{qs}}^{s} \\ {v_{dr}}^{s} \\ {v_{qr}}^{s} \end{bmatrix} = \begin{bmatrix} R_s + pL_s & 0 & pL_m & 0 \\ 0 & R_s + pL_s & 0 & pL_m \\ pL_m & \omega_0 L_m & R_r + pL_r & \omega_0 L_r \\ -\omega_0 L_m & pL_m & -\omega_0 L_r & R_r + pL_r \end{bmatrix} \begin{bmatrix} {i_{ds}}^{s} \\ {i_{qs}}^{s} \\ {i_{dr}}^{s} \\ {i_{qr}}^{s} \end{bmatrix} \qquad 6.58$$

The two equivalent circuits below represent the d-axis and the q-axis of the equations above.

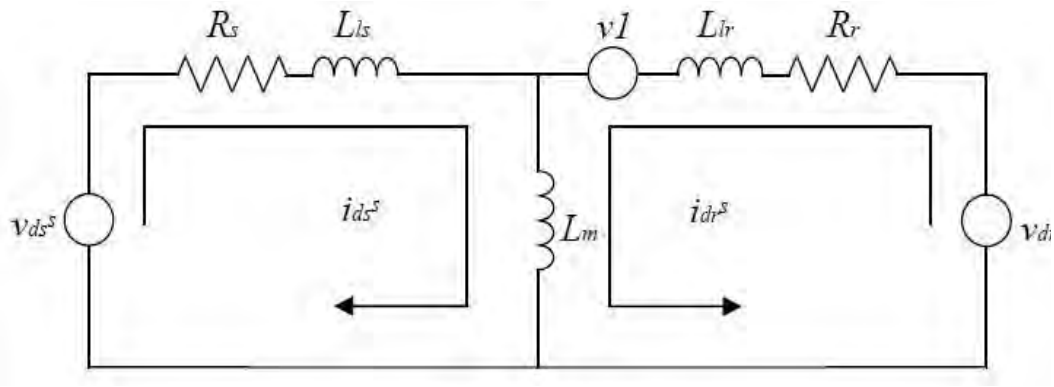

Fig. 6.9 Dynamic equivalent circuit of the d-axis in the stationary reference frame.

where,

$$v_1 = -\omega_0 (L_r i_{qr}^{s} + L_m i_{qs}^{s}) \qquad 6.59$$

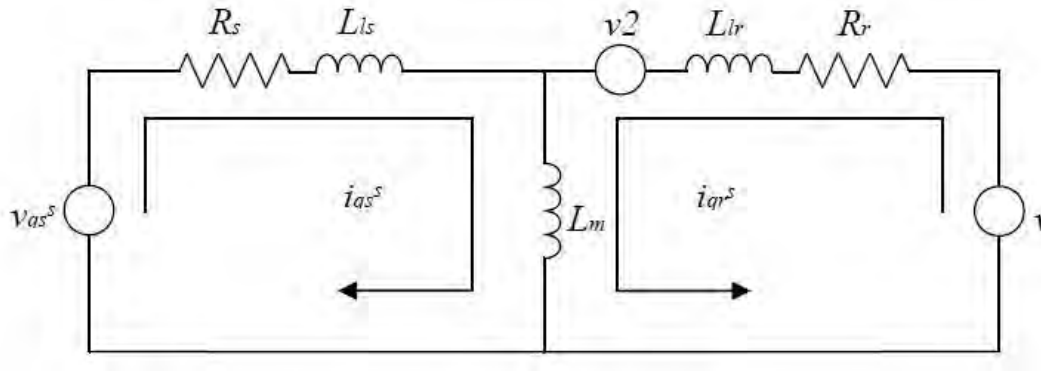

Fig. 6.10 Dynamic equivalent circuit of the q-axis in the stationary reference frame.

where,

$$v_2 = -\omega_0 (L_r i_{dr}^{s} + L_m i_{ds}^{s}) \qquad 6.60$$

6.6 Dynamic Model of the Induction Machine in the Synchronous Reference Frame

So far, the equivalent circuit and the modelling equations of the induction machine in the stationary reference frame have been given. Using equations 6.27, 6.29 and 6.30 (i.e. mapping v_s^s, i_s^s, ψ_s^s from the stationary reference frame to the synchronous reference frame), substituting into equations 6.46 and 6.47[65], [170], [171], [176].

$$v_s^e e^{j\omega t} = R_s i_s^e e^{j\omega t} + p\psi_s^e e^{j\omega t} \tag{6.61}$$

$$v_r^e e^{j\omega t} = R_r i_r^e e^{j\omega t} + \psi_r^e e^{j\omega t}(p - j\omega_0) \tag{6.62}$$

Substituting p with $\frac{d}{dt}$ and simplifying the stator equation,

$$v_s^e e^{j\omega t} = R_s i_s^e e^{j\omega t} + \frac{d(\psi_s^e e^{j\omega t})}{dt}$$

$$v_s^e e^{j\omega t} = R_s i_s^e e^{j\omega t} + \frac{d(\psi_s^e)}{dt} e^{j\omega t} + \frac{d(e^{j\omega t})}{dt}\psi_s^e \tag{6.63}$$

$$v_s^e e^{j\omega t} = R_s i_s^e e^{j\omega t} + \frac{d(\psi_s^e)}{dt} e^{j\omega t} + j\omega\psi_s^e e^{j\omega t}$$

$$\therefore v_s^e = R_s i_s^e + (p + j\omega)\psi_s^e$$

Simplifying the rotor equation,

$$v_r^e e^{j\omega t} = R_r i_r^e e^{j\omega t} + \frac{d(\psi_r^e e^{j\omega t})}{dt} - j\omega_0\psi_r^e e^{j\omega t}$$

$$v_r^e e^{j\omega t} = R_r i_r^e e^{j\omega t} + \frac{d(\psi_r^e)}{dt} e^{j\omega t} + \frac{d(e^{j\omega t})}{dt}\psi_r^e - j\omega_0\psi_r^e e^{j\omega t} \tag{6.64}$$

$$v_r^e e^{j\omega t} = R_r i_r^e e^{j\omega t} + \frac{d(\psi_r^e)}{dt} e^{j\omega t} + j\omega\psi_r^e e^{j\omega t} - j\omega_0\psi_r^e e^{j\omega t}$$

$$\therefore v_r^e = R_r i_r^e + (p + j\omega - j\omega_0)\psi_r^e$$

Since $\omega_{slip} = s\omega = \omega - \omega_0$,

$$v_r^e = R_r i_r^e + \left(p + j\omega_{slip}\right)\psi_r^e \tag{6.65}$$

Transforming equations 6.50 and 6.51 to the synchronous reference frame, the flux may be expressed as follows;

$$\psi_s^e = L_s i_s^e + L_m i_r^e \tag{6.66}$$

$$\psi_r^e = L_m i_s^e + L_r i_r^e \tag{6.67}$$

Substituting into equations 6.63 and 6.64 the following is attained,

$$v_s^e = [R_s + (p + j\omega)L_s]i_s^e + (p + j\omega)L_m i_r^e \quad 6.68$$

$$v_r^e = \left(p + j\omega_{slip}\right)L_m i_s^e + \left[R_r + \left(p + j\omega_{slip}\right)L_r\right] i_r^e \quad 6.69$$

and representing these in matrix form

$$\begin{bmatrix} {v_{Ds}}^e \\ {v_{Qs}}^e \\ {v_{Dr}}^e \\ {v_{Qr}}^e \end{bmatrix} = \begin{bmatrix} R_s + pL_s & -\omega L_s & pL_m & -\omega L_m \\ \omega L_s & R_s + pL_s & \omega L_m & pL_m \\ pL_m & -\omega_{slip}L_m & R_r + pL_r & -\omega_{slip}L_r \\ \omega_{slip}L_m & pL_m & \omega_{slip}L_r & R_r + pL_r \end{bmatrix} \begin{bmatrix} {i_{Ds}}^e \\ {i_{Qs}}^e \\ {i_{Dr}}^e \\ {i_{Qr}}^e \end{bmatrix} \quad 6.70$$

The two equivalent circuits, shown below represent the above matrix.

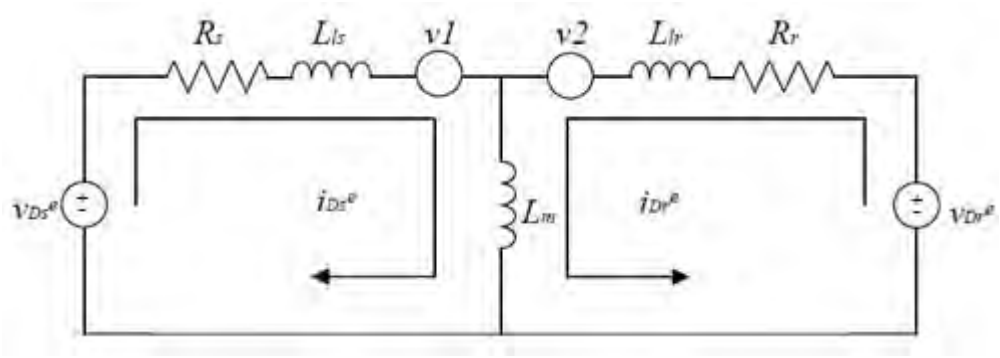

Fig. 6.11 Dynamic equivalent circuit of the D-axis in the synchronous reference frame.

where

$$v_1 = \omega(L_s i_{Qs}^e + L_m i_{Qr}^e) \quad 6.71$$

$$v_2 = \omega_{slip}(L_r i_{Qr}^e + L_m i_{Qs}^e) \quad 6.72$$

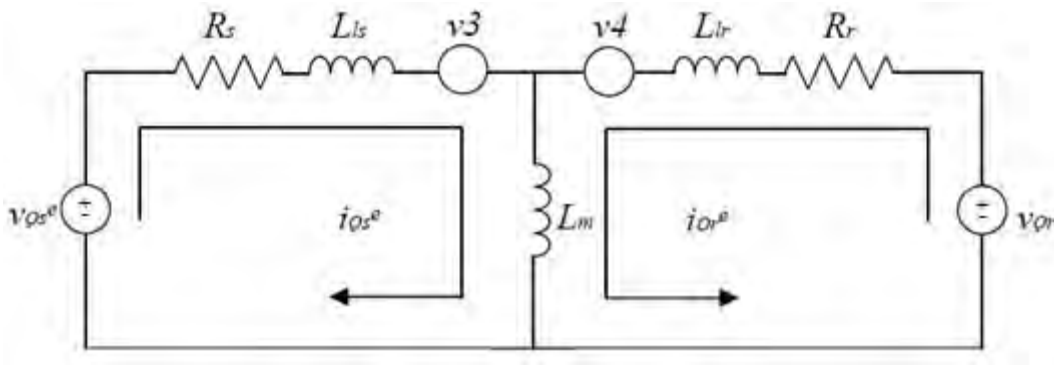

Fig. 6.12 Dynamic equivalent circuit of the Q-axis in the synchronous reference frame.

where

$$v_3 = -\omega(L_s i_{Ds}^e + L_m i_{Dr}^e) \quad 6.73$$

$$v_4 = -\omega_{slip}(L_r i_{Dr}^e + L_m i_{Ds}^e) \quad 6.74$$

6.7 Electromagnetic Torque Developed by the Induction Machine

The resultant stator and rotor current vectors may each be represented by a single fictitious coil (in figure 6.13) when the 3-phase winding transfers to a fictitious 2-phase winding in the stationary reference frame (figure 6.5). Figure 6.13 illustrates the stator magnetic flux by the dashed lines (Φ_{rs}). The radius of the rotor is represented by r while the angle between the stator and rotor current vectors is α. An electromagnetic force (F) is cause by a crash between the stator coil flux and the rotor coil flux. The torque applied on the rotor coil is caused by the force component, which lies perpendicular to the plane of the coil [170]. The force is expressed as follows:

$$F = F' \sin(\alpha) \quad 6.75$$

where,

$$F' = B.l.i.r \quad 6.76$$

B: Flux density of the magnetic field caused by the stator winding;

l : Length of the coil side;

The torque generated in both the coil sides is,

$$T' = 2F.r = 2F'.\sin(\alpha).r = 2l.r.B_{rs}i_r \sin(\alpha) \quad 6.77$$

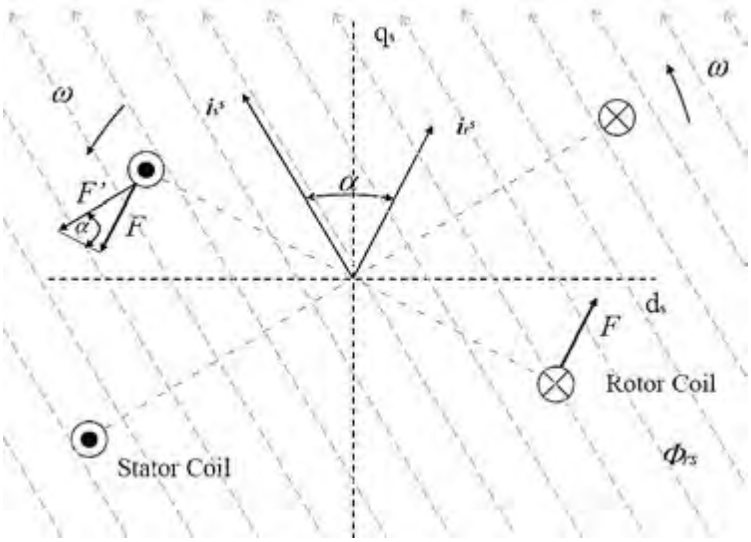

Fig. 6.13 Forces acting on imaginary stator and rotor coils [171].

Since the stator coil is a single turn, the flux density may be indicated in terms of the flux linkage,

$$B_{rs} = \frac{\Phi_{rs}}{A_r} = \frac{\psi_{rs}}{2l.r} \tag{6.78}$$

A_r: Area occupied by the rotor coil.

Substituting this back into the torque equation,

$$T' = \psi_{rs} i_r \sin(\alpha) \tag{6.79}$$

whereby the flux linkage may be represented in terms of the stator current as follows,

$$\psi_{rs} = L_m i_s \tag{6.80}$$

substituting into the torque equation,

$$T' = L_m i_s i_r \sin(\alpha) \tag{6.81}$$

$sin\ (\alpha)$ is expressed in terms of the currents rectangular complex components,

$$\sin(\alpha) = \sin(\theta_s - \theta_r) = \sin(\theta_s)\cos(\theta_r) - \cos(\theta_s)\sin(\theta_r) = \frac{i_{qs}^s}{i_s}\frac{i_{dr}^s}{i_r} - \frac{i_{ds}^s}{i_s}\frac{i_{qr}^s}{i_r} = \frac{1}{i_s i_r}\left(i_{qs}^s i_{dr}^s - i_{ds}^s i_{qr}^s\right) \tag{6.82}$$

The torque equation now appears in terms of the stator and rotor current complex components when substituting into equation 6.81.

$$T' = L_m\left(i_{qs}^s i_{dr}^s - i_{ds}^s i_{qr}^s\right) \tag{6.83}$$

As shown, the analysis done thus far has been for an induction machine with 2-poles. A machine with $2p_1$ number of poles turns p_1 times slower than the 2-poles machine. Therefore, the developed torque must be p_1 times to cover for the drop in speed (since Power (W) =Torque $(N.m)$ × Speed(rad/s)) for the same sized machine. The total apparent power gained by the imaginary 2-phase model, is $\frac{2}{3}$ times greater than the actual apparent power of the machine[170], [171]. This is proven below.

$$i_s = \frac{3}{2} I_{s,max} \tag{6.84}$$

$$v_s = \frac{3}{2} V_{s,max} \tag{6.85}$$

$$S'_s = v_s i_s = \frac{9}{4} I_{s,max} V_{s,max} \tag{6.86}$$

The actual apparent power of the machine is,

$$S'_s = 3\frac{I_{s,max}}{\sqrt{2}}\frac{V_{s,max}}{\sqrt{2}} \tag{6.87}$$

Thus, the actual power of the machine and the fictitious machine differs by a factor of $\frac{2}{3}$, which is compensated for by multiplying the torque by $\frac{3}{2}$. The resulting torque equation is as follows:

$$T = \frac{p}{3} L_m \left(i_{qs}^s i_{dr}^s - i_{ds}^s i_{qr}^s \right) \quad 6.88$$

Similarly the above may be proven for the transformation to the synchronous reference frame in which the following torque equation will emerge;

$$T = \frac{p}{3} L_m \left(i_{Qs}^e i_{Dr}^e - i_{Ds}^e i_{Qr}^e \right) \quad 6.89$$

6.8 d-q Modelling under Short-Circuit Condition

Here, the DFIG is considered to rotate at rated speed and its stator supplies an isolated passive load $(R_0 + j\omega L_0)$ with constant voltage v_s. In addition, a frequency converter with voltage phasor v_r is connected to the rotor. It is assumed that the speed, the rotor excitation voltage and the frequency remain unchanged. Vicatos used Laplace transformation on equations (6.70), (6.89) and $v_r^{e2} = v_{Qr}^{e2} + v_{Dr}^{e2}$ to deduce the machine's equations in Laplace mode. The d-q components of the stator and rotor equations are obtained by reversing the Laplace transformation. Then, the d-q components are retransformed to find the voltage as a function of time [178]. Ultimately, the stator voltage equations are simplified by eliminating the terms with p due to the stator and the rotor flux linkage remaining constant at the moment of short-circuit. The simplified voltage equation are as follow;

$$v_{Ds}{}^e = R_s i_{Ds}{}^e - \omega L_s i_{Qr}{}^e - \omega i_m i_{Qr}{}^e \quad 6.90$$

$$v_{Qs}{}^e = \omega L_s i_{Dr}{}^e + R_s i_{Qs}{}^e + \omega i_m i_{Dr}{}^e \quad 6.91$$

The d-q components of the rotor flux linkage are unchanged thus any stator current variation will cause a change in the rotor current at the instant the short-circuit occurs.

$$i_{Dr}{}^e = \frac{\psi_{Dr}{}^e}{L_r} - \frac{L_m}{L_r} i_{Ds}{}^e \quad 6.92$$

$$i_{Qr}{}^e = \frac{\psi_{Qr}{}^e}{L_r} - \frac{L_m}{L_r} i_{Qs}{}^e \quad 6.93$$

As a result, the stator voltage can also be expressed as follows:

$$v_{Ds}{}^e = R_s i_{Ds}{}^e - \omega i_{Qs}{}^e \left[L_s - \frac{L_m^2}{L_r} \right] - \omega L_m \frac{\psi_{Qr}{}^e}{L_r} \quad 6.94$$

$$v_{Qs}{}^e = R_s i_{Qs}{}^e + \omega i_{Ds}{}^e \left[L_s - \frac{L_m^2}{L_r} \right] + \omega L_m \frac{\psi_{Dr}{}^e}{L_r} \quad 6.95$$

Ultimately, the short-circuit current and voltage are determined and the stator short-circuit time constant can be calculated by $\frac{L_s}{R_s}\ (1 - \frac{L_m^2}{L_s\, L_r})$. The duration of the short-circuit is short due to the small stator time constant. In the end, the transient behavior of the DFIG is dependent on a few dominant parameters, which include time. The purpose of this section was to identify the dominant parameters of the machine's behavior, besides time. As considered, time is eliminated in equations (6.94) and (6.95), which enable identification of the other important parameters. The time constant is also important because their dynamic behaviors must be similar in equal time frame.

6.9 Conclusion

This chapter has reviewed the dynamic modelling of an induction machine. The dynamic modelling of the induction machine is critical in developing mathematical simulations. Also, it presents the dynamic model's parameter influence on the machine's behaviour. It would be useful to find a relationship between the mathematical model and the physical model. Ultimately, the machine will be scaled based on these parameters to have similarity in their behaviours in the next chapter.

7. Micro-Machines and Scaling

Thus far, the induction machine design has been discussed and the effective parameters of the DFIG in transient behaviour have been presented. The dimensional analysis technique is presented in this chapter in order to design a micro-machine which has the same behaviour as the reference machine. The identified parameters are used in order to find the scaling factor and ultimately design the scaled machine.

7.1 Introduction

As mentioned, there is a demand in the WECS to understand and predict issues such as integration, distribution, variability and power flow when a large scale of wind power is added to the power system. The first option is a mathematical simulation, which is ideal since the number of variables is large. However, the model simplification remains an interesting research area although finding the balance between computation time and result accuracy remains a challenge [1], [179]. The classic electric machine models have many simplifying assumptions which will reduce the accuracy [17], [180]. Therefore, an alternative technology is required to model the generator with its complexity and also reduce the simulation time. Micro-machines were introduced for this exact reason, to simulate complex operating phenomena associated with electric machines [65], [181]. Micro-machines are scaled prototypes of large utility-scale machinery. In the past, apprentice training, analytical design testing, tuning and regulation of current and new equipment were the reasons for the prototyping of micro-machines in the industry [7], [8]. In addition, the micro-machines were used for academic purposes such as confirmation of modes of specific systems and their specified parameters, simplification of the machine's structural parameters of specific elements, investigation of the power system stability and performing theoretical assumptions and approximations used in different analytical computations [9]–[11]. The micro-machines were attractive even though the ability of digital computers progressed and their results in sub-transient, transient and steady-state became more accurate. The advantage of micro-machines was that the exact operating condition could be simulated, which was a method to verify digitally computed results [4], [12].

7.2 Micro-Machine's History

Micro-machines are scaled models of industrial-sized generators, usually used as a component of a power system research bench. They were initially employed to be an

answer to the demand of empirical data amongst machine designers in the 1950s [182]. They were then used in the research of the transient behaviour of the power plant and the power system. Time constant regulators (TCRs) have been designed for micro-machines in order to improve their transient behaviour, which was their advantage against digital simulations [6], [183]. Their applications included the simulation of turbine generators, the creation of generator models, the determination of generated parameters as well as the validation of digital models of electric power systems. Furthermore, they have been used in the instruction (or teaching) of young engineers, the investigation of the generator stability and its control system [9], [13].

7.3 Micro-Machine's Applications in Wind Energy Conversion System

Micro-machines have the ability to validate the simulation of the integration of wind plants. Problems that may be solved by micro-machines include the inaccuracy in the mathematical modelling as well as the difficulty and cost involved in performing field tests on actual power systems [14]. The advantages of micro-machines in WECS include being easier to create a model, better model accuracy, the ability to carry out real-time analysis, and the ability to compare the results of real-time tests. The opportunities to use micro-machines in the WECS are as follows [181]:

- The large generators are integrated at transmission level to the power system, whilst the renewable energy sources (RESs) are usually integrated at the sub-transmission level. This means that the network is considered an ideal infinite bus at transmission level and the network would not be ideal at the sub-transmission level. Hence, the grid power quality may affect the RESs' behaviour in the system, and these influences may be neglected in current simulation packages. The realistic impact of the RESs on the system can be investigated by micro-machines.
- Current digital simulations depend on mathematical models of power system components. All of the usual influence in real components may not be involved in the simulation model due to the complexity of the components. The software manufacturers model the component slightly differently. This is why the designers are required to validate their simulation with various packages.
- There is a demand to validate the mathematical model experimentally, which is made possible by the micro-machines.
- As mentioned earlier, the electric machines are a complex phenomenon in the power system. This is worsened if a converter is added as a control system. The converters have their own dynamic behaviours which are not accurately modelled

in simulation packages. The micro-machines are able to be converted and tested under real conditions.

7.4 Dimensional Analysis Techniques

An acceptable scaled model of an alternator must be similar to the real one in a few parameters such as dynamic response and mechanical machine constants. In [7], a large synchronous generator is modelled by a micro-alternator with a low kVA rating. Equality in dynamic response is obtained by adding negative resistance on the rotor circuit. The micro-machine presented in [184] is relatively large for kVA power range and the result is not accurate enough. Equality in time constant and losses between the micro-machine and the real machine were considered in [10]. Berchten and his colleagues expressed a novel micro-machine model which adjusts eight of the transient and sub-transient characteristic time constants of a doubly-fed machine (DFM) [12]. In this model, several scaling factors link dimensions and also physical properties of the micro-machine to the real machine by considering equality in the dynamic response. The scaling factors and their definitions are shown in table 7.1.

Table 7.1 Scaling factors.

Scaling factors	Physical properties
k	For the machine diameter D, length L and slot width W_S
α	For the current density J
β	For the flux density B
γ	For the slot depth h_{SS}
Δ	For the airgap

The real machine dimension x^* multiplied to the scaling factor will drive the micro-machine dimension x. The scaling relationships of a micro-machine are represented by the equations in table 7.2.

$$x = (scaling\ factor) \times x^* \tag{7.1}$$

Table 7.2 Scaling formula.

Quantity	Relation	No.
Current Coverage [A]	$\frac{A}{A^*} = \alpha\gamma$	
kVA rating [VA]	$\frac{S}{S^*} = k^3\alpha\beta\gamma$	7.2
Voltage Rating [V]	$\frac{U}{U^*} = k^2\beta$	
Normalizing Impedance [ohm]	$\frac{Z_B}{Z_B{}^*} = \frac{k\beta}{\alpha\gamma}$	
Winding Resistance [p.u.]	$\frac{r}{r^*} = \frac{\alpha}{k\beta}$	7.3
Leakage Reactance [p.u.]	$\frac{x_\varrho}{x_\varrho{}^*} = \frac{\alpha\gamma^2}{k\beta}$	7.4
Magnetizing Reactance [p.u.]	$\frac{x_{ad}}{x_{ad}{}^*} = \frac{k\alpha\gamma}{\Delta\beta}$	7.5
Time Constant	$\frac{T}{T^*} = \gamma^2$	

These equations can be proven by substituting the scaling factor in the design equations from chapter 3. For instance, equation (7.2) can be proven as follows:

The apparent power is,

$$S = D^2 L_i k_{op} n_s \tag{7.6}$$

By substituting the specific electric loading and output coefficients in equation (7.6), S can be expressed as:

$$S = \frac{11\times10^{-3}}{\pi} D L_i n_s B_g K_w Q n_c I_s \tag{7.7}$$

The stator current is then converted to the current density and slot area, so S can be written as:

$$S = \frac{11\times10^{-3}}{\pi} D L_i n_s B_g K_w Z_c (J_s h_s b_{ss}) \tag{7.8}$$

The ratio of the output apparent power of the scaled-machine and that of the reference machine is expressed in (7.9). Here, the reference machine's number of conductors (Z_c) is also used for the scaled-machine (on the stator-side), so the scaling factors can be substituted as shown in (7.9).

$$\frac{S}{S^*} = k^3 \alpha \beta \gamma \tag{7.9}$$

The equations in table 7.2 can be derived in the same manner as equation (7.2). These equations build a dimensional relationship between a reference DFIG and micro-DFIG with the scaling factor for each design detail such as terminal voltage and current.

In chapter 6, equations (6.94-6.95) show the winding resistance, leakage and magnetizing reactances' impact on the transient behaviour of the machine under short-circuit conditions. The authors in [12] also derived the per-unit reactance and resistances of the micro-machine in the steady-state and transient which are close to the real DFIG to keep the dynamic response. Thus, equations (7.2-7.5) have been selected from table 7.2 in order for the micro-DFIG to prove that it performs like the real system. The reference machine will be scaled to an equivalent micro-DFIG when equations (7.2-7.5) are derived, based on ratio of the reference and micro DFIG parameters. Therefore, these ratios $\frac{r}{r^*} = 1$, $\frac{x_\varrho}{x_\varrho{}^*} = 1$, $\frac{x_{ad}}{x_{ad}{}^*} = 1$ will be assumed. Hence, the converted equations are given in (7.10-7.13):

$$k^3 \alpha \beta \gamma = 0.002 \tag{7.10}$$

$$\alpha = k\beta \tag{7.11}$$

$$\alpha\, \gamma^2 = k\, \beta \tag{7.12}$$

$$k\,\alpha\,\gamma = \Delta\,\beta \qquad 7.13$$

The scaling factors respectively are $\alpha = \frac{0.044}{k}$, $\beta = \frac{0.045}{k^2}$, $\gamma = 1$ and $\Delta = k^2$. These factors will define the characteristics of the scaled-DFIG. The geometric scaling factor k has to validate equation (7.14) for the micro-machine in the kVA range:

$$\pi D^* k \geq Q({b_{ss}}^*\gamma + {b_{st}}^* k\beta) \qquad 7.14$$

Equation (7.14) represents the fact that the circumference of the micro-machine ($\pi D^* k$) is equal to the sum of the slot width (${b_{ss}}^*\gamma$) and the thickness of rotor tooth (${b_{st}}^* k\beta$) multiplied by the number of slots if the airgap flux density remains unchanged ($\beta = 1$). Due to there being different scaling factors involved in scaling the slot width, the tooth width and diameter, this equation evaluates the feasibility of the scaled-DFIG.

Lipo suggested a simple scaling process of designing new machines by using the details of similar existing ones [25]. Alternative relations between two machines are proposed to simplify the design of the new machine in table7.3. It indicates that the parameters of the scaled-machine vary with length (k_l) and diameter (k_D) when the number of turns is held constant and when the number of turns is changed to keep the terminal voltage constant. Lipo also mentioned that the equality in the electrical time constant appeared to have a similar dynamic response between the two machines. As shown in table 7.3, the electrical time constant of the machine (transient and sub-transient) will increase by a factor ${k_D}^2$ when the resistance decreases and the inductance increases. The challenge of this method is the large deviation for scaling a machine from MWs rating to kWs. Hence, the model will not be accurate for a large difference between their ratings.

7.5 The Scaled-DFIG

As noted, two scaling models are introduced in this chapter. Berchten's scaling methodology is used in this thesis due to the inaccuracies in Lipo's policy when dealing with long distance scaling.

The design process usually begins with assumed values of the following initial design parameters: airgap flux density, stator and rotor current densities, etc. The scaling equations developed in this chapter are used in this thesis for the design of the scaled-DFIG. The minimum geometrical scaling factor (k) is determined as 0.25 by keeping the stator equivalent circuit parameters and magnetization reactance in per-unit system plus using equation (7.14).

Table 7.3 Lipo's scaling model parameters.

Parameter	Proportionality	Constant B, J and N	Constant B, J and V
Voltage [V]	$V \propto N.D.l$	$k_l.k_D$	1
Turns	N	1	$\frac{1}{k_l.k_D}$
Current [A]	$I \propto \frac{D^2}{N}$	${k_D}^2$	$k_l.{k_D}^3$
Power [W]	$V.I$	$k_l.{k_D}^3$	$k_l.{k_D}^3$
Resistance [Ω]	$R \propto \frac{N^2.l}{D^2}$	$\frac{k_l}{{k_D}^2}$	$\frac{1}{k_l.{k_D}^3}$
Losses [W]	$R.I^2$	$k_l.{k_D}^2$	$k_l.{k_D}^2$
Magnetic Inductance [Ω]	$L_m \propto \frac{N^2.A_m}{l_{mpath}}$	k_l	$\frac{1}{k_l.{k_D}^2}$
Leakage Inductance [Ω]	$L_l \propto \frac{N^2.A_l}{l_{lpath}}$	k_l	$\frac{1}{k_l.{k_D}^2}$
Magnetizing Current [A]	$I_m \propto \frac{V}{L_m}$	k_D	$k_l.{k_D}^2$
Magnetizing Field Energy	$\omega_m \propto L_m.{I_m}^2$	$k_l.{k_D}^2$	$k_l.{k_D}^2$
Leakage Field Energy	$\omega_l \propto L_l.{I_l}^2$	$k_l.{k_D}^4$	$k_l.{k_D}^4$
Electrical Time Constant	$\tau_e \propto \frac{L_m}{R}$	${k_D}^2$	${k_D}^2$
Breakdown Torque [N.m]	$T_{pk} \propto \frac{V^2}{L_l}$	$k_l.{k_D}^2$	$k_l.{k_D}^2$
Power Density [VA/m^3]	$\frac{VA}{volume}$	k_D	k_D
Temperature Rise [°C]	$\theta \propto \frac{I^2.R}{A_{surface}}$	k_D	k_D
Power Factor	$\frac{I}{I_m}$	k_D	k_D

The scaled-DFIG design is then continued by calculating the rating parameters such as output power, flux densities, current densities, stator diameter, airgap and slot dimension. In the next step, the rest of the machine's specifications such as rated voltage, equivalent circuit parameters and breakdown torque will be calculated by the equations in chapter 3. The current density and the airgap flux density were determined as 0.176A/m and 0.704T respectively, from the scaling process, which is clearly unacceptable. With consideration of the scaling procedure, the rated voltage is justified to have the desired current and stator slot fill factor (k_f). The number of turns on the rotor is also increased in order to improve the rotor tooth flux density and as a result the airgap flux density. As previously noted, the number of relevant stator or rotor slots for the scaled-DFIG is selected as half of the reference DFIG. This is to satisfy the slot width scaling factor (γ) as well as to strengthen the teeth of the micro-machine in order to resist against the rotational tension and stress. The airgap would be scaled to 0.1mm by Δ which is not feasible. Thus, it is assumed as 1.6mm, similar to the reference DFIG. Consequently, the scaled-DFIG cores, teeth and airgap flux densities are within the acceptable margin which verifies the result of analytical design. An air cooling system is considered for this machine. Table 7.4 illustrates the geometrical design details of the scaled-DFIG.

Table 7.4 Design parameter of the reference-DFIG details and the micro-DFIG.

Parameters	Reference	Micro-DFIG
kVA rating [VA]	2.5×10^6	5000
Efficiency [%]	95.7	73
Current [A]	1673.5	72.2
Voltage [V]	690	30
Torque [N.m]	13270	32.5
Number of slots Sta. /Rot.	60/48	30/24
Number of turns Sta. /Rot. per phase	80/160	80/320
Diameter [mm]	520	130
Length [mm]	520	130
Airgap [mm]	1.6	1.6
Stator slot width [mm]	13.6	6.8
Stator slot depth [mm]	68.8	8.7
Rotor slot width [mm]	15	7.5
Rotor slot depth [mm]	52	13.4
Airgap flux density [T]	0.75	0.63
Stator core flux density [T]	1.5	1.6
Stator teeth flux density [T]	1.55	1.32
Rotor core flux density [T]	1.87	1.63
Rotor teeth flux density [T]	2.1	1.77
Stator current density [A/mm^2]	6.5	6.5
Rotor current density [A/mm^2]	8	10

Maxwell 2D and 3D are used to verify the micro-DFIG and table 7.5 also indicates the equivalent circuit parameters.

Table 7.5 The equivalent circuit parameters for the reference-DFIG and the micro-DFIG.

Parameters	Reference	Micro-DFIG
Stator Resistance (R_s) [p.u.]	0.018	0.018
Stator Leakage Reactance (L_s)[p.u.]	0.346	0.349
Stator Time Constant [s]	0.0512	0.0493
Rotor Resistance (R_r)[p.u.]	0.022	0.133
Rotor Leakage Reactance (L_r)[p.u.]	0.4	0.526
Magnetization Reactance (X_m)[p.u.]	10.85	13. 5

The rated speed is assumed as 1750rpm and the rotor is excited through the converter. As expected, the efficiency is decreased by the output power. The per-unit resistance and per-unit reactance are approximately equal. The magnetization reactance is increased by 25 percent from the reference DFIG to the micro-DFIG. Their time constants are approximately 50ms. Due to the increase in number of turns and the use of narrower conductors, the rotor resistance and the rotor reactance are increased. The resultant flux lines and current densities are indicated in figure 7.1. As seen, the average current

densities are about 6.5A/mm^2 and 10A/mm^2 in the stator and the rotor respectively. Figure 7.2 shows the flux densities in the stator and the rotor cores. As shown above, the flux densities are distributed across the whole cross-section's area and they are not saturated. The average flux densities are $1.3Nm$ in the stator teeth and $1.8Nm$ in the rotor teeth. As mentioned in chapter 3, the stator outputs define the DFIG's behaviour. Figure 7.3 and 7.4 present the 3-phase stator current and the 3-phase stator voltage, respectively. These graphs are related to a state where the machine's speed is constant at 1750rpm while it is connected to the grid. The electrical time constant is about 45ms.

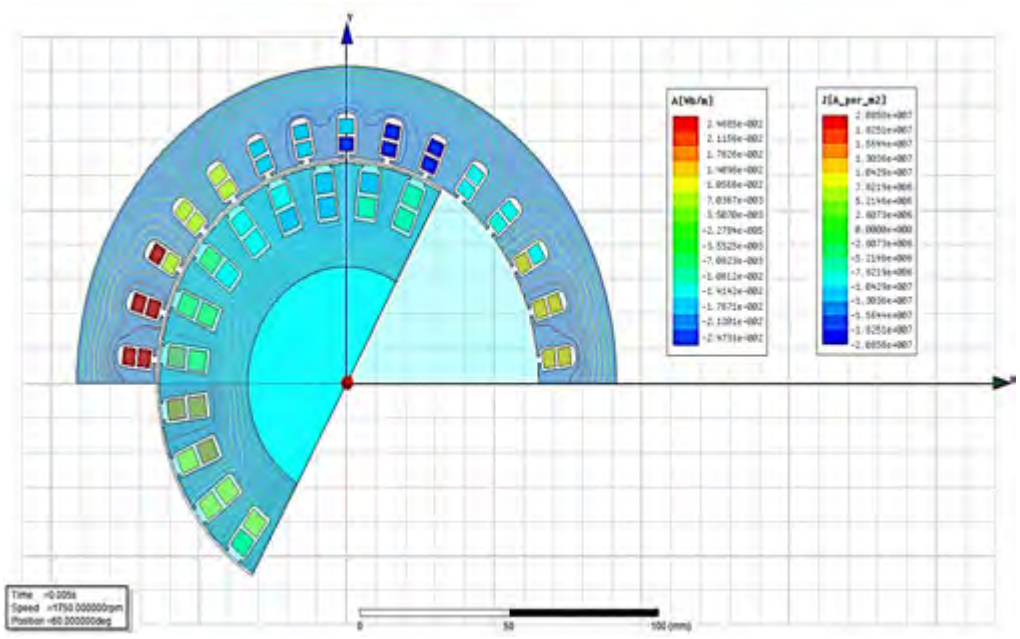

Fig. 7.1 The micro-DFIG flux lines and current densities in the stator and the rotor.

7.6 Conclusion

The micro-machines and their merits were reviewed in this chapter, along with several scaling processes. Here, Berchten's scaling model was preferred due to its accuracy in this case. The scaling equations in table 7.2 indicate the relationship between physical elements and equivalent circuit parameters. In fact, the circuit parameters will ultimately remain unchanged whenever the scaling factors (α, β and γ) are in unity. Therefore, the number of turns, slot width and voltage are adjusted after scaling to keep these factors in unity. Per-unit resistance and per-unit reactance are equal between the reference DFIG and scaled-DFIG. However, the magnetization reactances are different due to the airgap not having been scaled. The referenced DFIG is scaled to 5kW DFIG. The micro-DFIG has been verified by Maxwell 2D and 3D.

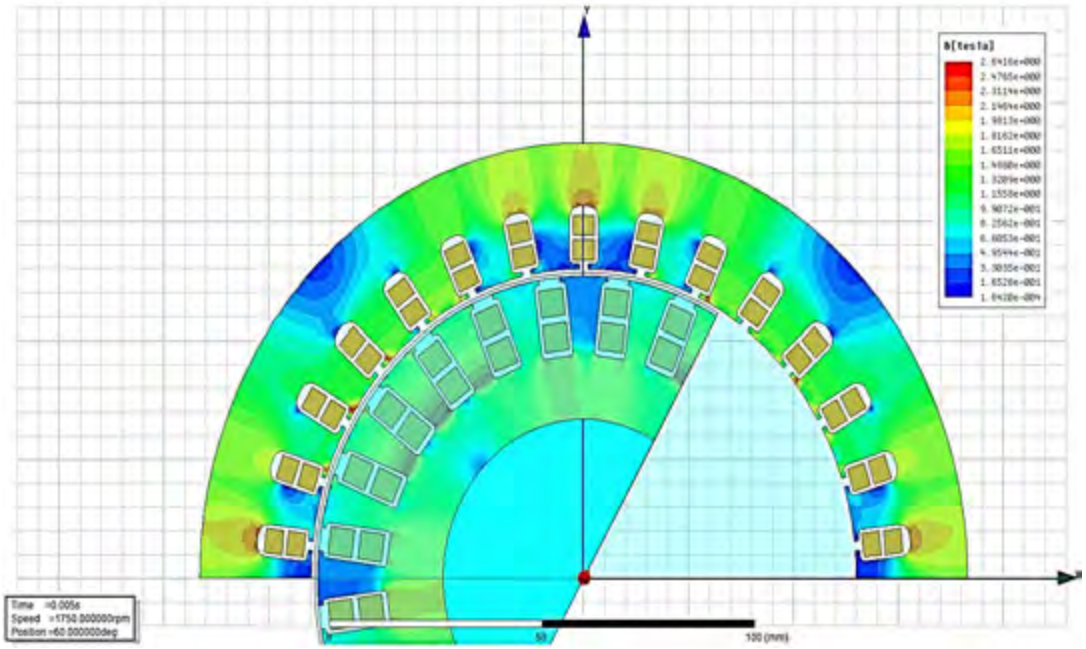

Fig. 7.2 The micro-DFIG flux current densities in the stator and the rotor.

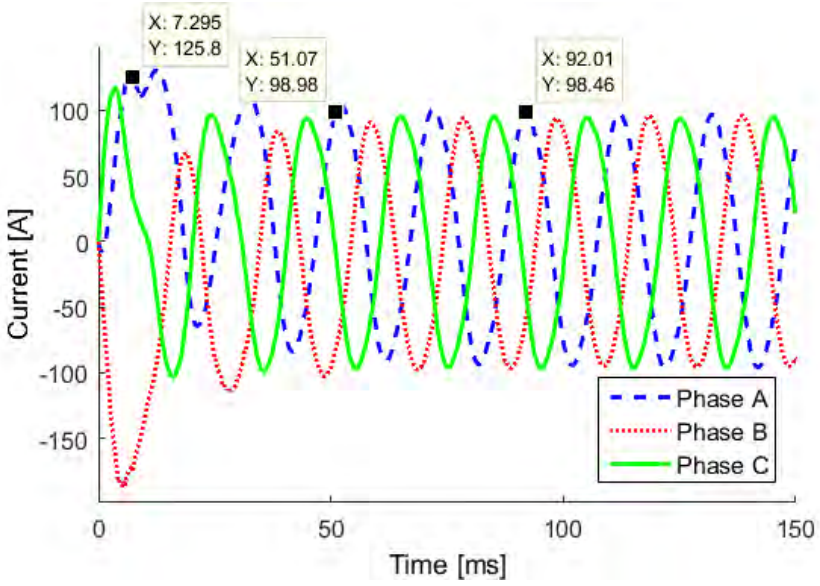

Fig. 7.3 The micro-DFIG 3-phase stator current.

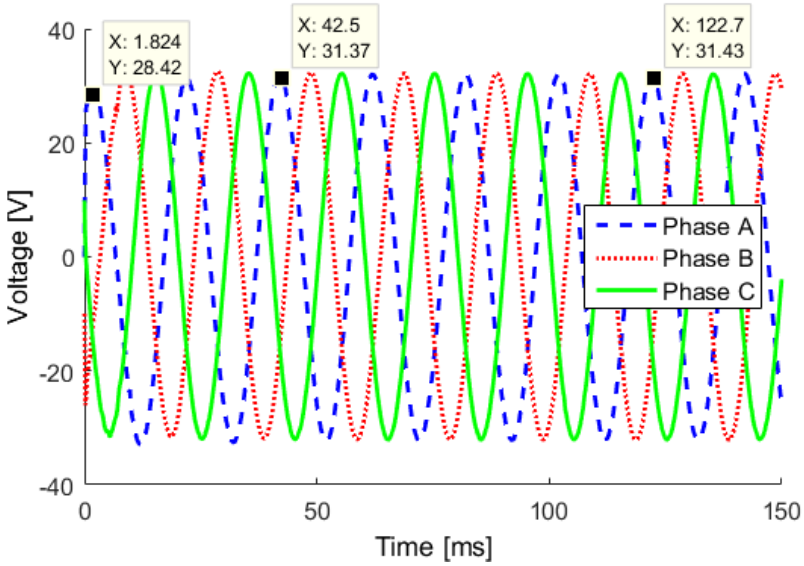

Fig. 7.4 The micro-DFIG 3-phase stator voltage.

8. Prototyping and Identification of micro-DFIG

In the previous chapter, the process of designing the micro-DFIG based on the reference design has been discussed. The analytical design has been verified by Maxwell 2D and 3D. Maxwell has also been employed to certify the objective of the designed micro-DFIG. In this chapter, the prototyping process is discussed and the equivalent circuit parameters are determined.

8.1 The Prototyping Process

The machine is composed of various parts such as the shaft, slip rings, bearings, rotor, and stator. These components are hosted in a casing. Here, the manufacturing process begins with purchasing an old 7.5kW 3-phase motor (table 8.1). The machine's frame and the other parts such as the slip rings and bearings are used in order to reduce time and cost. New cores and windings were prototyped and installed in the machine.

Table 8.1 The details of 7.5kW wound rotor induction motor.

Parameter	Value
Power [kW]	7.5
Rated line voltage, [V]	220
Rated line current, [A]	27
Power factor	0.75
Rated speed [rpm]	1420
Frequency [Hz]	50

All of the parts (frame, fan, and slip rings) are employed from a purchased machine as shown in figure 8.1. The outside stator diameter is smaller than the internal diameter of the frame. Thus, it is increased to fit the stator core in the casing. The stator back iron core will increase, however, it will not affect the micro-DFIG's dynamic behaviour. This is due to it not having an effect on the mentioned parameters in chapter 7 such as the airgap flux density. It will only decrease the stator core flux density as well as increase the volume of materials which is not cost efficient. The prototyped cores are shown in figure 8.2. Appendix B presents the stator, the rotor, and the shaft sketches. SURA M530-65A silicon-steel is employed to laminate the stator and the rotor cores. The thickness of each lamination is 0.5mm. Appendix C better presents the details of the SURA M530-65A. The laminations of the stator and the rotor cores are laser cut according to their sketches and placed on the shaft. It is important to note that the key way is skewed on the shaft in order to skew the rotor slots.

Fig. 8.1 The wound rotor induction motor's parts are used for micro-DFIG

Fig. 8.2 The prototyped stator, rotor and shaft of the micro-DFIG

The winding details of the micro-DFIG are presented in table 8.2. Figure 8.3 illustrates the stator and the rotor winding design. The windings were placed according to the profiles (figure 8.4) and the micro-DFIG is assembled and baked in the oven (figure 8.5).

Table 8.2 The micro-DFIG winding details.

Parameter	Stator	Rotor
Turn per Coil	4	4
Winding Layers	2	2
Parallel Branches	2	1
Coil pitch	7	5
Number of strands	2	3
Wire diameter range[mm]	1.829	0.724

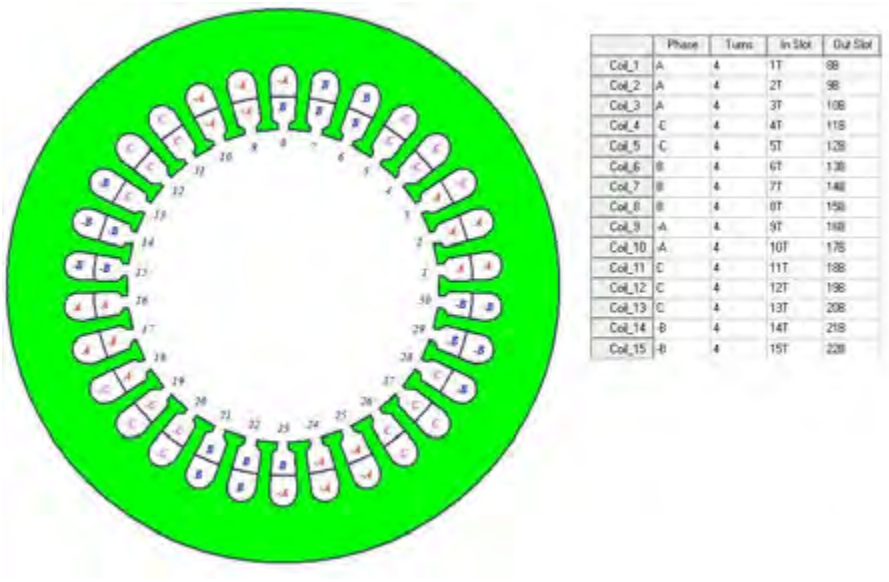

	Phase	Turns	In Slot	Out Slot
Coil_1	A	4	1T	8B
Coil_2	A	4	2T	9B
Coil_3	A	4	3T	10B
Coil_4	C	4	4T	11B
Coil_5	C	4	5T	12B
Coil_6	B	4	6T	13B
Coil_7	B	4	7T	14B
Coil_8	B	4	8T	15B
Coil_9	-A	4	9T	16B
Coil_10	-A	4	10T	17B
Coil_11	C	4	11T	18B
Coil_12	C	4	12T	19B
Coil_13	C	4	13T	20B
Coil_14	-B	4	14T	21B
Coil_15	-B	4	15T	22B

a)

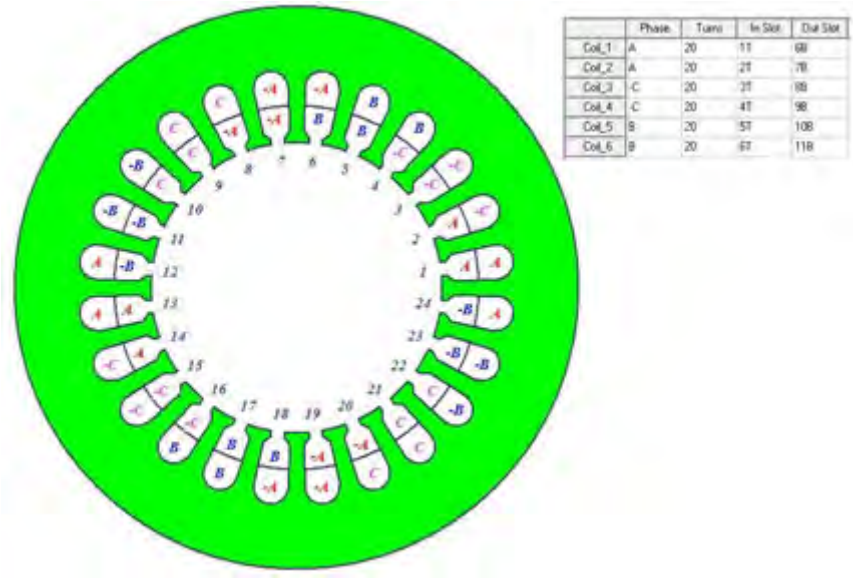

	Phase	Turns	In Slot	Out Slot
Coil_1	A	20	1T	6B
Coil_2	A	20	2T	7B
Coil_3	-C	20	3T	8B
Coil_4	-C	20	4T	9B
Coil_5	B	20	5T	10B
Coil_6	B	20	6T	11B

b)

Fig. 8.3 The micro-DFIG winding's profile for a) the stator and b) the rotor.

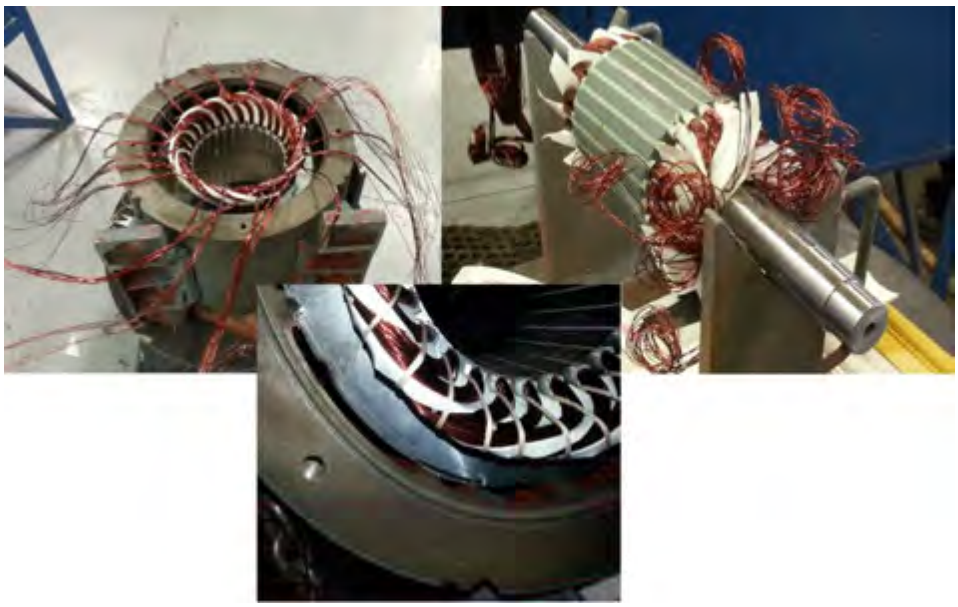

Fig. 8.4 Placement of windings into the micro DFGI's slots.

a)

b)

Fig. 8.5 The micro-DFIG's a) schematic parts and b) the final assemble.

8.2 Test's Rig

A test bench is required in order to test the micro-DFIG. The output voltage of the micro-DFIG is 3-phase 20.9 (phase voltage) volts, which is quite low. A transformer is designed and prototyped to connect the micro-DFIG to the grid (figure 8.6). Table 8.3 illustrates the details of the transformer.

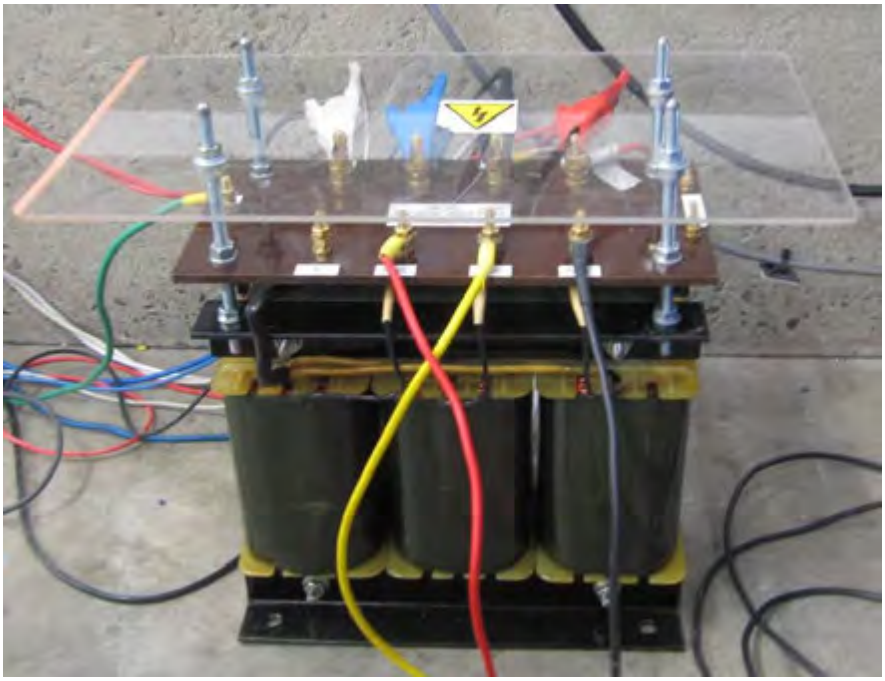

Fig. 8.6 The prototyped transformer to connect the micro-DFIG to the grid.

Table 8.3 The transformer's detail.

Parameter	Value
Power [kVA]	5.5
Primary voltage [V]	40
Primary current [A]	79
Secondary voltage [V]	380
Secondary current [A]	8.3

Yokogawa WT1800 is employed to capture data and California Instruments model MX30 is adapted as a power supply. Figure 8.7 shows the lab set-up for testing the micro-DFIG.

8.3 Identification of Equivalent Circuit Parameters

IEEE Standard 112 presents the procedure for testing IMs and for determining the equivalent circuit parameters. DFIGs are also tested using IEEE Standard 112. These machines have a slightly different design structure due to the presence of rotor windings. In the testing, the number of coil turns is assumed to be equal for both the stator and rotor but are in fact not equal. This assumption would decrease the accuracy of the results [31], [106], [185].

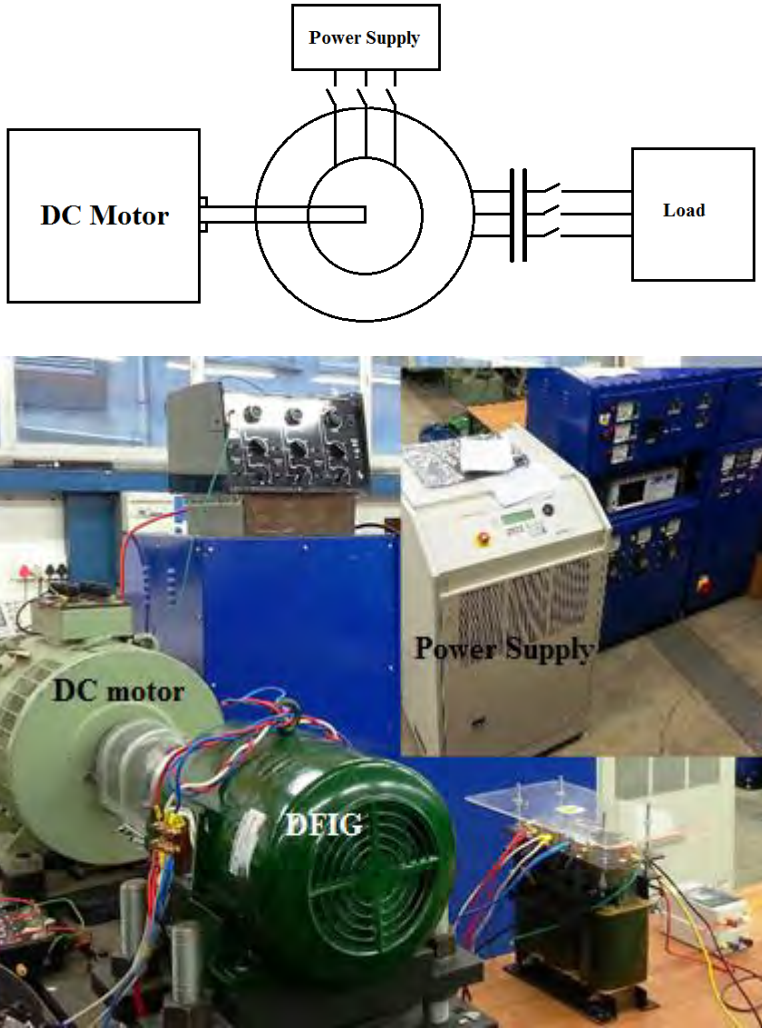

Fig. 8.7 Set up for lab tests.

The stator is usually connected to the grid and induces magnetic fields on the rotor winding. The magnetic fields are strong enough to produce electromagnetic torque. As a classic wound rotor machine, the machine will behave similarly if the stator gets short-circuited while the magnetic fields are being produced by the rotor coils. However, the stator coils have fewer turns than the rotor coils in DFIGs, which causes weaker magnetic fields and eventually weaker magnetic torque. In this chapter, Maxwell 2D is used to investigate the DFIG while it is fed through the stator or the rotor coils. In figure 8.8, the flux lines in the machine are seen. Figure 8.8a shows the flux lines when the DFIG is fed through the stator windings and the rotor windings are short-circuited, while figure 8.8b shows when the DFIG is fed through the rotor with the stator windings short-circuited. As indicated by m_1 and m_2, the flux lines are stronger when the machine is fed through the rotor. This is justified by the fact that the number of coil turns on the stator is less than the rotor in order to produce sufficient electromagnetic fields in generator mode.

The FEA proves IEEE Standard 112 tests' results would be more accurate for DFIGs if they were fed through the rotor.

Here, the equivalent circuit parameters are measured while the machine works in the motor mode at slip's' and it is also assumed that the stator winding is short-circuited. The equivalent circuit of the machine is shown in figure 8.9 when it is fed through the rotor.

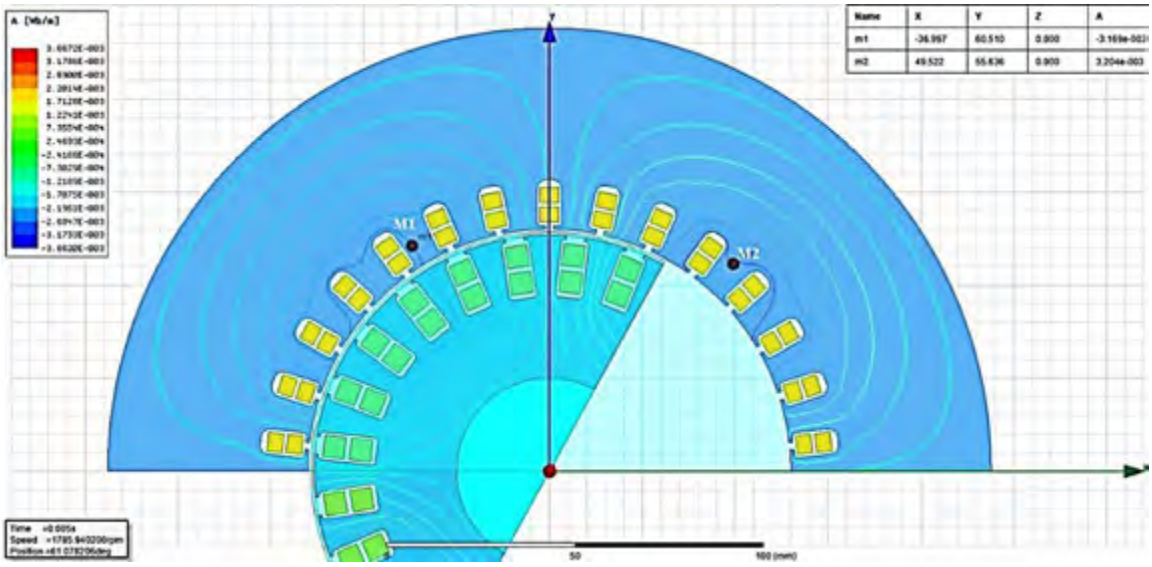

(a)

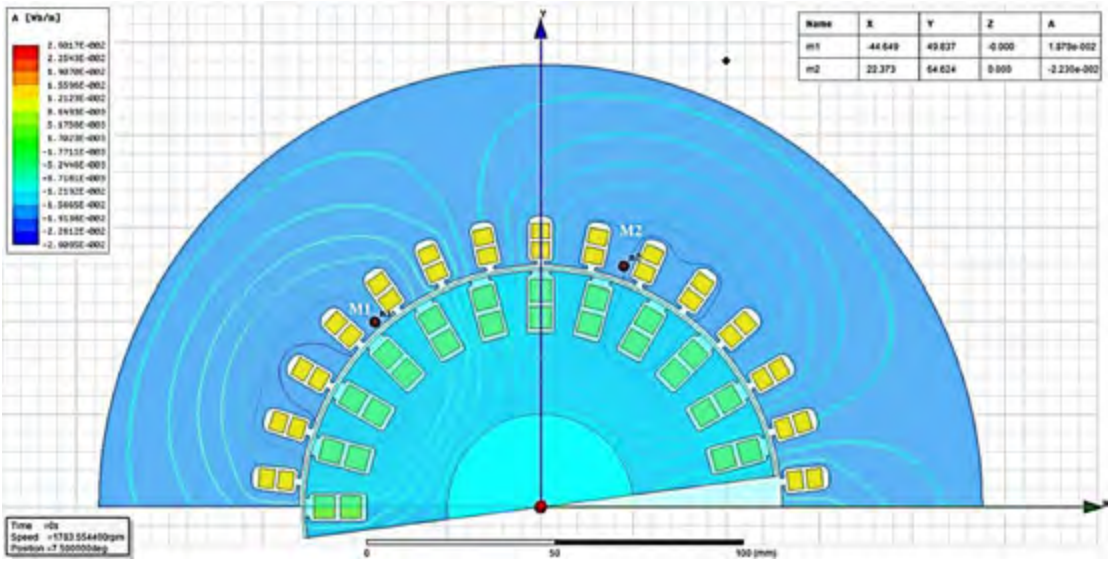

(b)

Fig.8.8 The flux lines is generated by a) the stator and b) the rotor coils.

8.3.1 No-Load Test

Figure 8.10 shows the equivalent circuit of the machine under the no-load condition. This means that the measured power under the no-load condition is dissipated across two components, the rotor core loss (r_m) and the rotor copper loss (r_2). The value of r_2 may be measured directly from the rotor windings.

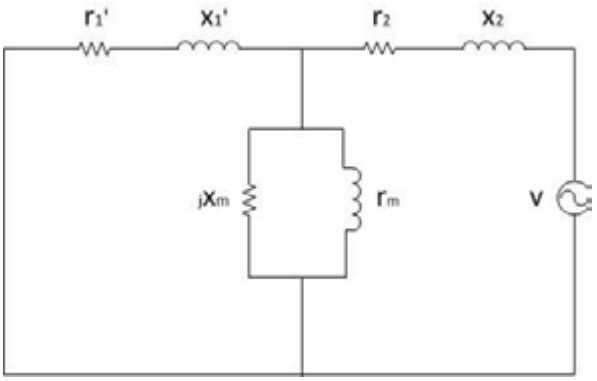

Fig. 8.9 The referred equivalent circuit of induction motor.

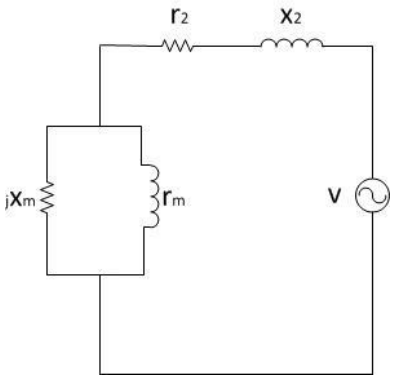

Fig. 8.10 The equivalent circuit of the induction machine under the no-load condition.

Therefore, r_m can be calculated easily as follows [186], [187]:

$$r_m = \frac{v^2}{P_{input}} - r_2 \qquad 8.1$$

Also, the input reactive power is used by the magnetizing and the rotor winding reactances. The magnetizing reactance is much greater than the rotor winding reactance, thus

$$X_m = \frac{v^2}{Q_{input}} \qquad 8.2$$

The no-load condition data of the induction machine is shown in table 8.4.

Table 8.4 The induction machine details under the no-load condition.

Rotor Resistance [Ω]	Frequency [Hz]	Active power [kW]	Reactive power [kVar]	Speed [rpm]	Stator Voltage [V]	Stator Current [A]	p.f.
1.35	50	0.089	0.344	1490	182.5	1.94	0.25

Therefore, the airgap magnetization reactance (x_m) is 97Ω and the core resistance is 375.5 Ω both on the rotor side.

8.3.2 Blocked-Rotor Test

The equivalent circuit is changed under the blocked-rotor (BR) condition as shown in figure 8.11.

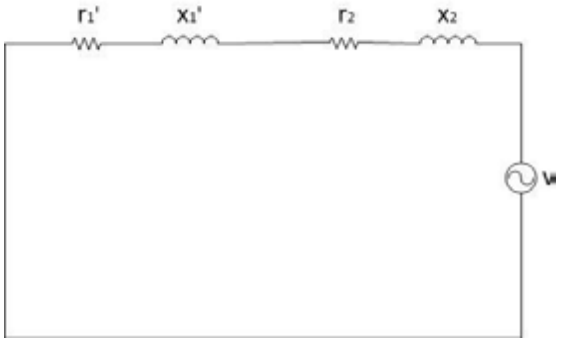

Fig. 8.11 The equivalent circuit of induction machine under the blocked-rotor condition.

It is possible to measure the referred stator resistance and it may be calculated as follows:

$$r_1{}' = \frac{v^2}{P_{input}} - r_2 \tag{8.3}$$

The total reactance is:

$$x_1{}' + x_2 = \frac{v^2}{Q_{input}} \tag{8.4}$$

Table 8.5 shows the equivalent circuit details at the blocked-rotor condition (slip=1).

Table 8.5 The induction machine details under the blocked-rotor condition.

Stator Resistance[Ω]	Frequency [Hz]	Active power [kW]	Reactive power [kVar]	Speed [rpm]	Stator Voltage [V]	Stator Current [A]	p.f.
0.142	16	1.247	1.0995	0	68	14.1	0.75

Hence, the stator resistance (r_1) and the rotor resistance (r_2) in the rotor side are 0.142Ω and 1.35Ω, respectively. The total stator and rotor reactances is 4.2Ω which means $x_2 = x_1' = 2.1\Omega$. By referring to equations 3.63, 3.64 and 3.65, the accurate value of the stator reactance is calculated as follow:

$$\lambda_s = \frac{h_{su}}{3W_s} + \frac{h_{sw}}{W_s'} = 3.84 \ , \lambda_{end} = 0.34\, q_1 \frac{l_{fs} - 0.64\beta_s\tau}{l_i} = 3.34$$
$$\lambda_{ds} = 0.9\tau_s\, (q_1\, K_{W1})^2\, K_{01} \frac{\sigma_{ds}}{K_C\, g} = 5.157 \tag{8.5}$$

$$L_{sl} = \mu_0 (2n_{c1})^2 l_i (\lambda_s + \lambda_{end} + \lambda_{ds}) \frac{N_s}{m\, {a_1}^2} = 3.22 \times 10^{-4}[H] \tag{8.6}$$

$$X_{sl} = \omega_1 L_{sl} = 0.101[\Omega] \tag{8.7}$$

and the rotor reactance is also calculated as follow:

$$\lambda_{SR} = \frac{h_{RU}}{3W_R} + \frac{h_{RW}}{W_R'} = 2.94\ ,\ \lambda_{endR} = 0.34 q_2 \frac{l_{fr} - 0.64\beta_R \tau}{l_i} = 1.23$$
$$\lambda_{dR} = 0.9\tau_R\ (q_2 K_{W2})^2 K_{02}\ \frac{\sigma_{dR}}{K_C g} = 1.811 \qquad 8.8$$

$$L_{rl}^r = \mu_0 (2n_{c2})^2 l_i (\lambda_{SR} + \lambda_{endR} + \lambda_{dR}) \frac{N_R}{m} = 0.0125\ [H] \qquad 8.9$$

$$X_{rl}^r = \omega_1 {L_{rl}}^r = 3.93\ [\Omega] \qquad 8.10$$

Table 8.6 presents the micro-DFIG's equivalent circuit parameters in per-unit system.

Table 8.6 The micro-DFIG equivalent circuit parameters.

Stator Resistance [p.u.]	Stator Reactance [p.u.]	Rotor Resistance [p.u.]	Rotor Reactance [p.u.]	Magnetization Reactance [p.u.]	Core Loss Resistance [p.u.]
0.0194	0.351	0.185	0.538	13.26	51.36

9. Transient Response of the micro-DFIG

In the previous chapters, the electrical machine's design was expressed theoretically and a reference-DFIG has been adapted. The effect of an optimum design in the WECS has been expressed earlier, relatively. Also, the dynamic modelling of the machine and the scaling policy are presented to indicate the impact of different parameters on the machine's behaviour. The reference-DFIG is scaled to maintain dynamic behaviour, in both sub-transient and transient states. Ultimately, the micro-DFIG is designed and prototyped. This chapter presents scenarios to compare the transient behaviour of the reference-DFIG and micro-DFIG by employing Maxwell 3D. The micro-DFIG is also tested under similar scenarios.

9.1 Introduction

The machine is required to be under transient conditions in order to display transient behaviour. In electric machines, transient conditions may be defined as follows [31], [97]:

- Prime mover torque variations for generator mode;
- Load machine torque variations for motor mode;
- Power grid faults for generator mode;
- Electric load variation in stand-alone generator mode;

Speed and voltage, current amplitudes, power, torque, and frequency vary in time during transient conditions, until they eventually stabilize to a new steady state. As noted, the proposed scaled-DFIG and reference DFIG were simulated in Maxwell 3D. The simulations were conducted in order to verify the analytical results of the scaling and design methodology. In addition, FEA would be used to verify the objective of this investigation regarding the dynamic response of the two DFIGs.

9.2 The DFIG Operation Mode

It is necessary to discuss the DFIG's operation mode before presenting the transient result. The grid-connected generators must produce power at constant voltage and frequency. DFIGs can do this by adjusting the rotor current and frequency for varying wind speeds. In addition, the voltage amplitude will remain steady as long as the specific flux value remains constant [188]. The induced stator voltage frequency depends on the rotor voltage frequency and its rotational speed:

$$f_s = f_r + f_m \quad (9.1)$$

Where f_s is the stator voltage frequency, f_r is the rotor voltage frequency and f_m is the rotor mechanical frequency, which

$$f_m = \frac{n_m \times p}{120} \quad (9.2)$$

The DFIG has two modes of operation depending on the rotational speed: sub-synchronous and super-synchronous. The positive direction of power flow is expressed as:

$$P_s = P_m - P_r \quad (9.3)$$

Where P_m is input mechanical power, P_s and P_r are the stator and the rotor power, respectively. The rotor power may be calculated:

$$P_r = T_m(\omega_m - \omega_s) \quad (9.4)$$

Where, T_m is mechanical torque and ω_m and ω_s are the mechanical and synchronous speed, respectively. The angular velocity slip expression is:

$$s\omega_s = \omega_s - \omega_m \quad (9.5)$$

By substituting the slip expression into the rotor power expression, it will be:

$$P_r = -sP_s \quad (9.6)$$

The stator power as a function of the slip is given by:

$$P_s = \frac{P_m}{1 - s} \quad (9.7)$$

Hence, the slip and the rotational speed of the rotor have an impact on the direction of the power flow. Also, the slip polarity indicates weather the power is drawn or delivered at the stator and the rotor terminals.

Here, the stator voltage frequency of the micro-DFIG is accurate in FEA results due to its ability to excite the rotor with 8.5Hz at the rated slip (17%). However, the stator voltage frequency is not 50Hz due to the inability of California Instruments to supply less than 16Hz. Here, the rotor frequency is selected as 20Hz and the stator frequency depends on the slip in the tests. By referring to table 7.2 and time constant formula ($\frac{L_s}{R_s}\left(1 - \frac{L_m^2}{L_s L_r}\right)$), this issue does not have effect on transient behaviour of the machine while testing.

9.3 FEA Transient State Results

So far, the equivalent circuit parameters for the reference DFIG, the scaled-DFIG and the prototyped-DFIG are shown in table 9.1. The efficiency is moderate, but expected for the size of the scaled-DFIG. The efficiency of the prototyped DFIG is lower compared to

the reference DFIG due to the increased copper and iron losses in the prototyped machine. The per-unit resistance and per-unit reactance are approximately equal.

Table 9.1 Comparison of Parameters for the Reference and scaled DFIGs.

Machine	**Reference DFIG**	**Scaled-DFIG**	**Prototyped Scaled-DFIG**
Power [kW]	2500	5	5
Efficiency [%]	95.7	73	65
Voltage (line to line) [V]	690	30	36.7
Stator current [A]	1675	72	72
Torque [N.m]	13270	32	32
Stator Resistance (R_s) [p.u.]	0.018	0.018	0.0194
Stator Leakage Reactance (X_s) [p.u.]	0.346	0.349	0.351
Stator Time Constant [S]	0.0512	0.0493	0.0477
Rotor Resistance (R_r)[p.u.]	0.022	0.133	0.185
Rotor Leakage Reactance (X_r)[p.u.]	0.4	0.526	0.538
Magnetization Reactance (X_m)[p.u.]	10.85	13. 5	13.26

As expected, the magnetization reactance is increased by 25% from the reference DFIG to the prototyped DFIG. The prototyped DFIG's time constant is approximately 50ms. Figure 9.1 shows the equivalent circuit which is assigned for the reference DFIG and micro-DFIG in FEA. The circuit is only included on the stator side of DFIGs.

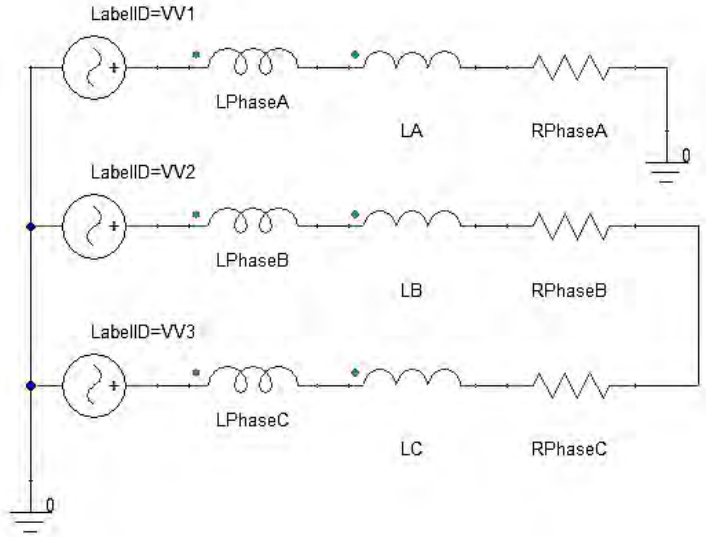

Fig. 9.1 The micro-DFIG assigned equivalent circuit.

The rotor side of the DFIGs is assumed to be connected to a converter and gets excited through the grid. Therefore, the test scenario is as follows: the rotor excites through a converter and suddenly the stator is connected directly to loads when it rotates at the rated speed (1750rpm). Phase A of the reference machine and scaled-DFIG are connected to the earth at 150ms. The dynamic behaviour of the DFIG and scaled-DFIG are shown in figure 9.2 and figure 9.3. Figures 9.2a and 9.3a represent the fact that the reference DFIG and the scaled-DFIG speeds are constant while the generators experience start-up and

short-circuit conditions. Figures 9.2b and 9.3b indicate the electromagnetic characteristics of the reference DFIG and scaled-DFIG, respectively. Three critical points are observed until 50ms in both graphs. The reference machine's electromagnetic torque decreases from -10 to -13.7 (kN.m) and the scaled-DFIG's electromagnetic torque reduces from -26 to -28.8 (N.m). The electromagnetic torque also falls immediately after short-circuit and their graphs' shapes become triangular, in both graphs. Their stator currents are presented in figures 9.2c and 9.3c respectively. The reference machine output current decreases from -1630A to -2050A and it settles after 50ms. The scaled-DFIG's stator current starts from 115A and ends up at 100A at 50ms. Their short-circuit behaviour is the same and their currents in phase-A rise dramatically due to experiencing almost zero load resistance (only stator resistance). Figure 9.2d and figure 9.3d show the stator voltages of the reference DFIG and scaled-DFIG, respectively. The reference machine voltage increases gradually form 675V to 692V within 50ms. The 3-phase voltage also became unbalanced after a short-circuit at 150ms. The scaled-DFIG's stator voltage behaviour appears to follow that of the reference DFIG's behaviour when the machine is connected to the load and it is short-circuited. The stator voltage increases to the rated voltage and rests at 30V line-to-line and it becomes unbalanced after short-circuit at 150ms as well. These figures present the induced stator voltages and also show that the voltages are not zero in phase-A after the short-circuit.

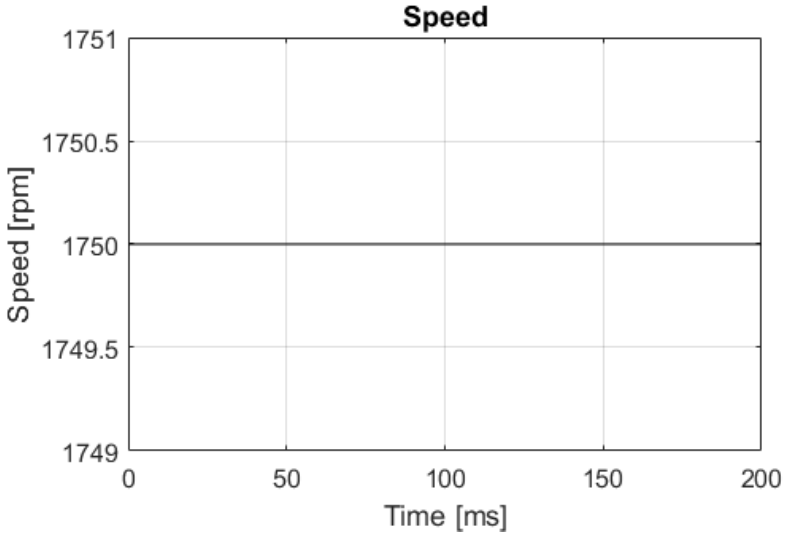

(a)

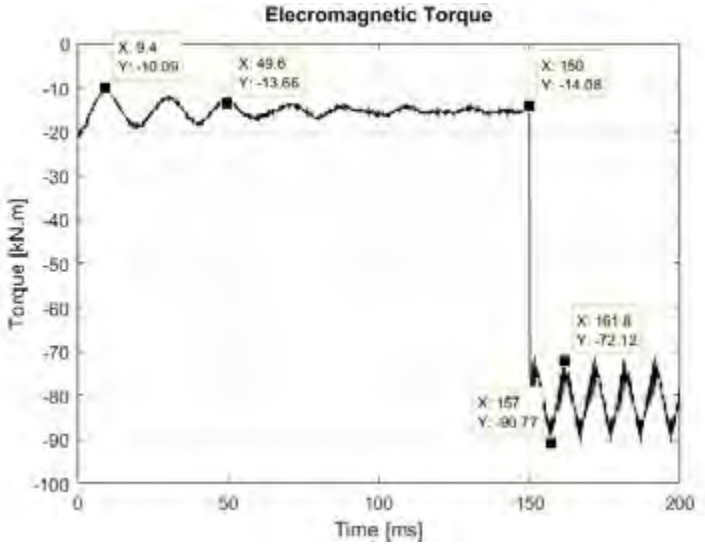

(b)

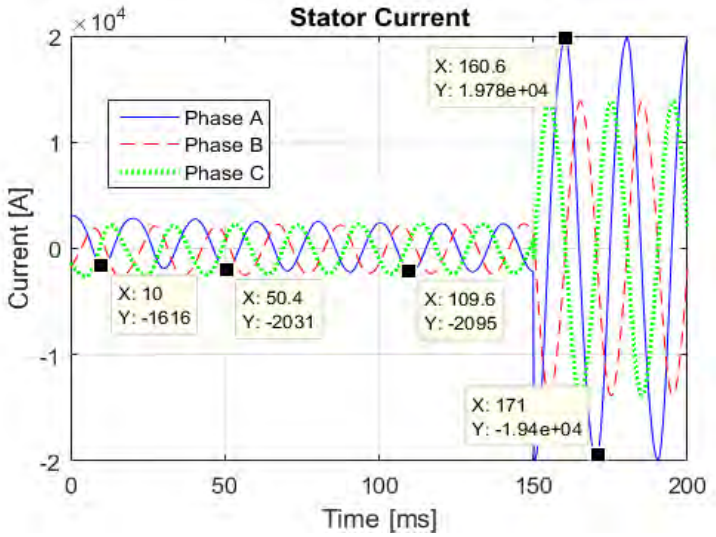

(c)

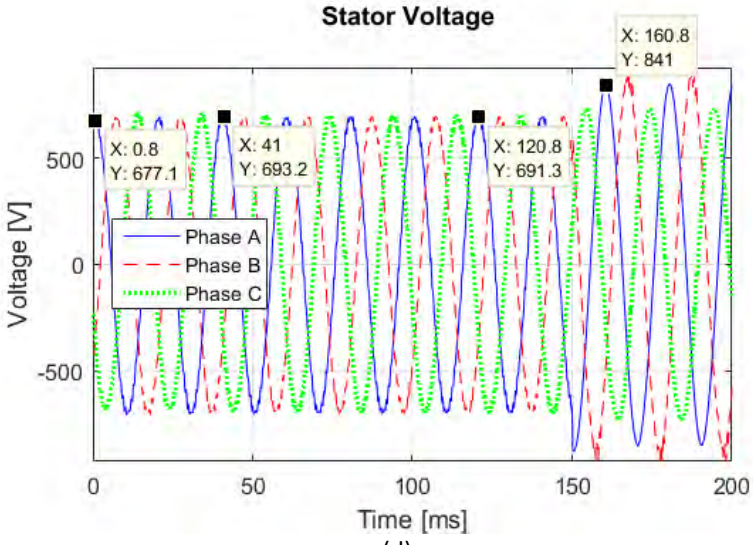

(d)

Fig. 9.2 The reference DFIG FEA results a) rotor rotational speed b) electromagnetic torque c) stator current d) stator voltage.

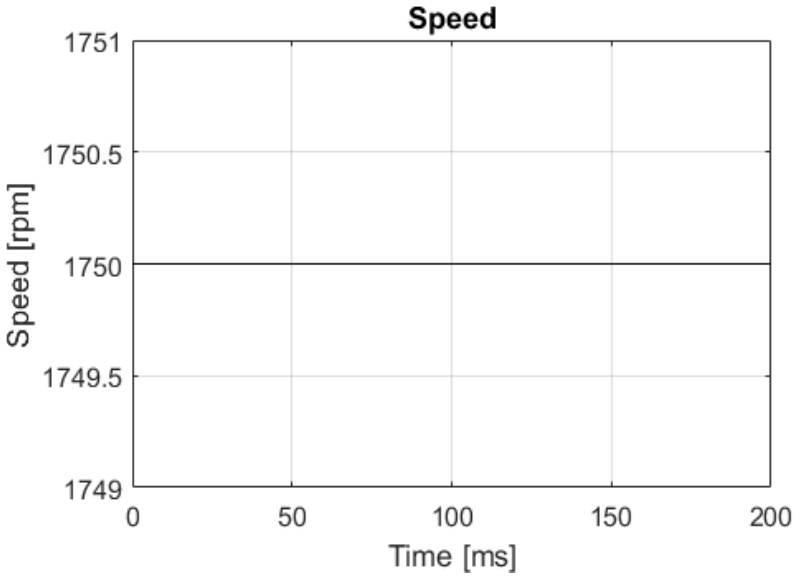
Speed
1751
1750.5
1750
1749.5
1749
Speed [rpm]
0
50
100
150
200
Time [ms]

(a)

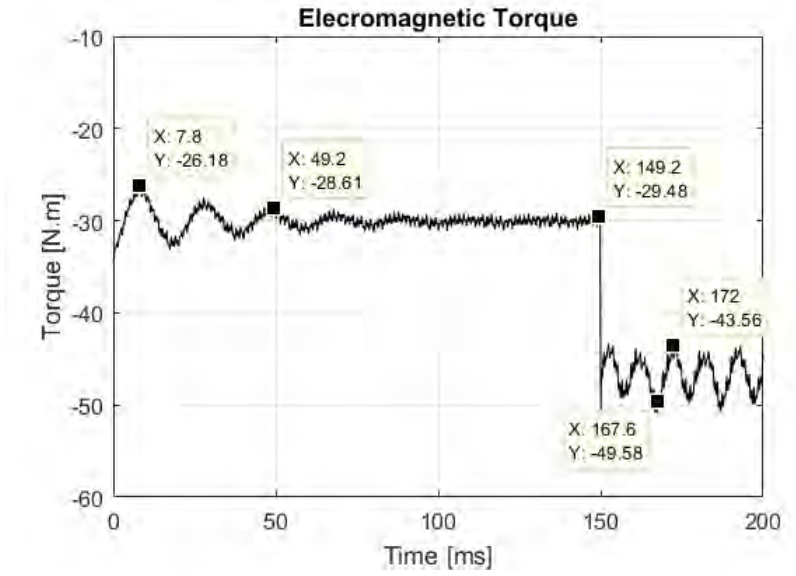
Elecromagnetic Torque
-10
-20
-30
-40
-50
-60
Torque [N.m]
X: 7.8
Y: -26.18
X: 49.2
Y: -28.61
X: 149.2
Y: -29.48
X: 172
Y: -43.56
X: 167.6
Y: -49.58
0
50
100
150
200
Time [ms]

(b)

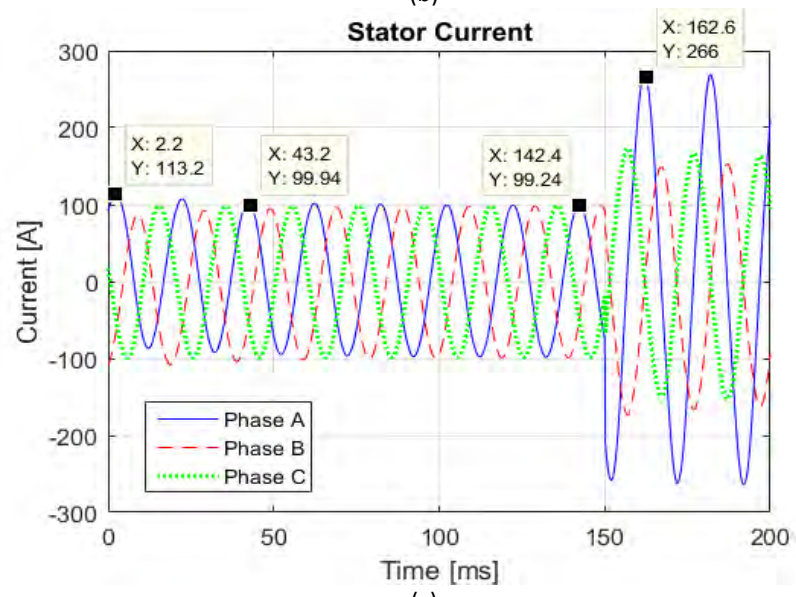
Stator Current
300
200
100
0
-100
-200
-300
Current [A]
X: 2.2
Y: 113.2
X: 43.2
Y: 99.94
X: 142.4
Y: 99.24
X: 162.6
Y: 266
Phase A
Phase B
Phase C
0
50
100
150
200
Time [ms]

(c)

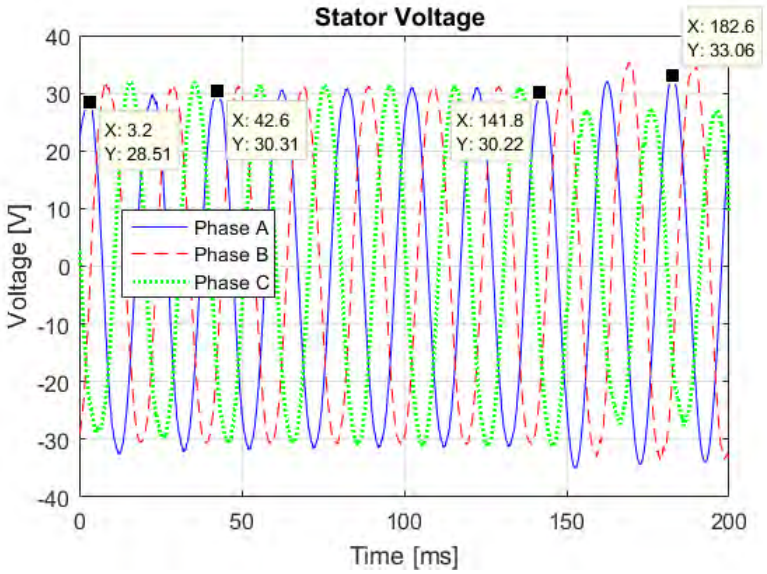

(d)

Fig. 9.3 The scaled-DFIG FEA results a) rotor rotational speed b) electromagnetic torque c) stator current d) stator voltage.

The short-circuit scenario was performed to place the DFIGs under transient conditions in Maxwell 3D. The reference-DFIG and the micro-DFIG circuits were shorted to earth at 150ms. It proves that their dynamic behaviours are similar in the transient state. Therefore, the micro-DFIG design is acceptable.

9.4 The micro-DFIG Transient State Results

The experimental results are compared to FEA results for the scaled-DFIG, since experimental results are not available for the reference DFIG. Therefore, the scaled-DFIG is tested under the same conditions as the FEA simulation, however, the short-circuit conditions were not tested due to concerns about safety of the operator and lab facilities. As shown in figure 8.7, the micro-DFIG is excited by California Instruments and the stator is connected to the load through the transformer. The prototyped DFIG is driven by a DC motor. It is connected to a balance load on the stator through a transformer. A California Instrument MX30 programmable power supply is connected to the rotor and acts as a converter. The data is captured by means of a Yokogawa WT1800 power analyser.

In order to get the machine to its start-up condition, the machine is rotated until it gets to 1800rpm while the stator is not connected to the load. The machine is tested by suddenly connecting it to the load and the results are shown in figure 9.4. The speed is reduced as presented in figure 9.4a. Figure 9.4b and 9.4c show an overshoot in the output power and stator current at about 100ms because the electromagnetic fields of the rotor and stator coils interact. In figure 9.4b, the electrical transient domain starts from about 108ms and it becomes steady at about 160ms. The stator current transient state in phase-A starts from 102ms and it takes 53ms to reach steady-state.

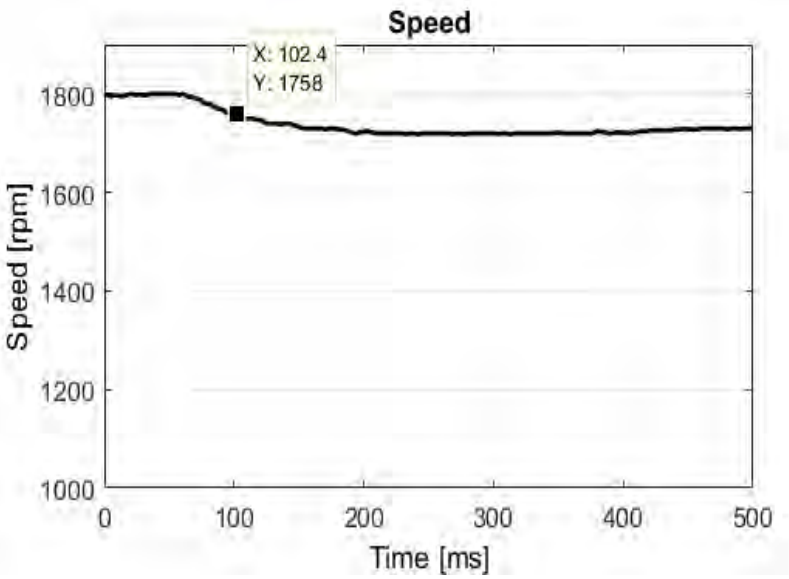
Speed
X: 102.4
Y: 1758
Speed [rpm]
Time [ms]

(a)

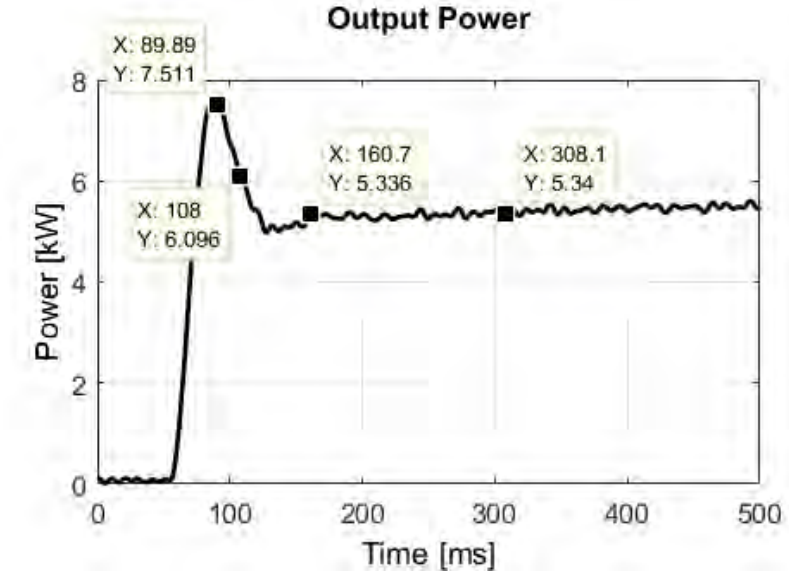
Output Power
X: 89.89
Y: 7.511
X: 160.7
Y: 5.336
X: 308.1
Y: 5.34
X: 108
Y: 6.096
Power [kW]
Time [ms]

(b)

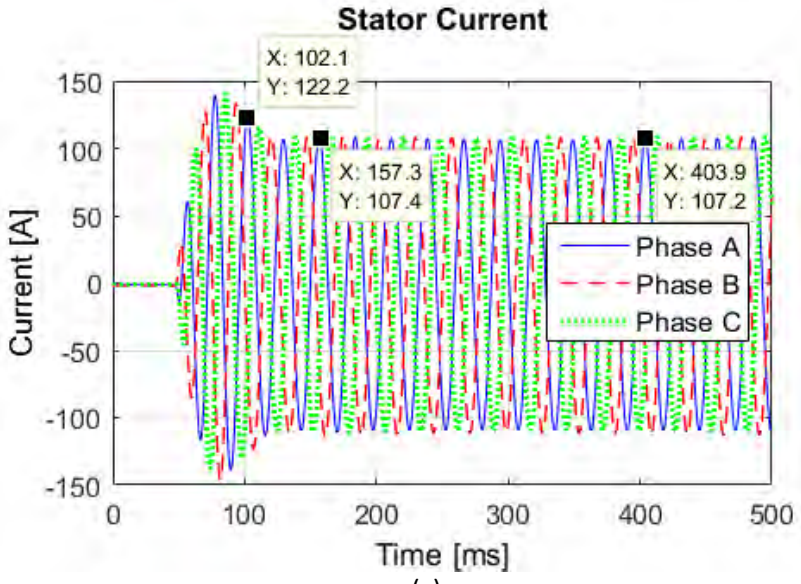
Stator Current
X: 102.1
Y: 122.2
X: 157.3
Y: 107.4
X: 403.9
Y: 107.2
Phase A
Phase B
Phase C
Current [A]
Time [ms]

(c)

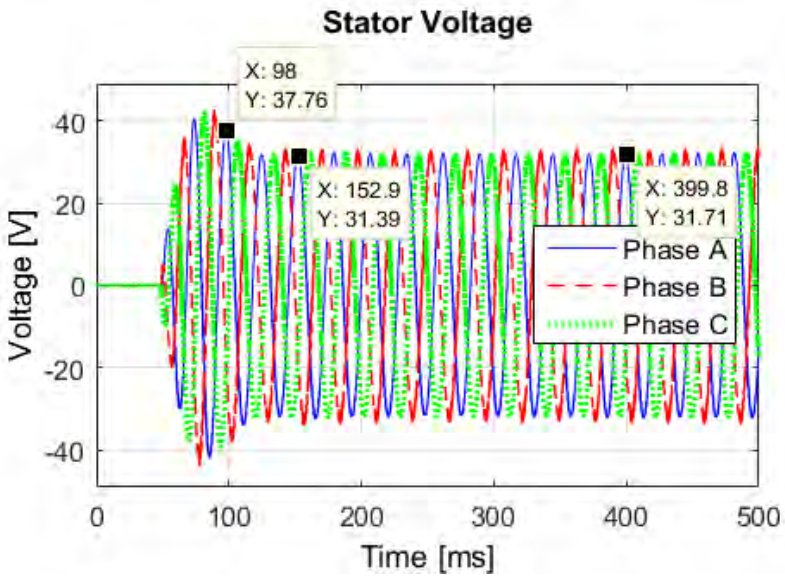

(d)

Fig. 9.4 The scaled-DFIG test results a) rotor rotational speed b) electromagnetic torque c) stator current d) stator voltage when the machine starts to operate.

Figure 9.4d indicates that the stator voltage has increased to 38V as a result of electromagnetic fields interacting and three peaks are observed from 100 to 153ms. The results in figures 9.3 and 9.4 show that the scaled-DFIG and the prototyped DFIG behave the same under the start-up condition. Figure 9.5 presents the results of the prototyped DFIG when the load is increased by 30 percent.

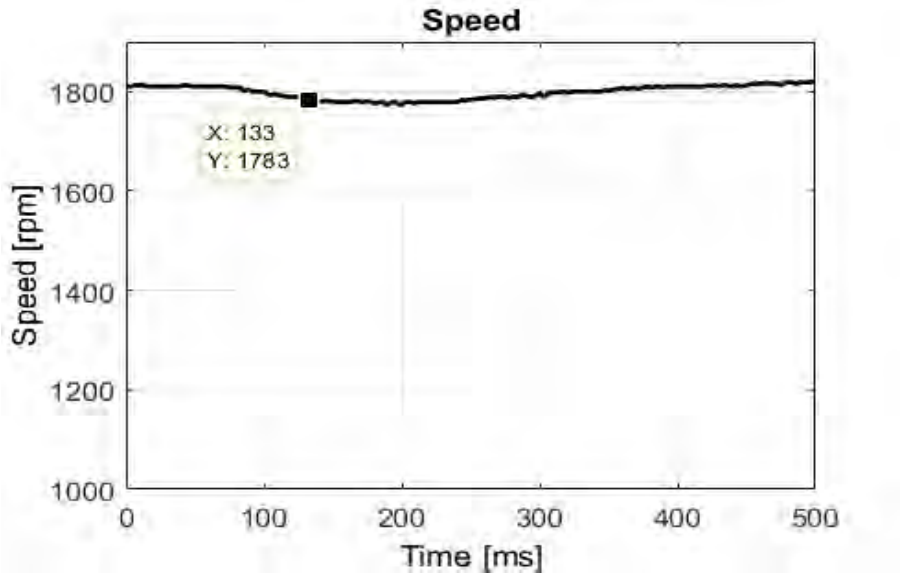

(a)

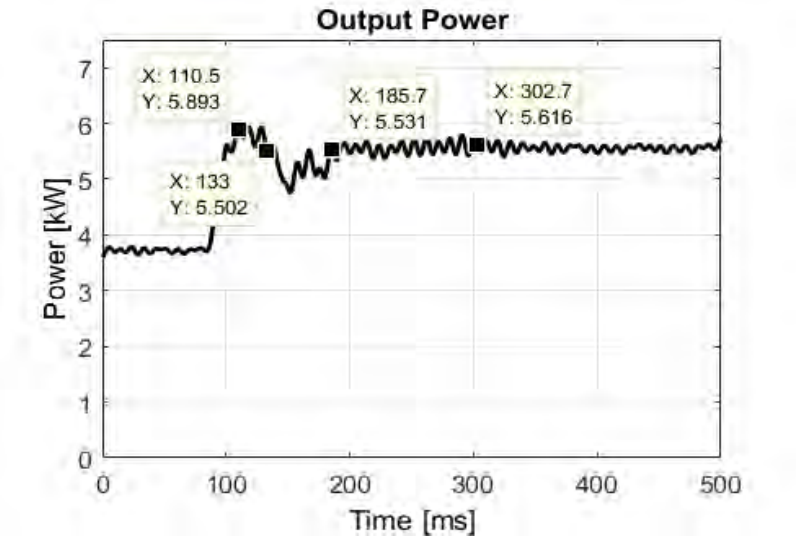

(b)

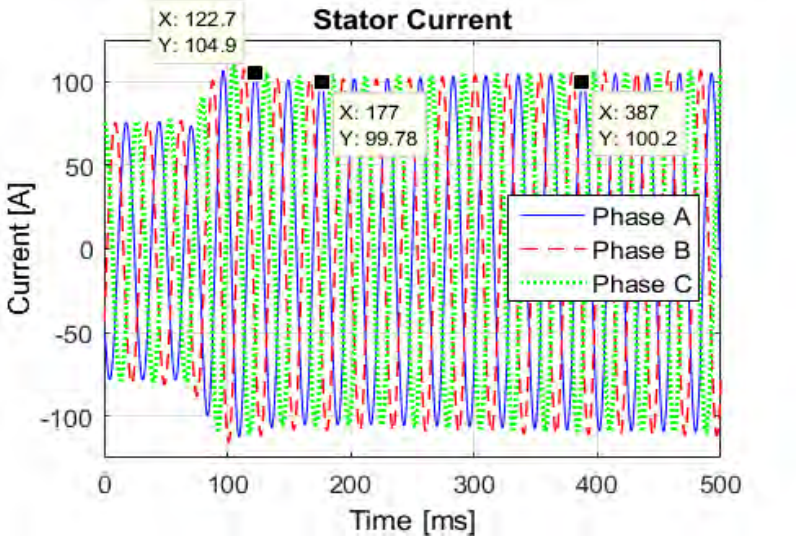

(c)

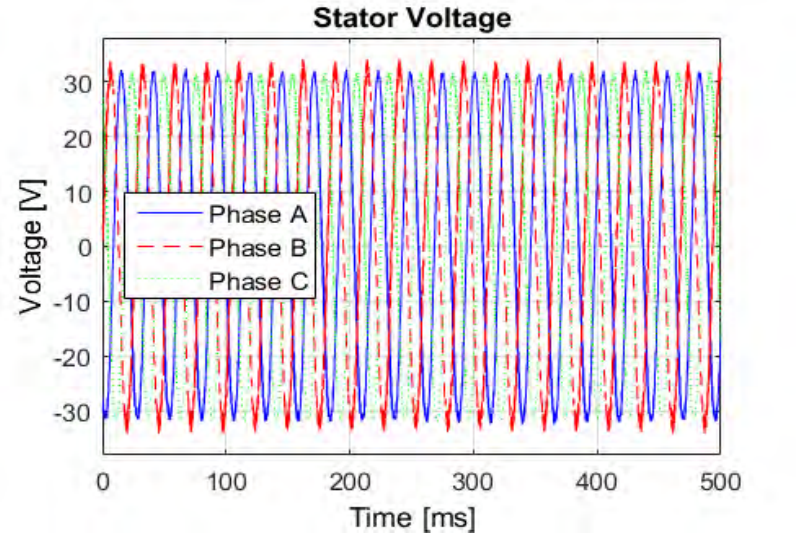

(d)

Fig. 9.5 The scaled-DFIG test results a) rotor rotational speed b) electromagnetic torque c) stator current d) stator voltage when the machine's load increases.

The load is increased from 3.8kW to 5.6kw when the rotational speed is 1800rpm. As a result: sudden increasing the electromagnetic torque on the shaft, the output power graph peaks at about 100ms while the rotational speed drops slightly until 133ms and then starts to return to the initial speed. It can be observed that the electrical transient domain is between 133ms and 185ms as shown in figure 9.5b. The output power becomes constant after 185ms when it is 5.6kW at 303ms which is very close to output power at 186ms. Figures 9.5c and 9.5d show the stator current and voltage characteristics, respectively. The stator current characteristics have a similar behaviour to the output power graph as opposed to the stator voltage. The electromagnetic fields interaction causes a significant increase at about 100ms and its time constant is 50ms in figures 9.5b and 9.5c. As expected, the stator voltage magnitude is constant in figure 9.5d. Figure 9.6 presents the result of simulation of the scaled-DFIG in FEA under the same conditions as the previous test.

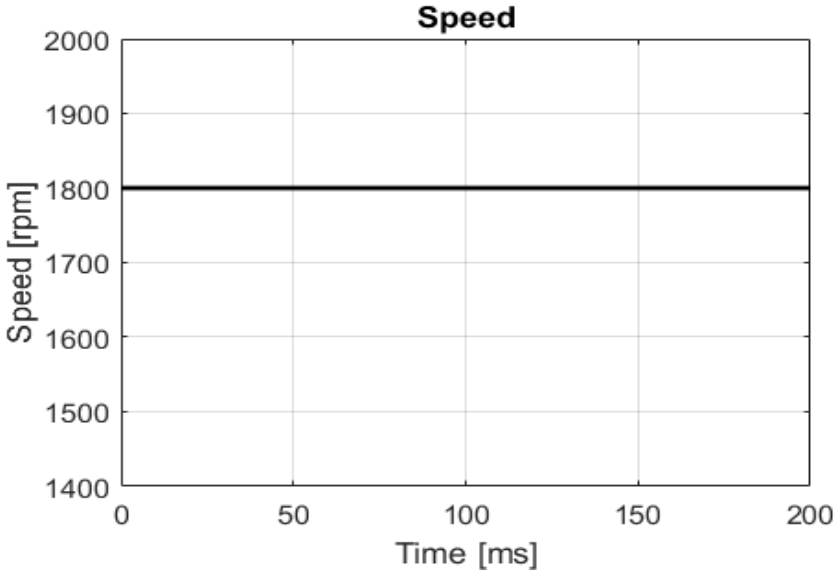

(a)

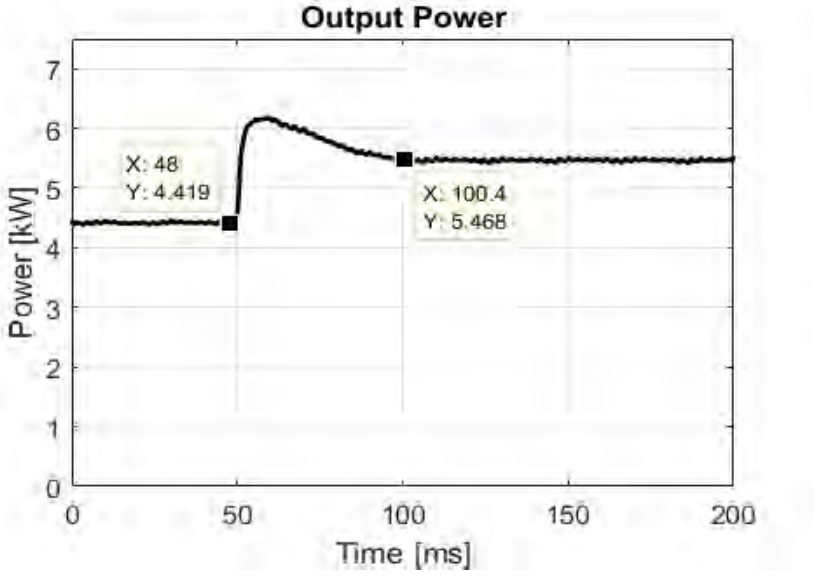

(b)

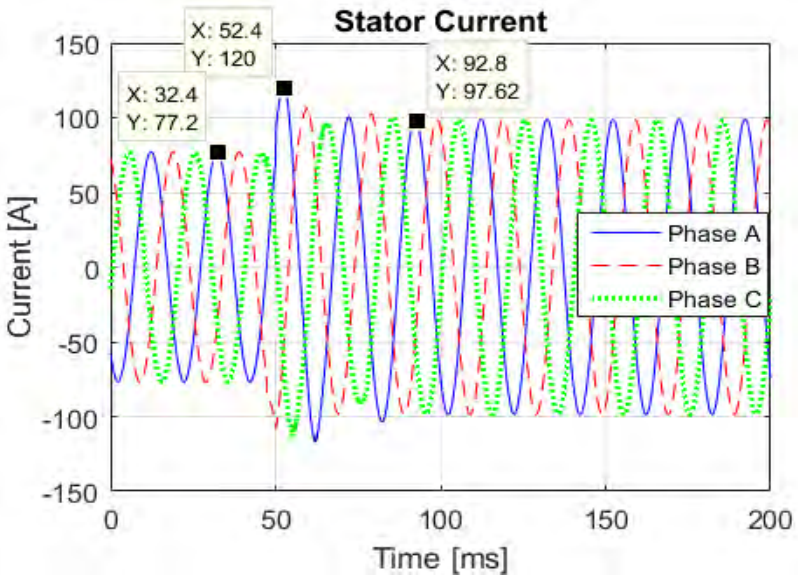

(c)

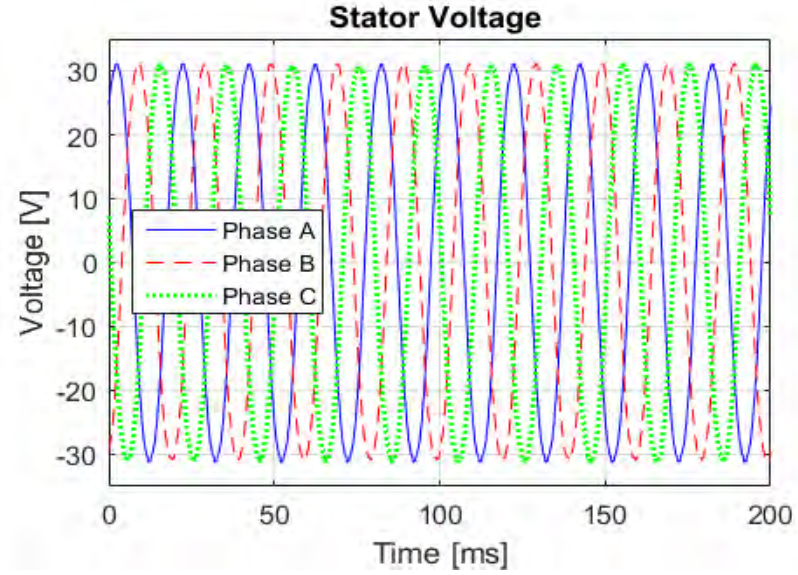

(d)

Fig. 9.6 The scaled-DFIG FEA results a) rotor rotational speed b) electromagnetic torque c) stator current d) stator voltage when the machine's load increases.

The rotational speed is constant in figure 9.6a even when the load is added at 50ms. The output power suddenly increases at 50ms and it reduces gradually to its steady-state value at 100ms. Figure 9.6c illustrates three peaks from 50 to 93ms in the Phase-A stator current. Figure 9.6d shows that the stator voltage magnitude is also steady. Figures 9.5 and 9.6 indicate that the scaled-DFIG and the prototyped DFIG have similar behaviours while their loads increase. The rotational speed profiles in the test and the FEA simulation are presented in figure 9.7a and 9.7b, respectively.

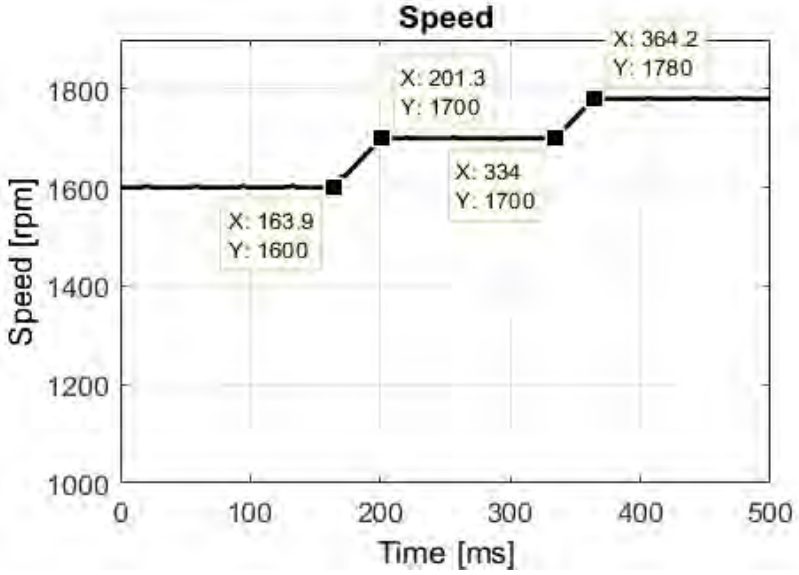

(a)

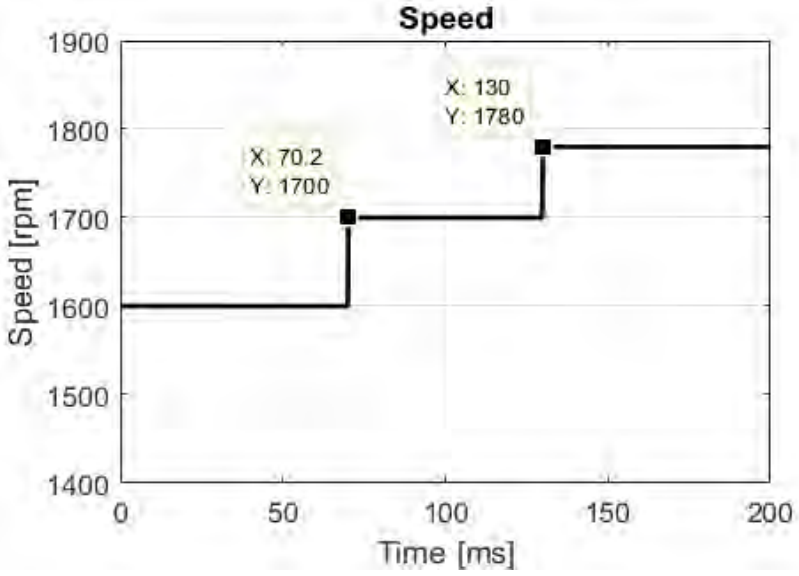

(b)

Fig. 9.7 The scaled-DFIG rotational speed graph in, a) the experiment and b) FEA simulation.

As noted, the speed ramps up between the operating points in the test but it is stepped in the FEA. In fact, there is a delay in the speed increases in the test, while it is instantaneous in the FEA simulation. Figure 9.8a and 9.8b present the output power of the scaled-DFIG based on the rotational speed profiles.

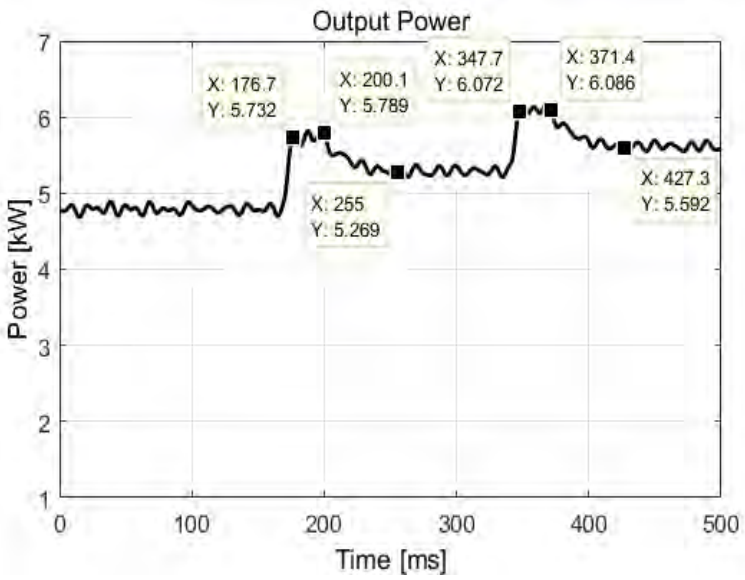

(a)

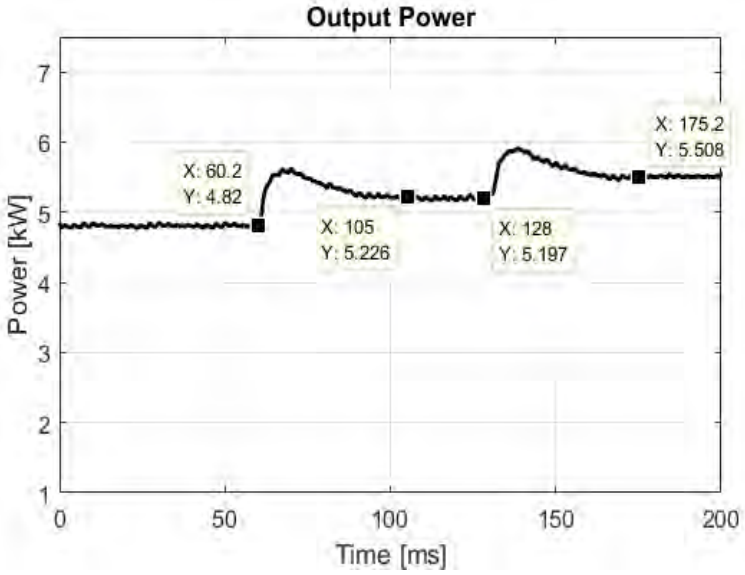

(b)

Fig. 9.8 The scaled-DFIG output power characteristics when speed increases, a) in the experiment and b) in FEA simulation.

In the laboratory test, the speed increases twice between 165-200ms and 335-370ms. The influence of the speed variations is evident in the output power graph within these periods. The output power rises dramatically when the speed increases and it decreases gradually after the rotational speed becomes constant in figure 9.8a. The FEA results show that the output power increases quickly after the rotational speed is raised and it becomes steady after about 45ms. The output power behaviour of the scaled-DFIG in the laboratory test and the FEA simulation are similar. The stator current graph varies with the rotational speed profile in the same manner as the output power. Figure 9.9 indicates the stator current of the scaled-DFIG in the test and the FEA simulation.

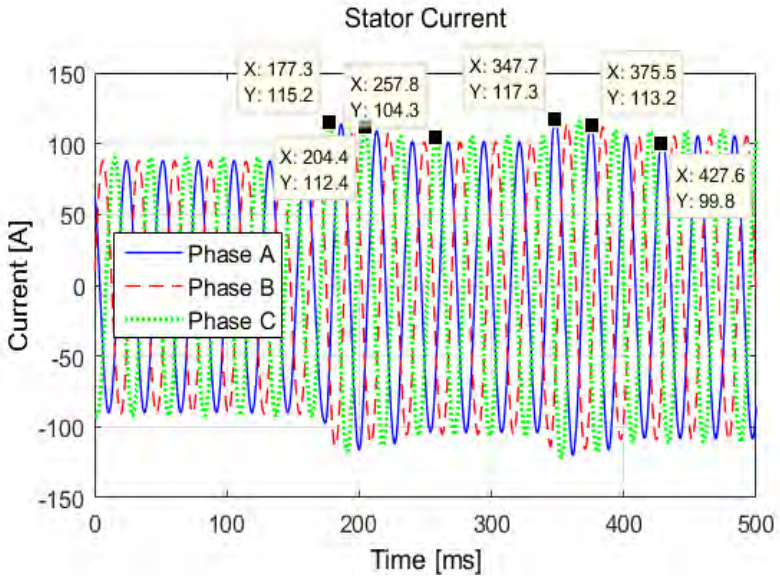

(a)

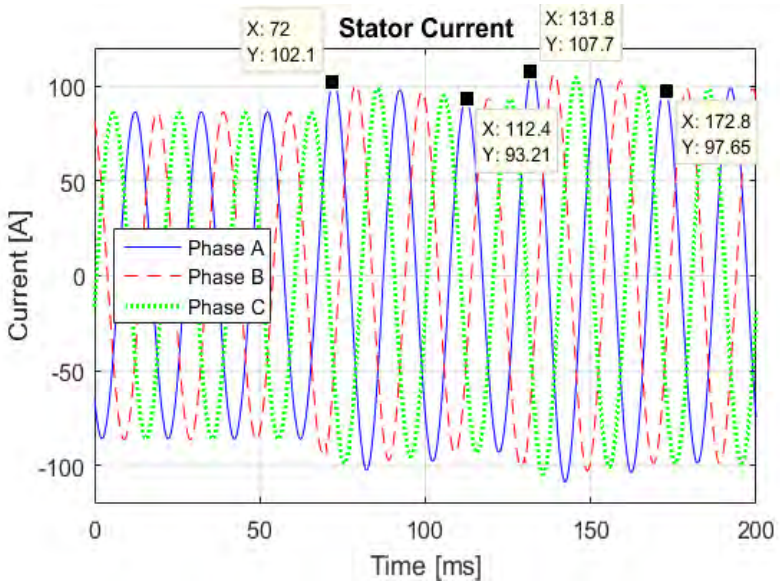

(b)

Fig. 9.9 The scaled-DFIG stator current characteristics when speed increases, a) in the experiment and b) in FEA simulation.

Figures 9.9a shows that the electrical transient domains are between 205-257ms and 376-428ms. Three peaks can also be observed in each one. The stator current settles at 101.5A and 106.5A when the speed becomes steady in each step. Figure 9.9b shows the current passes three peaks within 70-113ms and 130-175ms as it gradually reduces. The stator voltage of the scaled-DFIG in the laboratory test and FEA are presented in figures 9.10a and 9.10b, respectively. As noted, the stator voltage is constant while the speed varies.

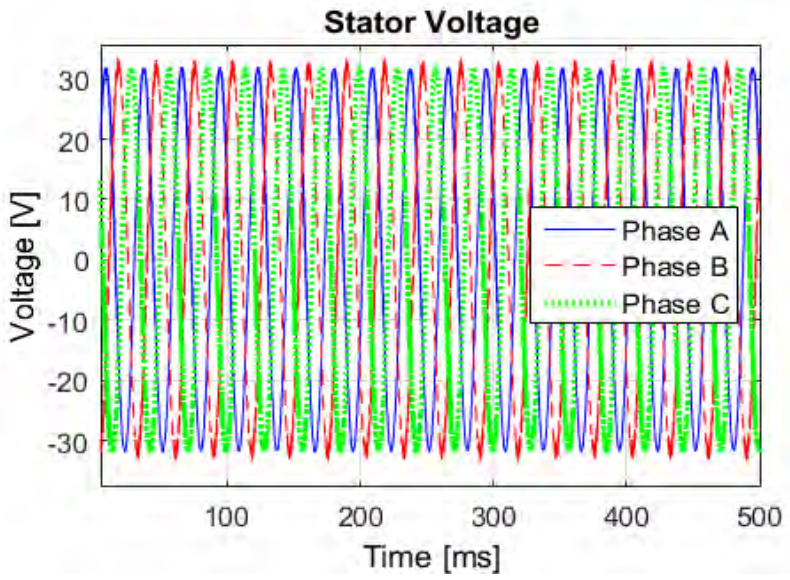

(a)

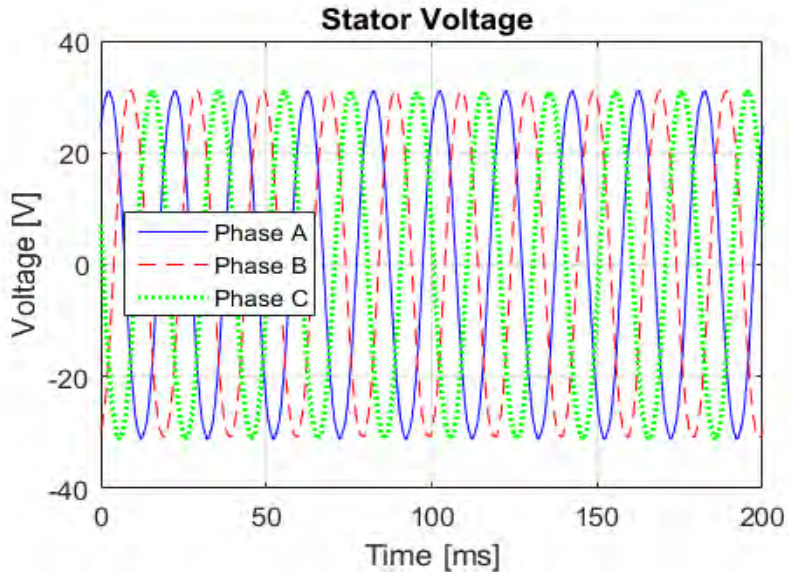

(b)

Fig. 9.10 The scaled-DFIG stator voltage characteristics when speed increases, a) in the experiment and b) in FEA simulation.

Figure 9. 11 presents the temperature of cores and windings at full-load after running for an hour.

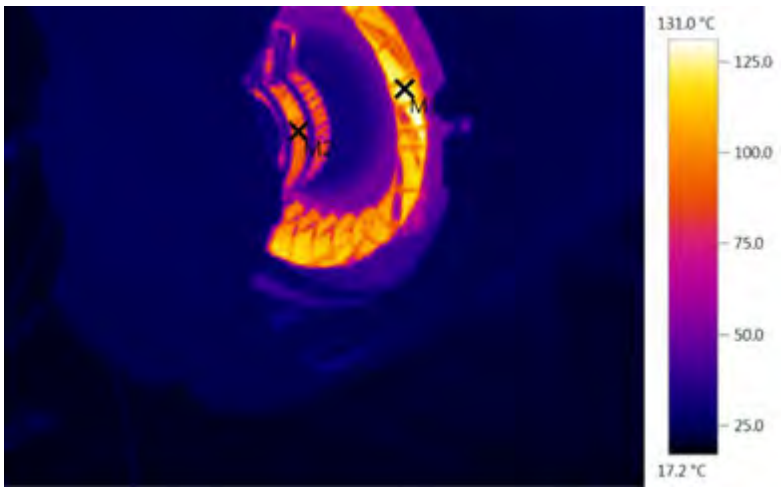

Fig. 9.11 The thermal image of the micro-DFIG at full-load.

As seen above, the maximum temperature of rotor is 120℃, the slip rings are 100℃, and the rest of the parts are less than 60℃. It proves that the cooling system of the machine is capable to transferring the heat and protecting the insulations.

10. Conclusions and Recommendations

10.1 Conclusions

Based on the finding of this project, the following conclusion can be made:

1- Wound Rotor Induction Machine Design and Reference Design:

This dissertation has expressed the analytical design of the wound rotor induction machine, following the literature review regarding induction machine design. The sizing equations of the induction machine design have been illustrated and a reference design was presented and verified in Maxwell 2D.

2- Investigation in the Wind Energy Conversion System with a DFIG:

The effect of various voltages and speeds has been investigated in the WECS with the DFIG. The investigation was necessary in order to explore the DFIG's design impact on the cost and performance of the WECS. As a result, if there is an opportunity to redesign a DFIG for the current WECS it would be reasonable to design it for a medium voltage system.

3- Investigation in the Wind Energy Integration Issues

The penetration of the wind energy in the power system has been investigated to illustrate their behaviours in the transient state. Then, the aggregation has been introduced to develop a better understanding of the integration issues. The aggregated models are introduced for specific issues but they present challenges as they are not accurate. For instance, an accurate model is still required to predict the behaviour of wind energy within the grid when there is a short-circuit. Furthermore, a single machine equivalent is also discussed, but it is not feasible to be prototyped. Each power system requires a specific model to accurately investigate the wind energy penetration within sensible time.

4- Finding Critical Characteristics in Wound Rotor Induction Machine's Transient Behaviour:

The dynamic modelling of the induction machine has been expressed by a number of equations to illustrate their transient behaviours. These equations have been transferred to the stationary frame to decrease the model difficulty. These models have been employed in FEA software to simulate the electrical machines mathematically. These models theoretically can show the effective parameters on the dynamic behaviour of the machine. These parameters can also be related to the machine's geometry. This means

that the machine can be scaled while the reference and the scaled machine behave the same during transient conditions.

5- Investigation in Dimensional Analysis and Micro-Machine's Applications

The micro-machines have been expressed with their applications. They have been used to solve the integration issues of the turbo-alternator. The dimensional analysis is also discussed to design micro-machines. As the scaled wind generator would react the same as the reference generator, it is feasible to employ them in solving the wind farm integration issues.

6- Similarity Between Transient Behaviours' of Reference DFIG and micro-DFIG

The mathematical modelling is adapted in order to identify the dominant parameters in the equivalent circuit of the DFIG, which determines its behaviour. These equivalent circuit elements must ultimately remain unchanged after the scaling process in order to maintain the same behaviour of the reference machine and the scaled-DFIG. The scaling process is outlined with the scaling factors and the scaling equation. Per-unit resistance and per-unit reactance are kept equal between the reference DFIG and scaled-DFIG. However, the magnetization reactances are different because the same airgap is used. The reference DFIG and the scaled-DFIG are verified in the FEA and were tested under a transient condition. The objective of the project was met, despite the efficiency of the scaled-machine being less than the reference machine. The prototype DFIG was also tested under the same transient conditions as FEA. There is a similarity between the FEA and the prototype DFIG at the transient region. However, there are mechanical effects which affect the test results of the prototype DFIG, which are not modelled in the FEA (Maxwell), and hence not presented in the results, even though parameters, such as inertia were implemented in the FEA software. The results show that the electrical dynamic behaviour of the simulated and prototype scaled-DFIGs are similar, which proves the objective of this investigation.

10.2 Recommendations and Future Work

Most of available FE software are facilitated to design squirrel cage induction machines and they sometimes require complicated adjustments to simulate WRIMs. For instance in the Flux, squirrel cage bars material must be replaced by copper and the machine equivalent circuit also needs to justify simulating a WRIM while the rotor slots shape still needs to be defined. Due to these challenges, Maxwell is employed to design wound rotor induction machine in this project. However, Maxwell does not cover the mechanical impacts of the machine (even though there are inertia variables that may be assigned).

Therefore, it is recommended to develop FE software for particularly wound rotor machines since they are the popular wind generators.

Since a single machine is infeasible to simulate a wind farm and as result investigate the wind integration issue, an ideal solution may be prototyping a laboratory based wind farm using micro wind generators. The laboratory wind farm can include different types of wind generators such as DFIG, SCIG, and PMSG. It should be capable of testing under different wind profiles while it interacts with the grid (depends on where it is installed).

11. References

[1] T. Ackermann, *Wind Power in Power Systems*. John Wiley, 2005.

[2] J. G. Slootweg and E. de Vries, “Inside Wind Turbines - Fixed vs. Variable Speed,” *Renew. Energy World*, pp. 30–40, 2003.

[3] I. Boldea and S. A. Nasar, *The Induction Machines Design Handbook*. CRC Press/Taylor & Francis, 2010.

[4] R. Robert, “Micromachines and Microreseaux: Study of the Problems of Transient Stability by the use of Models Similar Electromechanically to Existing Machines and Systems,” in *CIGRE*, pp. 338–346, 1950.

[5] A. Rangekar, K. V. N. Rao, M. K. Gupta, and S. N. Saxena, “Development of Time Constant Regulator for Micron-machine,” *IEEE Trans. Ind. Electron.*, vol. IE-32, 1985.

[6] S. S. Kalsi and B. Adkins, “Transient Stability of Power Systems Containing both Synchronous and Induction Machines,” *Proc. IEE*, vol. 118, no. 10, pp. 1467–1474, 1971.

[7] T. J. Hammons and A. J. Parsons, “Design of Microalternator for Power-System-Stability Investigations,” *Proc. Inst. Electr. Eng. UK*, vol. 118, no. 10, p. 1421, 1971.

[8] M. J. Jefferies and A. Wright, “New Approach to Micromachine Construction,” *Proc. Inst. Electr. Eng. UK*, vol. 117, no. 7, p. 1309, 1970.

[9] P. L. Alger, *The Nature of Induction Machines*. Gordon and Breach, 1965.

[10] V. A. Venikov and A. V Ivanov-Smolenski, “Developing Physical Models of Electrical Systems,” *Elektrichstro*, pp. 1–10, 1955.

[11] C. M. Focken, *Dimensional Methods and their Applications*. London: Arnold, 1953.

[12] S. Berchten, K. Reichert, and E. Thaler, “Micromachine for Real-Time Generator Simulation Design Limits and a Novel Solution with Adjustable Parameters,” *IEEE Trans. Energy Con.*, vol. 9, no. 12, pp. 38–39, 1989.

[13] D.W. Auckland and R. Shuttleworth, “Compensation Systems for a Micromachine Model,” *IEE Proc. C Gener. Transm. Distrib.*, vol. 128, no. 1, pp. 12–17, 1981.

[14] D. W. Auckland, R. Shuttleworth, and Y. A. A. Turki, “Micromachine Model for the

Simulation of Turbine Generators," *Transm. Distrib.*, vol. 134, no. 4, pp. 265–271, 1987.

[15] D. W. Auckland, S. M. L. Kabir, and R. Shuttleworth, "Generator Model for Power System Studies," *Transm. Distrib.*, vol. 137, no. 6, pp. 383–390, 1990.

[16] D. Ruiz, T. I. Asiain, and D. Olguin, "Teaching and Research Laboratory Simulator of Electric Power Systems," in *FIE '99. 29th Annual Frontiers in Education Conference*, p. 11B6/8-11B6/14, 1999.

[17] C. Concordia, *Synchronous Machines, Theory and Performance*. New York, 1951.

[18] J. H. Walker, *Large Synchronous Machines*. Clarendon Press, 1981.

[19] B. R. Singla, S. Marwaha, and A. Marwaha, "Design and Transient Analysis of Cage Induction Motor Using Finite Element Methods," in *2006 International Conference on Power Electronic, Drives and Energy Systems*, pp. 1–5, 2006.

[20] L. Livadaru, A. Munteanu, A. Simion, and C.-G. Cantemir, "Design and finite element analysis of high-density torque induction motor for traction applications," in *2015 9th International Symposium on Advanced Topics in Electrical Engineering (ATEE)*, pp. 211–214, 2015.

[21] S. Williamson, "Implementation of finite-element analysis in a cage induction motor electrical design program," in *Seventh International Conference on Electrical Machines and Drives*, pp. 57–61, 1995.

[22] R. Richter, "Electric Machines," Bassel/Stuttgart: Verlag Birkhauser, 1954.

[23] P. L. Cochran, *Polyphase Induction Motors*. M. Dekker, 1989.

[24] P. L. Alger, *Induction Machines, Their Behavior and Uses*. Gordon and Breach, 1970.

[25] T. A. Lipo, *Introduction to AC Machine Design*. Wisconsin Power Electronics Research Center, University of Wisconsin, 2004.

[26] E. S. Hamdi, *Design of Small Electrical Machines*, 1st ed. Chichester: Wiley, 1994.

[27] F. F. Tang and X., *Induction Machine Design Handbook*. Shanghai, China: China Machine Press, 2002.

[28] Ca.mouser.com, "Mouser Electronics - Electronic Components Distributor." 2016.

[29] "Wind Energy Foundation," 2016. [Online]. Available:

http://windenergyfoundation.org/. [Accessed: 09-Jul-2016].

[30] "U.S. Motors," 2016. [Online]. Available: http://www.usmotors.com/. [Accessed: 11-Apr-2016].

[31] I. Boldea, *The Electric Generators Handbook*. CRC/Taylor & Francis, 2006.

[32] I. Boldea, *Linear Electric Machines, Drives, and Maglevs Handbook*, 1st ed. Boca Raton, Fla.: CRC Press, 2013.

[33] E. R. Laithwaite, *Induction Machines for Special Purposes*. Newnes, 1966.

[34] C. A. Gross, *Electric Machines*. CRC Press, 2007.

[35] R. J. Kerkman, G. L. Skibinski, D. W. Schlegel, and A. C. Drives;, "A.C. drives; Year 2000 and Beyond," in *Record of IEEE – APEC*, 1999.

[36] P. Gipe, *Wind Energy Comes of Age*. Wiley, 1995.

[37] C. G. Veinott, *Theory and Design of Small Induction Motors*. McGraw-Hill, 1959.

[38] M. G. Say, *The Performance and Design of Alternating Current Machines*. Pitman, 1958.

[39] A. K. Sawhney, *A Course in Electrical Machine Design*. Dhanpat Rai and Sons, 1984.

[40] J. Pyrhonen, T. Jokinen, and V. Hrabovcova, *Design of Rotating Electrical Machines*, 1st ed. .

[41] C. Kral, A. Haumer, M. Haigis, H. Lang, and H. Kapeller, "Comparison of a CFD Analysis and a Thermal Equivalent Circuit Model of a TEFC Induction Machine With Measurements," *IEEE Trans. Energy Con.*, vol. 24, no. 4, pp. 809–818, 2009.

[42] S. L. Ho and W. N. Fu, "Review and Future Application of Finite Element Methodes in Induction Motors," *Electr. Mach. Power Syst.*, vol. 26, no. 2, pp. 111–125, 1998.

[43] S. A. Nasar, *Handbook of Electric Machines*. McGraw-Hill, 1987.

[44] A. H. Bonnett, "A Comparison Between Insulation Systems Available for PWM-Inverter-Fed Motors," *IEEE Trans. Ind. Appl.*, vol. 33, no. 5, pp. 1331–1341, 1997.

[45] T. G. Arora, M. V. Aware, and D. R. Tutakne, "Effect of Pulse Width Modulated Voltage on Induction Motor Insulation," in *2012 7th IEEE Conference on Industrial Electronics and Applications (ICIEA)*, pp. 2044–2048, 2012.

[46] G. Mugala, R. Eriksson, and P. Pettersson, "Comparing Two Measurement

Techniques for High Frequency Characterization of Power Cable Semiconducting and Insulating Materials," *IEEE Trans. Dielectr. Electr. Insul.*, vol. 13, no. 4, pp. 712–716, 2006.

[47] M. L. Miller, "Common Characterization Techniques for Insulating Materials Used in Turbine Generators," in *EIC*, 2007.

[48] M. Sawahata, K. Nishihama, H. Mikami, and T. Fujigaki, "Magnetic Flux Density Analysis of Wound Rotor Induction Motor by Permeance Model," in *International Conference on Electrical Machines and Systems (ICEM)*, 2009, pp. 1–6.

[49] M. Birkfeld and K. A. Hempel, "Calculation of the Magnetic Behaviour of Electrical Steel Sheet Under Two Dimensional Excitation by Means of the Reluctance Tensor," *IEEE Trans. Magn.*, vol. 33, no. 5, pp. 3757–3759, 1997.

[50] M. J. Hofmann and H.-G. Herzog, "Modeling Magnetic Power Losses in Electrical Steel Sheets in Respect of Arbitrary Alternating Induction Waveforms: Theoretical Considerations and Model Synthesis," *IEEE Trans. Magn.*, vol. 51, no. 2, pp. 1–11, 2015.

[51] J. Martinez-Roman, J. Perez-Cruz, M. Pineda-Sanchez, R. Puche-Panadero, J. Roger-Folch, M. Riera-Guasp, and A. Sapena-Bano, "Electrical Machines Laminations Magnetic Properties: A Virtual Instrument Laboratory," *IEEE Trans. Educ.*, vol. 58, no. 3, pp. 159–166, Aug. 2015.

[52] M. Mochizuki, S. Hibino, and F. Ishibashi, "Application of 6.5% Silicon Steel Sheet to Induction Motor and ITS Magnetic Properties," *Electr. Mach. Power Syst.*, vol. 22, no. 1, pp. 17–29, 1994.

[53] S. W. Cheong, E. J. Hilinski, and A. D. Rollett, "Grain Growth in a Low-Loss Cold-Rolled Motor-Lamination Steel," *Met. Mat Trans A*, vol. 34, no. 6, pp. 1321–1327, 2003.

[54] S. Sprague and D. Jones, "Using the New Lamination Steels Database in Motor Design," in *Proceedings of SMMA*, pp. 1–12, 2000.

[55] R. Kimmich, M. Doppelbauer, D. T. Pefers, J. G. Cowie, and E. F. Bruvn, "Die Cast Copper Rotor Motors via Simple Substitution and Motor Redesign for Copper," in *International Conference on Electrical Machines and Systems (ICEM)*, 2006.

[56] M. G. Say, *Alternating Current Machines*. Wiley, 1976.

[57] G. Madescu, I. Boldea, and T. J. E. Miller, "An Analytical Iterative Model (AIM) for

Induction Motor Design," *IEEE Trans. Ind. App.*, vol. 23, pp. 566–573, 1996.

[58] J. Wanjiku, M. A. Khan, P. S. Barendse, and P. Pillay, "Influence of Slot Openings and Tooth Profile on Cogging Torque in Axial-Flux PM Machines," *IEEE Trans. Ind. Electron.*, vol. 62, no. 12, pp. 7578–7589, Dec. 2015.

[59] O. O. Ogidi, P. S. Barendse, and M. A. Khan, "Detection of Static Eccentricities in Axial-Flux Permanent-Magnet Machines With Concentrated Windings Using Vibration Analysis," *IEEE Trans. Ind. Appl.*, vol. 51, no. 6, pp. 4425–4434, Nov. 2015.

[60] H. Dehnavifard, M. Khan, and P. Barendse, "Development of a 5kW Scaled Prototype of a 2.5 MW Doubly-Fed Induction Generator," *IEEE Trans. Ind. Appl.*, 2016.

[61] I. Daut, K. Anayet, and S. Tirapathy, "Design and modeling of induction motor using opera 2D based on aluminum material," in *2009 3rd International Conference on Energy and Environment (ICEE)*, pp. 94–97, 2009.

[62] J.-S. Rho, C.-H. Lee, and H.-K. Jung, "Optimal Design of Ultrasonic Motor Using Evolution Strategy and Finite Element Method," *Int. J. Appl. Electromagn. Mech.*, vol. 25, pp. 699–704, 2007.

[63] L. Jun-qing and W. Xi-mei, "FEM Analysis on Interturn Fault of Rotor Wingding in DFIG," in *Electrical Machines and Systems*, pp. 797–802, 2013.

[64] Y. Duan and R. G. Harley, "A Novel Method for Multiobjective Design and Optimization of Three Phase Induction Machines," *IEEE Trans. Ind. App.*, vol. 47, no. 4, pp. 1707–1715, 2011.

[65] L. Fan, Z. Miao, L. F. Miao, Z., L. Fan, Z. Miao, L. F. Miao, and Z., *Modeling and Analysis of Doubly Fed Induction Generator Wind Energy Systems*. London: Academic Press, 2015.

[66] G. I. Vakil and K. R. Rajagopal, "Computer Aided Design of a Compact Doubly-Fed Induction Generator for Small Wind Power Application," *IEEE Trans. Ind. App.*, pp. 456–460, 2010.

[67] S. J. Chapman, *Electric Machinery Fundamentals*. McGraw-Hill, 1999.

[68] J. Martinez, A. Belahcen, and A. Arkkio, "3D Permeance Model of Induction Machines Taking into Account Saturation Effects and its Connection with Stator Current and Shaft Speed Spectra," *IET Electr. Power Appl.*, vol. 9, no. 1, pp. 20–29,

2015.

[69] J. R. Lopez, “The Effect of Induction Motor Design on Losses and Efficiency for Adjustable Frequency Drives,” *Conf. Rec. ISIE’94*, pp. 214–219, 1994.

[70] W. L. Soong, G. B. Kliman, R. N. Johnson, R. A. White, and J. E. Miller, “Novel High-Speed Induction Motor for a Commercial Centrifugal Compressor,” *IEEE Trans. Ind. Appl.*, vol. 36, no. 3, pp. 706–713, 2000.

[71] B. J. Chalmers and A. C. Williamson, *A.C. Machines*. Research Studies Press, 1991.

[72] P. C. Sen, *Principles of Electric Machines and Power Electronics*. John Wiley & Sons, 1997.

[73] T. L. Mthombeni, P. Pillay, and R. M. W. Strnat, “New Epstein Frame for Lamination Core Loss Measurements Under High Frequencies and High Flux Densities,” *IEEE Trans. Energy Con.*, vol. 22, no. 3, pp. 614–620, 2007.

[74] O. Barre and B. Napame, “Fractional Slot Concentrated Windings: A New Method to Manage the Mutual Inductance between Phases in Three-Phase Electrical Machines and Multi-Star Electrical Machines,” *Machines*, vol. 3, no. 2, pp. 123–137, 2015.

[75] B. Amin, *Induction Motors*. Springer, 2001.

[76] A. Boglietti, A. Cavagnino, and M. Lazzari, “Geometrical Approach to Induction Motor Design,” in *the 33rd Annual Conference of the IEEE Industrial Electronics Society (IECON)*, pp. 149–156, 2007.

[77] D. H. Braymer and A. C. Roe, *Rewinding Small Motors*. McGraw-Hill, 1949.

[78] M. Cistelecan and E. Demeter, “New Three-Phase A.C. Windings with Low Spatial Harmonic Content,” *Rec. Electromotion Symp.*, pp. 98–100, 1997.

[79] K. Wilkinson, *Rewinding Small Motors*. Newnes, 1965.

[80] C. I. McClay and S. Williamson, “Influence of Rotor Skew on Cage Motor Losses,” *IEE Proc. - Electr. Power Appl.*, vol. 145, no. 5, p. 414, 1998.

[81] J. Staszak, “Determination of Slot Leakage Inductance for Three-Phase Induction Motor Winding using an Analytical Method,” *Arch. Electr. Eng.*, vol. 62, no. 4, 2013.

[82] H. F. Parshall and H. M. Hobart, *Armature Windings of Electric Machines*. D. Van

Nostrand Co, 1895.

[83] M. Ruviaro, F. Runcos, N. Sadowski, and I. M. Borges, “Analysis and Test Results of a Brushless Doubly Fed Induction Machine With Rotary Transformer,” *IEEE Trans. Ind. Electron.*, vol. 59, no. 6, pp. 2670–2677, 2012.

[84] E. Abdi, M. R. Tatlow, R. A. McMahon, and P. J. Tavner, “Design and Performance Analysis of a 6 MW Medium-Speed Brushless DFIG,” in *Renewable Power Generation Conference (RPG)*, pp. 1–4, 2013.

[85] D. M. Ionel, M. V Cistelecan, T. J. E. Miller, and M. I. McGilp, “A New Analytical Method for the Computation of Airgap Reactances in Three-Phase Induction Machines,” *Rec. IEEE – IAS, Annu. Meet.*, vol. 1, pp. 65–72, 1998.

[86] T. Jokinen, “Flux Leakage,” 2008.

[87] H. Sequenz, “The Windings of Electric Machines,” in *A.C. Machines*, vol. 3, Vienna: Springer Verlag, 1950.

[88] A. R. W. Broadway, “Part–Symmetrization of Three-Phase Windings,” *IEEE Trans. Ind. App.*, vol. 12, pp. 122–125, 1975.

[89] M. V Cistelecan and E. Demeter, “A Closer Approach of the Fractional Multilayer Three-phase A.C. Windings,” *Rec. Electromotion*, vol. 1, p. 51-- 54., 1999.

[90] G. H. Rawcliffe, R. F. Burbidge, and W. Fong, “Induction-Motor Speed-Changing by Pole-Amplitude Modulation,” *Proc. IEE Part A Power Eng.*, vol. 105, no. 22, p. 411, 1958.

[91] H. Nam, S.-K. Jung, G.-H. Kang, J.-P. Hong, T.-U. Jung, and S.-M. Baek, “Design of Pole-Change Single-Phase Induction Motor for House hold Appliances,” *IEEE Trans. Ind. App.*, vol. 40, no. 3, pp. 780–788, 2004.

[92] C. Zhang, J. Yang, X. Chen, and Y. Guo, “A New Design Principle for Pole-Changing Winding-the Three-Equation Principle,” *Electr. Mach. Power Syst.*, vol. 22, no. 2, pp. 187–199, 1994.

[93] M. Poloujadoff, J. C. Mipo, and P. Siarry, “Designing 2 Pole and 2/4 Pole Windings by the Simulated Annealing Method,” *Electr. Mach. Power Syst.*, vol. 26, no. 10, pp. 1059–1066, 1998.

[94] A. S. Langsdorf, “Air-Gap Flux in Induction Motors,” *Trans. Am. Inst. Electr. Eng.*, vol. XXIV, pp. 919–931, 1905.

[95] A. Hughes, “New 3-Phase Winding of Low m.m.f. Harmonic Content,” *Proc. Inst. Electr. Eng. UK*, vol. 117, no. 8, p. 1657, 1970.

[96] N. Bianchi, S. Bolognani, and F. Tonel, “Thermal Analysis of a Run-Capacitor Single-Phase Induction Motor,” *IEEE Trans. Ind. App.*, vol. 39, no. 2, pp. 457–465, 2003.

[97] I. Boldea and S. A. Nasar, *Induction Machine Handbook*. Boca Raton, Fla: CRC Press, 1998.

[98] W. H. McAdams, *Heat Transmission*, 2nd ed. New York: McGraw Hill Inc., 1942.

[99] S. C. Mukhopadhyay and S. K. Pal, “Temperature Analysis of Induction Motors using a Hybrid Thermal Model with Distributed Heat Sources,” *J. Appl. Phys.*, vol. 83, no. 11, p. 6368, 1998.

[100] A. Boglietti, A. Cavagnino, M. Lazzari, and M. Pastorelli, “A Simplified Thermal Model for Power Derating Prediction of TEFC Induction Motors,” *Electr. Power Components Syst.*, vol. 32, no. 7, pp. 701–723, 2004.

[101] G. Bellenda, L. Ferraris, and A.Tenconi, “A New Simplified Thermal Model for Induction Motors for EVs Applications,” in *Electrical Machines and Drives*, pp. 11–13, 1995.

[102] D. Staton, A. Boglietti, and A. Cavagnino, “Solving the More Difficult Aspects of Electric Motor Thermal Analysis in Small and Medium Size Industrial Induction Motors,” *IEEE Trans. Energy Con.*, vol. 20, no. 3, pp. 620–628, 2005.

[103] A. Boglietti, A. Cavagnino, M. Popescu, and D. Staton, “Thermal Model and Analysis of Wound-Rotor Induction Machine,” *IEEE Trans. Ind. Electron.*, vol. 49, no. 5, pp. 2078–2085, 2013.

[104] A. Boglietti, A. Cavagnino, and D. A. Staton, “TEFC Induction Motors Thermal Models: A Parameter Sensitivity Analysis,” *IEEE Trans. Ind. App.*, vol. 41, no. 3, pp. 756–763, 2005.

[105] N. Christofides, “Origins of Load Losses in Induction Motors with Cast Aluminium Rotors,” *Proc. Inst. Electr. Eng. UK*, vol. 112, no. 12, p. 2317, 1965.

[106] Z. Tan, S. Member, X. Song, W. Cao, and S. Member, “DFIG Machine Design for Maximizing Power Output Based on Surrogate Optimization Algorithm,” *IEEE Trans. Energy Convers.*, vol. 30, no. 3, pp. 1154–1162, 2015.

[107] W. A. Roshen, “Magnetic Losses for Non-Sinusoidal Waveforms Found in AC

Motors," *IEEE Trans. Power Electron.*, vol. 21, no. 4, pp. 1138–1141, 2006.

[108] A. A. Jimoh, *Stray Load Losses in Induction Machines*. National Library of Canada, 1987.

[109] A. Visintin, "Mathematical Models of Hysteresis," phdthesis, University of Trieste, 2005.

[110] I. Mayergoyz, "Mathematical Models of Hysteresis," *IEEE Trans. Magn.*, vol. 22, no. 5, pp. 603–608, 1986.

[111] S. Yanase, H. Kimata, Y. Okazaki, and S. Hashi, "A Simple Predicting Method for Magnetic Losses of Electrical Steel Sheets under Arbitrary Induction Waveform," *IEEE Trans. Magn.*, vol. 41, no. 11, pp. 4365–4367, 2005.

[112] M. J. Manyage, T. L. Mthombeni, P. Pillay, and A. Boglietti, "Improved Prediction of Core Losses in Induction Motors," in *2007 IEEE International Electric Machines & Drives Conference*, pp. 531–536, 2007.

[113] M. Popescu and D. M. Ionel, "A Best-Fit Model of Power Losses in Cold Rolled-Motor Lamination Steel Operating in a Wide Range of Frequency and Magnetization," *IEEE Trans. Magn.*, vol. 43, no. 4, pp. 1753–1756, 2007.

[114] K. Roy, D. Chatterjee, and A. K. Ganguli, "Modeling and Estimation of Core Losses for Doubly-fed Wound Rotor Induction Machine," in *IEEE India Conference (INDICON)*, pp. 1–4, 2010.

[115] E. M. Olin, "Determination of Power Efficiency of Rotating Electric Machines: Summation of Losses Versus Input-Output Tests," *Proc. Am. Inst. Electr. Eng.*, vol. 31, no. 7, pp. 1287–1310, 1912.

[116] A. M. Odok, "Stray-Load Losses and Stray Torques in Induction Machines," *Trans. Am. Inst. Electr. Eng. Part III Power Appar. Syst.*, vol. 77, no. 3, pp. 43–53, 1958.

[117] S. C. Englebretson, *Induction Machine Stray Loss from Inter-Bar Currents*. 2009.

[118] P. L. Alger, G. Angst, and E. J. Davies, "Stray-Load Losses in Polyphase Induction Maclines," *Trans. Am. Inst. Electr. Eng. Part III Power Appar. Syst.*, vol. 78, no. 3, pp. 349–355, 1959.

[119] W. Cao, K. J. Bradley, and J. Allen, "Evaluation of additional loss in induction motors consequent on repair and rewinding," in *IEE Proc. Electr. Power Appl.*, pp. 1–6, 2006.

[120] W. Cao, K. J. Bradley, and A. Member, “Assessing the Impacts of Rewind and Repeated Rewinds on Induction Motors : Is an Opportunity for Re-Designing the Machine Being Wasted ?,” *IEEE Trans. Ind. App.*, vol. 42, no. 4, pp. 958–964, 2006.

[121] N. David, D. C. Aliprantis, and S. Member, “Improved Efficiency of DFIG Wind Energy Conversion Systems by Operating in the Rotor-Tied Configuration,” pp. 189–195, 2014.

[122] S. Jelassi, R. Romary, and J. F. Brudny, “Slot Design for Dynamic Iron Loss AC Rotating Electrical Machine Reduction,” in *IEEE Energy Conversion Congress and Exposition (ECCE)*, pp. 563–569, 2010.

[123] T. A. Lipo, *Introduction to AC Machine Design*, Third. Madison, USA: Wisconsin Power Electronics Research Center, University of Wisconsin, 2011.

[124] H. Dehnavifard, A. D. Lilla, M. A. Khan, and P. Barendse, “Design and optimization of DFIGs with alternate voltage and speed ratings for wind applications,” in *2014 International Conference on Electrical Machines (ICEM)*, pp. 2008–2013, 2014.

[125] A. D. Lilla, H. Dehnavifard, M. A. Khan, and P. Barendse, “Optimization of high voltage geared permanent-magnet synchronous generator systems,” in *2014 International Conference on Electrical Machines (ICEM)*, pp. 1356–1362, 2014.

[126] W. Erdman and M. Behnke, “Low Wind Speed Turbine Project Phase II : The Application of Medium-Voltage Electrical Apparatus to the Class of Variable Speed Multi-Megawatt Low Wind Speed Turbines Low Wind Speed Turbine Project Phase II : The Application of Medium-Voltage Electrical A,” San Ramon, California, techreport, 2014.

[127] A. Larsson, “The Power Quality of Wind Turbines,” phdthesis, Chalmers University of Technology, 2000.

[128] F. Watanabe and T. Uchida, “Micro-siting of Wind Turbine in Complex Terrain: Simplified Fatigue Life Prediction of Main Bearing in Direct Drive Wind Turbines,” *Wind Eng.*, vol. 39, no. 4, pp. 349–368, 2015.

[129] J. Manwell, *Wind Energy Explained*. John Wiley, 2001.

[130] T. Shanker, R. K. Singh, and M. Ieee, “Wind Energy Conversion System : A Review,” 2012.

[131] K. W. E. Cheng, J. K. Lin, Y. J. Bao, and X. D. Xue, “Review of the Wind Energy Generating System,” 2011.

[132] A. Acakpovi and E. Ben Hagan, “A Wind Turbine System Model using a Doubly-Fed Induction Generator (DFIG),” *nternational J. Comput. Appl.*, vol. 90, no. 15, pp. 6–11, 2014.

[133] Hui Li, Zhe Chen, and H. Polinder, “Optimization of Multibrid Permanent-Magnet Wind Generator Systems,” *IEEE Trans. Energy Convers.*, vol. 24, no. 1, pp. 82–92, Mar. 2009.

[134] S. Heier, *Grid Integration of Wind Energy Conversion Systems*. Chichester, UK and Kassel , Germany: John Wiley & Sons Ltd, 1998.

[135] P. J. Tavner, G. J. W. V Brussel, and F. Spinato, “Machine and Converter Reliabilities in Wind Turbines,” in *Proc. 3rd Power Electron. Mach. Drives (PEMD)*, pp. 127–130, 2006.

[136] V. Akhmatov, “Variable-speed Wind Turbines with Doubly-fed Induction Generators, Part III: Model with the Back-to-back Converters,” *Wind Eng.*, vol. 27, no. 2, pp. 79–91, 2003.

[137] S. Muller, M. Deicke, and R. DeDoncker, “Adjustable Speed Generators for Wind Turbines based on Doubly-fed Induction Machines and 4- Quadrant IGBT Converters Linked to the Rotor,” *IEEE Trans. Ind. App.*, vol. 2, 2000.

[138] Mohan N., T. M. Undeland, and W. P. Robbins, *Power Electronics: Converters, Applications and Design*. Oxford, UK: Clarendon Press, 1989.

[139] P. Alemi and D.-C. Lee, “Power Loss Comparison in Two and Three-Level PWM Converters,” in *ECCE*, 2011.

[140] W. Song, X. Feng, and K. M. Smedley, “A Carrier-Based PWM Strategy With the Offset Voltage Injection for Single-Phase Three-Level Neutral-Point-Clamped Converters,” *IEEE Trans. Power Electron.*, vol. 28, no. 3, pp. 1083–1095, 2013.

[141] J. S. Kim and S. K. Sul, “New Control Scheme for AC–DC–AC converter without DC link Electrolytic Capacitor,” in *PESC’93*, 1993, pp. 300–306.

[142] A. Schuster, “A Matrix Converter without Reactive Clamp Elements for an Induction Motor Drive System,” in *PESC’s*, 1998, pp. 714–720.

[143] P. W. Wheeler and D. A. Grant, “A Low Loss Matrix Converter for AC Variable-speed Drives,” in *EPE 5th European Conference on Power Electronics and Application*, 1993, vol. 5, pp. 27–32.

[144] J. Rodriguez, L. Moran, A. Gonzalez, and C. Silva, “High Voltage Multilevel Converter with Regeneration Capability,” in *PESC’s 99*, vol. 2, pp. 1077–1082.

[145] M. Alatalo, “Permanent Magnet Machines with Air Gap Windings and Integrated Teeth Windings,” Sweden, techreport, 1996.

[146] A. J. Mitcham and N. Grum, “An Integrated LP Shaft Generator for the more Electric Aircraft,” in *IEE Coloquium on All Electric Aircraft*, 1998, p. 8/1--8/9.

[147] “U.S. Small Wind Turbine Market: 2014 summary report,” New York, techreport, 2015.

[148] A. M. Alkandari, S. A. Soliman, and M. H. Abdel-rahman, “Steady State Analysis of a Doubly Fed Induction Generator,” vol. 2011, no. September, pp. 393–400, 2011.

[149] A. Perdana, “Dynamic Models of Wind Turbines A Contribution towards the Establishment of Standardized Models of Wind Turbines for Power System Stability Studies,” phdthesis, CHALMERS UNIVERSITY OF TECHNOLOGY, 2008.

[150] M. Ali, I.-S. Ilie, J. V Milanovic, and G. Chicco, “Wind Farm Model Aggregation Using Probabilistic Clustering,” *IEEE Trans. Power Syst.*, vol. 28, no. 1, pp. 309–316, 2013.

[151] B. Kivido, “Grid Integration of Wind Energy Systems,” phdthesis, University of Cape Town, 2014.

[152] M. R. Islam and M. R. I. Sheikh, *Enhancement of Power System Stability by Using DFIG Based Wind Farm*, 1st ed. Saarbrücken: LAP LAMBERT Academic Publishing, 2014.

[153] G. Abad, *Doubly Fed Induction Machine*. Wiley, 2011.

[154] H. Sterling, “Harmonic Field Effects in Induction Machines,” *Electron. Power*, vol. 23, no. 10, p. 841, 1977.

[155] L. Lin, “Effect of Wind Farm Based-on Wound Rotor Induction Generator on Transient Characteristics of Transmission Grid,” 2009.

[156] V. Rana and M. A. Ansari, “Wind Farm Integration Effect on Electricity Market Price,” in *ECCE*, pp. 349–354, 2013.

[157] S. Dakai, “Discussion of Wind Farm Integration in China,” techreport, 2005.

[158] G. Saccomando, J. Svensson, and A. Sannino, “Improving Voltage Disturbance

Rejection for Variable-Speed Wind Turbines," *IEEE Power Eng. Rev.*, vol. 22, no. 7, p. 53, 2002.

[159] "An Aggregated Model of a Grid-connected, Large-scale, Offshore Wind Farm for Power Stability Investigations Importance of Windmill Mechanical System," *Electr. Power Energy Syst.*, vol. 24, no. 9, pp. 709–717, 2002.

[160] J. Juang and Y.-C. Huang, *Intelligent Technologies and Engineering Systems*. Springer, 2013.

[161] F. Jurado, L. M. Ferna, and J. R. n Saenz, "Aggregated Dynamic Model for Wind Farms with Doubly Fed Induction Generator Wind Turbines," *Renew. Energy*, vol. 33, pp. 129–140, 2008.

[162] N. Jenkins, "Engineering Wind Farms," *Power Eng. J.*, vol. 4, pp. 53–60, 1993.

[163] J. R. Kristoffersen and P. Christiansen, "Horns Rev Offshore Wind Farm: Its Main Controller and Remote Control System," *Wind Eng.*, vol. 27, no. 5, pp. 351–360, 2003.

[164] D. Yang, L. Ban, Z. Xiang, N. Du, B. Zheng, and Z. Wu, "An Aggregation Method of Wind Farm Model for Electromagnetic Transient Simulation Analysis," pp. 4–8, 2012.

[165] M. A. Chowdhury, N. Hosseinzadeh, M. M. Billah, and S. A. Haque, "Dynamic DFIG Wind Farm Model with an Aggregation Technique," in *6th International Conference on Electrical and Computer Engineering ICECE 2010*, no. December, pp. 18–20, 2010.

[166] V. Akhmatov, "An Aggregated Model of a Large Wind Farm with Variable-speed Wind Turbines Equipped with Doubly-fed Induction Generators," *Wind Eng. Press*, 2004.

[167] S. J. G., S. W. H. de Haan, H. Polinder, and K. W., "Aggregated Modelling of Wind Parks with Variable Speed Wind Turbines in Power System Dynamics Simulations," in *the 14th Power Systems Computation Conference*, 2002.

[168] P. Sørensen, B. Bak-Jensen, J. Kristian, A. D. Hansen, L. Janosi, and J. Bech, "Power Plant Characteristics of Wind Farms," in *in Wind Power for the 21st Century*, 2000.

[169] J. G. Slootweg, H. Polinder, and W. L. Kling, "Dynamic Modeling of a Wind Turbine with Doubly Fed Induction Generator," in *IEEE Power Eng. Soc. Summer Meeting*, 2001.

[170] A. Trzynadlowski, *The Field Orientation Principle in Control of Induction Motors*. Kluwer Academic, 1994.

[171] P. S. Barendse, “Design and Implementation of Variable Speed Induction Generator For Wind Energy System,” phdthesis, University of Cape Town, 2004.

[172] K. Hamann, “Field Orientated Control of an Induction Motor,” University of Cape Town, 1999.

[173] P. M. Anderson and A. A. Fouad, *Power System Control and Stability*. IEEE Press, 2003.

[174] B. M. Wilamowski and J. D. Irwin, *Power Electronics and Motor Drives*. CRC Press, 2011.

[175] P. Vas, *Sensorless Vector and Direct Torque Control*. London: Oxford University Press, 1998.

[176] C. Batlle, A. Dòria-Cerezo, and E. Fossas, “Modeling, Simulation and Control of a Doubly-Fed Induction Machine,” *Proc. Appl. Math. Mech.*, vol. 7, no. 1, pp. 3030003–3030004, 2007.

[177] J. B. Ekanayake, S. Member, L. Holdsworth, X. Wu, N. Jenkins, and S. Member, “Dynamic Modeling of Doubly Fed Induction Generator Wind Turbines,” *IEEE Trans. POWER Syst.*, vol. 18, no. 2, pp. 803–809, 2003.

[178] S. Vicatos, A. Tegopoulos, M. S. Vicatos, J. A. Tegopoulos, S. Vicatos, and A. Tegopoulos, “Transient State Analysis of a Doubly-Fed Induction Generator under Three Phase Short Circuit,” *IEEE Trans. Energy Con.*, vol. 6, no. 1, pp. 62–68, Mar. 1991.

[179] S. J. Chapman, *Electric Machinery and Power System Fundamentals*. McGraw-Hill, 2002.

[180] R. H. Park, “Two-Reaction Theory of Synchronous Machines Generalized Method of Analysis-Part I & II,” *Trans. Am. Inst. Electr. Eng.*, vol. 48, no. 3, pp. 716–727, 1929.

[181] R. Solomon, M. A. Khan, P. S. Barendse, P. Pillay, and K. A. Folly, “Review and Application of Micromachines for Wind Energy Integration,” *IEEE Int. Conf. Electr. Mach.*, pp. 2151–2157, 2012.

[182] H. R and L. L. Freris, “Micromachine Simulation of Steam Power Plant,” *Proc. IEE*,

vol. 121, no. 6, p. 491499, 1974.

[183] M. E. Newton and B. W. Hogg, “Optimal Control of a Micro-Alternator System,” *IEEE Trans. Power Appar. Syst.*, vol. 95, no. 6, pp. 1822–1833, 1976.

[184] M. P. Kostenko and I. D. Ursav, “Electromagnetic Models of the Kyibyshew Power Station,” *Elektrichstro*, vol. 8, pp. 781–795, 1955.

[185] S. H. Kia, H. Henao, S. Member, and G. Capolino, “Windings Monitoring of Wound Rotor Induction Machines under Fluctuating Load Conditions,” pp. 3459–3465, 2011.

[186] “Induction Motor Laboratory.”

[187] Standards Coordinating Committee 21, “IEEE Standard Test Procedure for Polyphase Induction Motors and Generators,” 2004.

[188] R. Pena, R. Cardenas, and G. Asher, “Overview of Control Systems for the Operation of DFIGs in Wind Energy Applications,” in *IECON 2013 - 39th Annual Conference of the IEEE Industrial Electronics Society*, pp. 88–95, 2013.

12. Appendices

Appendix A

A reference DFIG is employed in chapter 3. Appendix A presents the reference DFIG's design details with relevant equations.

Table 1 The reference DFIG design details

Specification	Formula	Quantity
Power[MW]	P	2.5
Efficiency[%]	η	95.8
Voltage[V]	V_{SN}	690
Poles	$2.p_1$	4
Phase	m	3
Speed[rpm]	n_{1N}	1500
Frequency[Hz]	f_1	50
Max Slip	S_{max}	±0.25
Electromagnetic power[MW]	$S_{gN} = \frac{Power}{0.96}$	2.604
Stator power[MW]	S_{SN}	2
Rotor power[MW]	$S_{RN} = S_{SN}\lvert S_{max}\rvert$	0.5
Stator Design		
Electromagnetic Torque[kN.m]	$T_e = \frac{S_{gN}}{2\pi\frac{f_1}{p_1}(1+\lvert S_{max}\rvert)}$	13.27
The shear rotor stress [N/cm^2]	$1.5 < f_{xt} < 6$	6
Stack length ratio	$\lambda = \frac{l_i}{D_{is}}; 0.2 < \lambda < 1.5$	1
Stator Internal Diameter[m]	$D_{is} = \sqrt[3]{\frac{2 \times T_e}{\pi \times \lambda \times f_{xt}}}$	0.52
Stator Outer Diameter[m]	$D_{out} = 1.48\,.D_{is}$	0.796
Rated stator current[A]	$I_{SN} = \frac{S_{SN}}{\sqrt{3}V_{SN}}$	1675.46
Airgap flux density[T]	B_{g1}	0.75
Pole pitch[m]	$\tau = \frac{\pi D_{is}}{2p_1}$	0.4
Stator winding factor	$K_{W1} = \frac{sin\frac{\pi}{6}}{q_1 sin\frac{\pi}{6q_1}} sin\frac{\pi}{2}\frac{y}{\tau}$ $q_1 = 5$ (slot per pole per phase) $\frac{y}{\tau}$: the stator coil span/pole pitch ratio $\frac{2}{3} \le \frac{y}{\tau} \le 1$	0.9097

Number turn per current path (rough calculation)	$W_{1a} = \frac{K_E \frac{V_{SN}}{\sqrt{3}}}{2\sqrt{2} f_1 W_1 K_{W1a} B_{g1} \tau l_i}$ $K_E = 0.97\ (0.97 < K_E < 0.98)$ $a_1 = 2$ (current path)	19.32
Number of turn per coil	$n_{c1} = \frac{W_1}{\left(\frac{2p_1 q_1}{a_1}\right)}$	2
Number turn	$W_1 = \frac{2p_1}{a_1} q_1 n_{c1}$	20
Stator slot pitch[m]	$\tau_s = \frac{\pi D_{is}}{m 2 p_1 q_1}$	0.0266
Stator number of slot	$N_s = 2 p_1 q_1 m$	60
Stator conductor cross section[mm^2]	$A_{cos} = \frac{I_{SN}}{a_1 . j_{cos}}$ $j_{COS} = 6.5\ [\frac{A}{mm^2}]$ (assumed current density)	128.88
Stator slot width[m]	$W_S = 0.5\ \tau_s$	0.01333
Stator useful slot area[mm^2]	$A_{su} = \frac{2 n_{c1} A_{cos}}{k_f}$ $k_f = 0.55$ (assumed filling factor)	937
Stator useful slot height[mm]	$h_{su} = \frac{A_{su}}{1000 * W_S}$	70.315
Arigap[mm]	$g = (0.1 + 0.012\sqrt[3]{S_{Sn}})10^{-3}$	1.6
Stator back iron core[m]	$h_{cs} = \frac{B_g \tau}{\pi B_{cs}}$ $B_{cs} = 1.55\ [T]$ (assumed stator core flux density)	0.0637
Outer diameter[m]	$D_{outm} = D_{is} + 2(h_{sm} + h_{sw} + h_{cs})$	0.7997~0.8
Cross section area of elementary conductor[mm^2]	$A_{cose} = \frac{A_{cos}}{4}$ Number of elementary conductor=4	32.2
Height of elementary conductor[mm^2]	$h_{ce} = \frac{A_{cose}}{a_{ce}}$ $a_{ce} = 12[mm]$, (width of elementary conductor) $m_e = 16$ (number of layers elementary conductors)	2.68
Skin Effect		
B[m^{-1}]	$\beta = \sqrt{\frac{\omega_1 \mu_0 \sigma_{co}}{2} \frac{a_{ce}}{W_S}}$ $\omega_1 = 2\pi . f_1$ $\mu_0 = 1.256 \times 10^{-6}$ $\sigma_{co} = 4.3 \times 10^7$	69.64
ξ (unnamed in the reference)	$\xi = \beta \times h_{ce}$	0.1866

Skin effect coefficient (for 16 layers elementary conductor)	$K_{Rme} = \varphi(\xi) + \frac{m_e^2 - 1}{3}\psi(\xi)$ $\varphi(\xi) = \xi\frac{sinh2\xi + sin2\xi}{cos2h\xi - cos\xi} = 1$ $\psi(\xi) = 2\xi\frac{(sinh\xi + sin\xi)}{cosh\xi + cos\xi} = 5.55 \times 10^{-4}$	1.04675
Additional skin effect	$K_{Rad} = 4\beta^4.h_{ce}^4(\frac{l_i}{l_{turn}})^2 n_{cn}^2\frac{(1+cos\gamma)^2}{4}$ l_{turn}: coil turn length $\gamma = \left(1 - \frac{y}{\tau}\right)\frac{\pi}{2} = 0\ (for\ dimentional\ coil)$	0.01847
Total skin effect factor	$K_R = 1 + (K_{rme} - 1)\frac{l_{stack}}{l_{turn}} + K_{Rad}$	1.03717
Rotor Design		
Turn ration	$K_{RS} = \frac{W_2 K_{W2}}{W_1 K_{W1}} = \frac{1}{\lvert S_{max}\rvert}$	4
Stator current reduced to rotor side[A]	$I'_{SN} = \frac{I_{SN}}{K_{RS}}$	418.865
Rotor-reduced magnetizing current[A]	$I'_m = K_m I'_{SN}$	125.6595
Rotor current at max slip[A]	$I_{RN}^R = \sqrt{I'^2_{SN} + I'^2_m}$	437.3
Rotor power factor	$cos\varphi_{2N} = \frac{P_{RN}}{\sqrt{3}\,V_{RN} I_{RN}^R}$	0.9578
Rotor winding factor	$K_{W2} = \frac{sin\frac{\pi}{6}}{q_2 sin\frac{\pi}{6q_2}} sin\frac{\pi}{2}\frac{y_R}{\tau}$ $q_2 = 4$ (Rotor slot per phase per pole)	0.925
Rotor number of slot	$N_r = 2p_1 q_2 m$	48
Rotor turns per phase	$W_2 = \frac{W_1 K_{W1} K_{RS}}{K_{W2}}$	78.53~80
Number of turn per coil for rotor	$n_{c2} = \frac{W_2}{\left(\frac{2p_1 q_2}{a_2}\right)}$ $a_2 = 1$ (rotor current path)	5
Rotor slot pitch[m]	$\tau_R = \frac{\pi D_{is}}{m_1 2p_1 q_2}$	0.033805
Rotor conductor cross section[mm^2]	$A_{cor} = \frac{I_{RN}}{a_2.j_{cos}}$ $j_{cor} = 8\ [\frac{A}{mm^2}]$ (assumed current density)	43.4
Rotor slot width[m]	$W_R = 0.45\ \tau_R$	0.0152
Rotor useful slot area[mm^2]	$A_{ru} = \frac{2n_{c2}A_{cor}}{k_f}$ $k_f = 0.55$ (assumed filling factor)	789.09
Rotor useful slot height[mm]	$h_{RU} = \frac{A_{ru}}{1000 * W_R}$	51.913

Minimum rotor teeth width[mm]	$W_{tRmin} = \frac{\pi(D_{is} - 2(g + h_{RU} + h_{RW}))}{N_R} - W_R$	11.42
Maximum rotor teeth flux density[T]	$B_{tRmax} = \frac{B_{g1}\tau_R}{W_{tRmin}}$	2.22
Rotor back iron radial path[m]	$h_{CR} = \frac{B_g \tau}{\pi B_{cr}}$ $B_{cr} = 1.6[T]$ (assumed rotor core flux density)	0.0597~ 0.06
Inner diameter[m]	$D_{IR} = D_{IS} - 2(g + h_{SU} + h_{RW} + h_{CR})$	0.287
Magnetization Current		
Carter Coefficient	$K_C = K_{C1}K_{C2}$ $K_{C1,C2} = \frac{1}{1 - \gamma_{1,2}\frac{g}{2\tau_{s,r}}}; K_{C1} = 1.0826, K_{C2} = 1.04$ $\gamma_{1,2} = \frac{\left(\frac{2W_{S',R'}}{g}\right)^2}{5 + \frac{2W_{S',R'}}{g}}$ $W_{S'} = \frac{W_S}{\mu_{RS}} = \frac{13.2}{3} = 4.066$ $W_{R'} = \frac{W_R}{\mu_{RR}} = \frac{15.2}{5} = 3.04$	1.126
Airgap mmf [A.turns]	$F_{AA'} = gK_C\frac{B_{g1}}{\mu_0}$	1083.86
Stator teeth mmf [A.turns]	$F_{AB} = H_{ts}(h_{su} + h_{sw})$ $B_{ts} = B_{g1} \times \frac{\tau_S}{W_{ts}} = 1.49[T]$ $H_{ts} = 1290\ [A/m]$	94.62
Stator back iron mmf [A.turns]	$F_{BC} \approx H_{cs}.l_{csav}$ $(l_{csw})_{BC} \approx \frac{2}{3}\frac{\pi(D_{out} - h_{cs})}{2.2p_1} = 0.19266\,m$ $H_{cs} = 1340[A/m]$	258.17
Rotor teeth mmf [A.turns]	$F_{A'B'} = H_{tr}(h_{RU} + h_{RW})$ $B_{trt} = B_{g1} \times \frac{\tau_R}{W_{tR}} = 1.3629[T]$ $B_{tRm} = B_{g1} \times \frac{\tau_R}{W_{tRm}} = 1.69[T]$ $B_{tRb} = B_{g1} \times \frac{\tau_R}{W_{tR}} = 2.2[T]$ $B_{tR} = \frac{B_{tRt} + B_{tRb} + 4B_{tRm}}{6} = 1.72[T]$ $H_{tr} = 5334\ [A/m]$	292.34
Rotor back iron mmf [A.turns]	$F_{B'C'} = H_{CR}.l_{CRav}$ $l_{CRav} = \frac{2}{3}\frac{\pi\left(D_{shaft} + h_{CR} + 0.01\right)}{2.2p_1} = 0.19266\,m$ $H_{CR} = 2460[A/m]$	216.92

Total magnetization mmf [A.turns]	$F_m = \frac{3W_2K_{W2}I_{R0}\sqrt{2}}{\pi p_1} = (F_{AA'} + F_{AB} + F_{BC} + F_{A'B'} + F_{B'C'}$	1946.40
No-load rotor current[A]	$I_{R0} = F_m \frac{\pi . p_1}{3W_2 . K_{W2}\sqrt{2}}$ $K_m = \frac{I_{R0}}{I'_{SN}} = 0.09322$ (compare it with assumed K_m)	39.05
Saturation factor[%]	$K_S = \frac{F_{AB} + F_{BC} + F_{A'B'} + F_{B'C'}}{F_{AA'}}$	79
Reactances and Resistances		
Magnetization Inductance[mH]	$L_m = \frac{6\mu_0(W_{1a}K_{WS})^2\tau l_i}{\pi^2 p_1 g K_C(1+K_S)}$	8.0428
Magnetization Reactance[Ω]	$X_m = \omega_1 L_m$	2.582
Base reactance[Ω]	$X_b = \frac{V_{SN}}{I_{SN}}$	0.238
Magnetization Reactance[p.u.]	$x_m = \frac{X_m}{X_b}$	10.85
Stator end connection[m]	$l_{fs} = 2(l_l + l_{l'}) + \pi h_{st} = 2\left(l_l + \frac{\beta_s \tau}{2cos\alpha}\right) + \pi h_{ts}$ l_l= 0.015 [m] $\beta_s = \frac{y}{\tau} = \frac{12}{15}$ $h_{ts} = 0.07035\ [m]$ (diameter of end connection) α=40°	0.668
Stator resistance[Ω]	$R_S = \rho_{co100°} \frac{W_{1a}.2}{A_{cos}}(l_i + l_{fs})\frac{1}{a_1}$	0.429×10^{-2}
Stator leakage inductance[mH]	$L_{sl} = \mu_0(2n_{c1})^2 l_i(\lambda_s + \lambda_{end} + \lambda_{ds})\frac{N_s}{m_1 {a_1}^2}$ The slot coefficient, $\lambda_s = \frac{h_{su}}{3W_s} + \frac{h_{sw}}{W'_s} = 7.852$ The end connection coefficient, $\lambda_{end} = 0.34q_1\frac{l_{fs} - 0.64\beta_s\tau}{l_i} = 1.5143$ The differential geometrical permeance $\lambda_{ds} = 0.9\tau_s\,(q_1K_{W1})^2\,K_{01}\frac{\sigma_{ds}}{K_C g} = 1.127$ $K_{01} = 1 - 0.033\left(\frac{W'_S}{g\tau_s}\right) = 0.9873$	0.257×10^{-3}
Stator leakage reactance[Ω]	$X_{sl} = \omega_1 L_{sl}$	0.0823
Rotor end connection[m]	$l_{fr} = 2\left(l_l + \frac{\beta_r \tau}{2cos\alpha}\right) + \pi(h_{RU} + h_{RW})$ $l_l = 0.015\ [m]$	0.6375

	$\beta_r = \frac{y}{\tau} = \frac{10}{12}$ $\alpha = 40°$	
Rotor resistance[Ω] (reduced to rotor side)	$R_R^r = \rho_{co100°} \frac{W_2.2}{A_{cor}} (l_i + l_{fs})$	83.8×10^{-3}
Rotor leakage inductance[mH] (reduced to rotor side)	$L_{rl}^r = \mu_0 (2n_{c2})^2 l_i (\lambda_{SR} + \lambda_{endR} + \lambda_{dR}) \frac{N_R}{m}$ The slot coefficient, $\lambda_s = \frac{h_{RU}}{3W_R} + \frac{h_{RW}}{W_R'} = 2.1256$ The end connection coefficient, $\lambda_{endR} = 0.34 q_2 \frac{l_{fr} - 0.64\beta_R \tau}{l_i} = 1.1093$ The differential geometrical permeance $\lambda_{dR} = 0.9\tau_R (q_2 K_{W2})^2 K_{02} \frac{\sigma_{dR}}{K_C g} = 1.413$ $K_{02} = 1 - 0.033 \left(\frac{W_R'}{g\tau_R}\right) = 0.994$	4.858
Rotor leakage reactance[Ω] (reduced to rotor side)	$X_{rl}^r = \omega_1 {L_{rl}}^r$	1.525
Rotor resistance[Ω]	$R_R = \frac{R_R^r}{K_{RS}^2}$	5.24×10^{-3}
Rotor leakage inductance[mH]	$L_{Rl} = \frac{L_{Rl}^r}{K_{RS}^2}$	0.303
Rotor leakage reactance[Ω]	$X_{Rl} = \frac{X_{Rl}^r}{K_{RS}^2}$	0.0953
Stator copper losses[kW]	$P_{cos} = 3 \times K_R R_S I_{SN}^2$	37.47
Rotor copper losses[kW]	$P_{cor} = 3 \times R_R^r I_{RN}^2$	48.075
Sliprings losses[kW]	$P_{sr} = 3 V_{SR} I_R^r$ The voltage drop along brushes is $V_{SR} = 1V$	1.3119
Stator back iron weight[kg]	$G_{cs} \approx \pi (D_{out} - h_{cs}) \times h_{cs} \times l_i \times \gamma_{iron}$	582
Stator teeth weight[kg]	$G_{ts} = \left\{ \frac{\pi}{4} \left[\left(D_{is} + 2(h_{su} + h_{sw})\right)^2 - D_{is}^2 \right] - N_s \times (h_{su} + h_{sw}) \times W_s \right\} l_i \gamma_{iron}$	313.8
Stator core losses[kW]	$P_{irons} = P_{\frac{10}{50}} \left(\frac{f_1}{50}\right)^{1.5} \left(K_t B_{ts}^2 G_{ts} + K_y B_{cs}^2 G_{cs}\right)$ $P_{\frac{10}{50}} = 3[\frac{W}{kg}]$ $K_t = 1.6$ $K_y = 1.3$	8.442
Rotor core losses[kW]	$P_{ironr} < S_{max}^2 P_{irons}$	0.527
Total losses[kW]	$\sum P_e = P_{cos} + P_{cor} + P_{irons} + P_{ironr} + P_{ad} + P_{sr}$ $P_{add} = 10\ [kW]$	101.2

Efficiency[%]	$\eta_e = \frac{P_{SN} + P_{RN}}{P_{SN} + P_{RN} + \sum P_e}$	95.8

Appendix B

The micro-DFIG's structural profiles for the stator, the rotor and the shaft are presented in Fig. 1, 2 and 3.

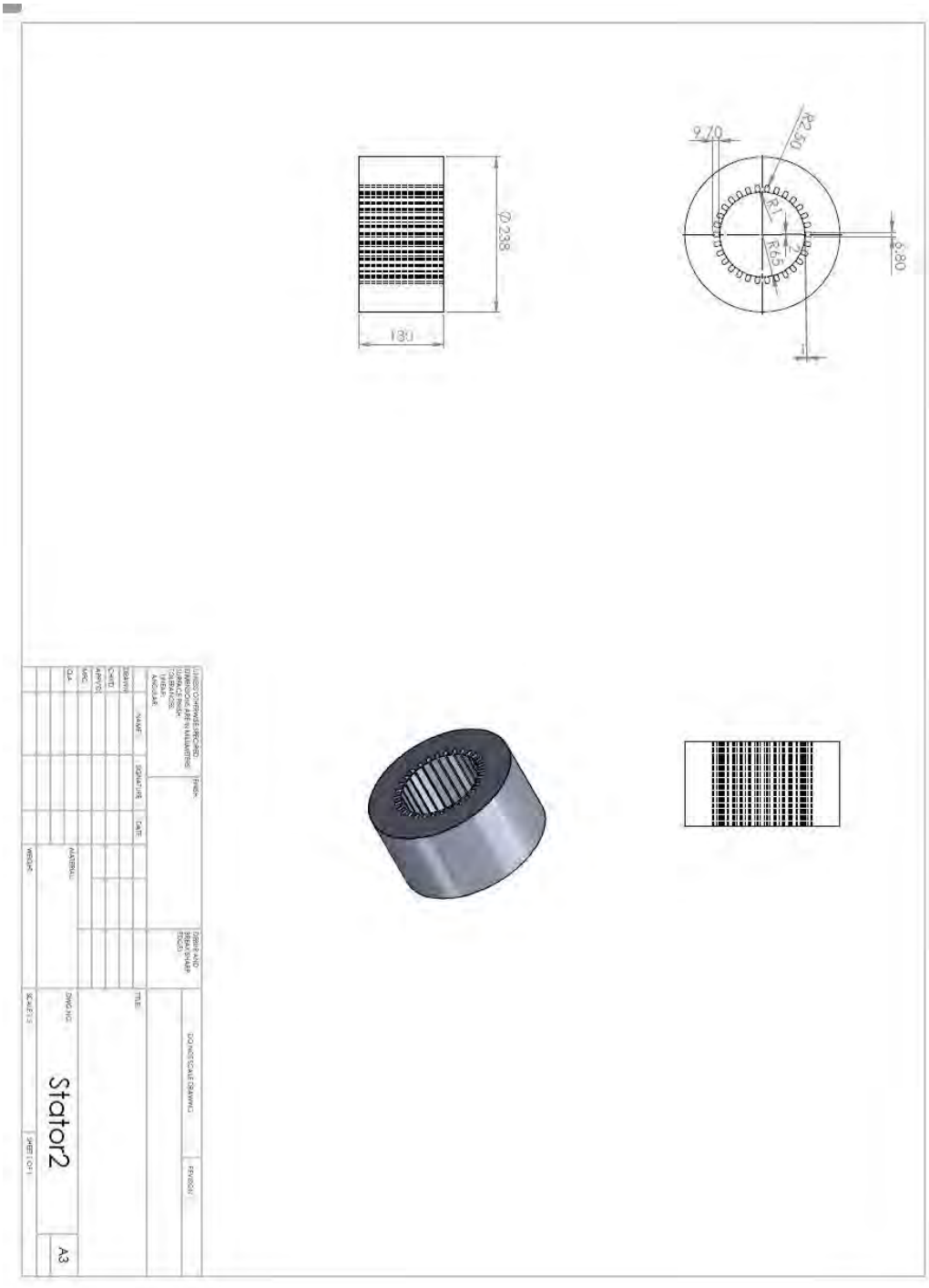

Figure 1 The micro-DFIG 2D and 3D stator sketch.

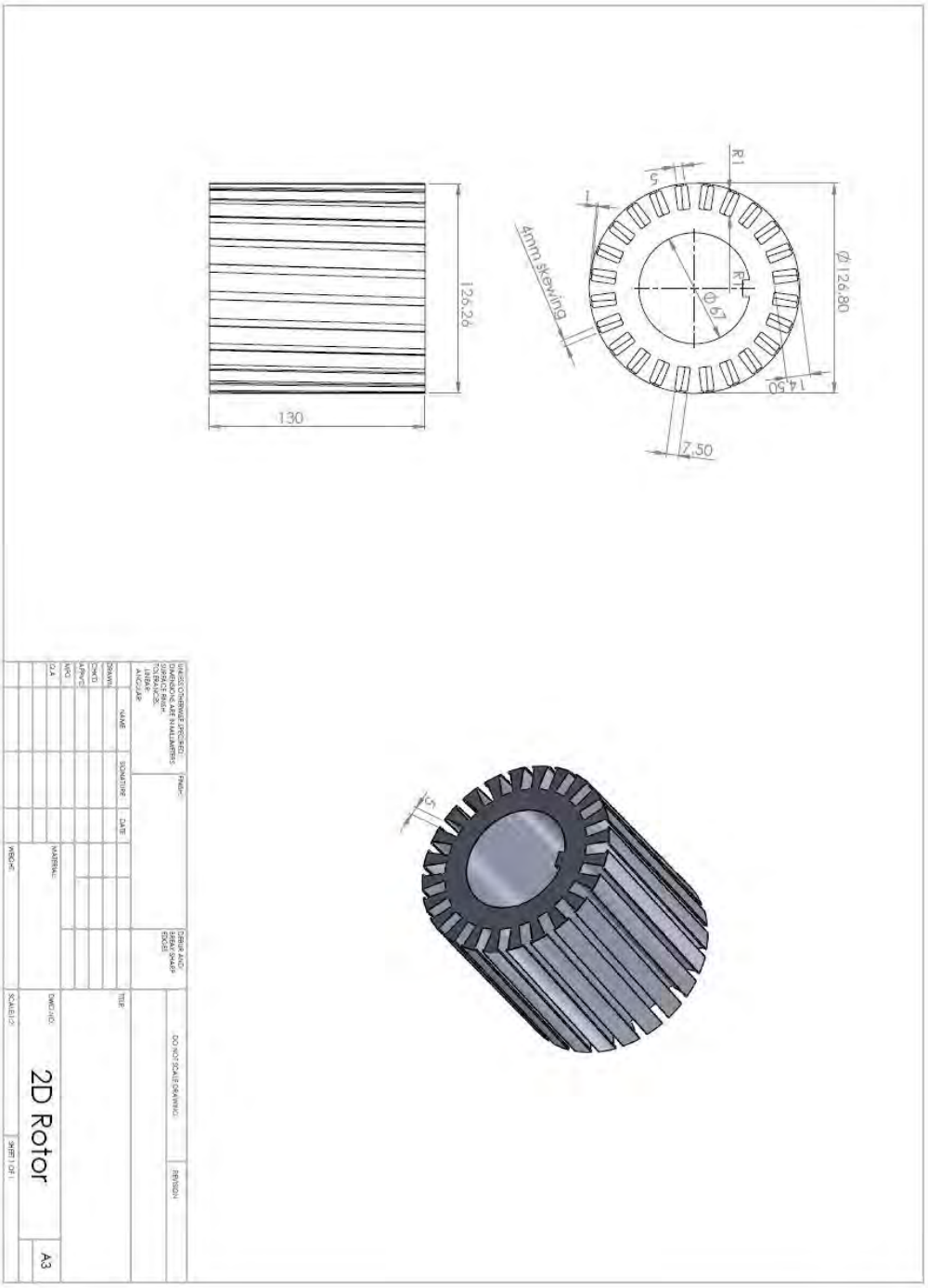

Figure 2 The micro-DFIG 2D and 3D rotor sketch.

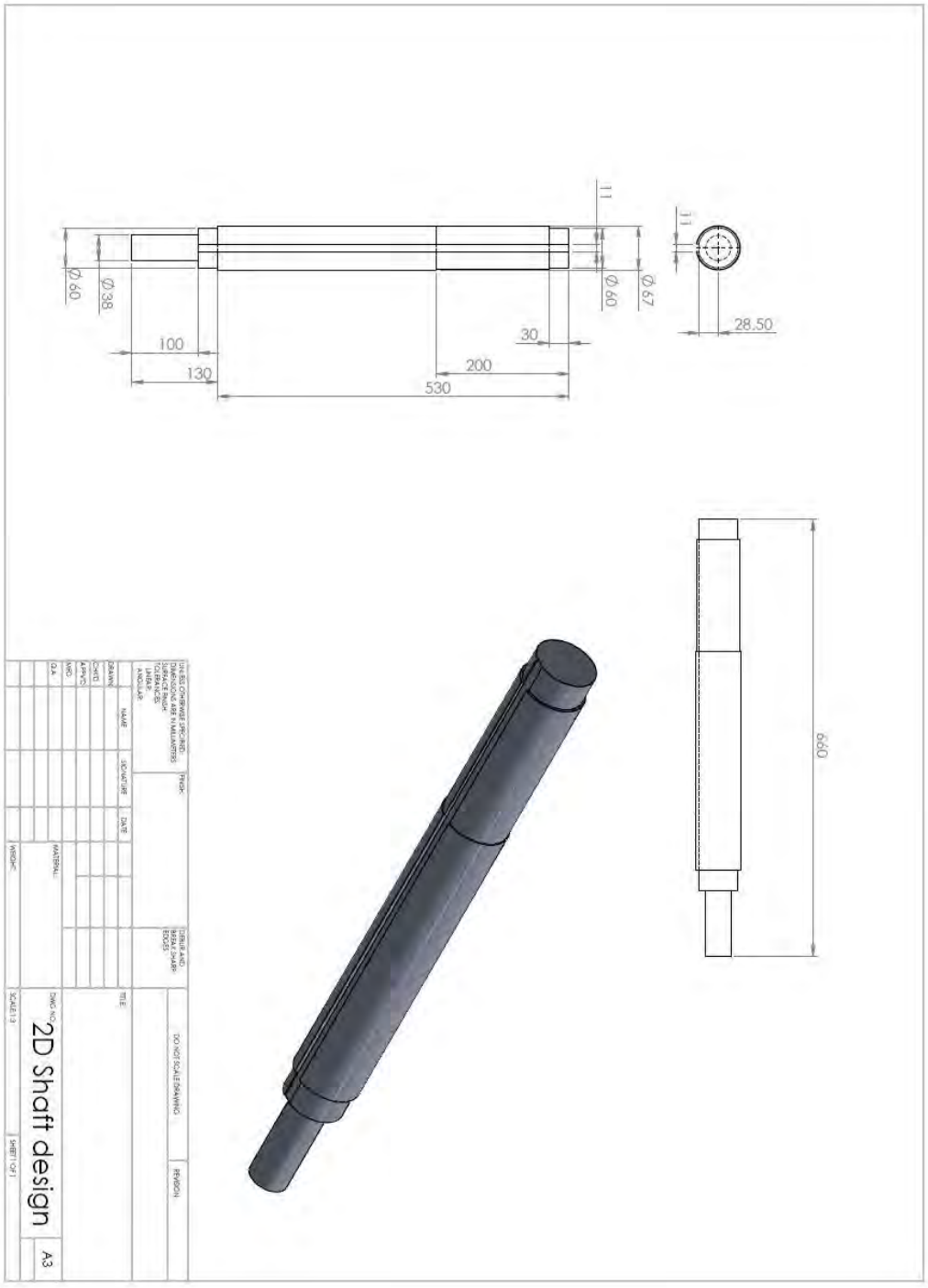

Figure 3 The micro-DFIG 2D and 3D shaft sketch.

Appendix C

SURA M530-65A silicon-steel is used to laminate the micro-DFIG's cores and the lamination thickness is 0.5mm. Table 1 presents the loss details of SURA M530-65A silicon-steel at 50Hz.

Table 2 SURA M530-65A silicon-steel loss details at 50Hz

Flux density[T]	[W/kg]	[VA/kg]	[A/m]
0.1	0.02	0.08	39.2
0.2	0.11	0.23	53.2
0.3	0.23	0.41	62.9
0.4	0.38	0.62	71.5
0.5	0.56	0.86	79.8
0.6	0.76	1.14	88.5
0.7	0.98	1.46	97.8
0.8	1.24	1.82	108
0.9	1.53	2.25	120
1.0	1.85	2.76	134
1.1	2.12	3.41	156
1.2	2.62	4.28	195
1.3	3.07	5.65	271
1.4	3.63	8.66	466
1.5	4.26	18.46	1085
1.6	4.97	49.01	2750
1.7	5.59	115	5797
1.8	6.10	226	10270

Table 2 shows the magnetic details of SURA M530-65A silicon-steel.

Table 3 SURA M530-65A silicon-steel magnetic details

Magnetic polarization at 50Hz	
H = 2500 A/m, [T]	1.59
H = 5000 A/m, [T]	1.68
H = 10000 A/m, [T]	1.79
Coercivity (DC) [A/m]	60
Relative permeability at 1.5 T	1110
Resistivity [μΩcm]	38
Yield strength [N/mm²]	285
Tensile strength [N/mm²]	430
Young's modulus, RD[11], [N/mm²]	190000
Young's modulus, TD[12], [N/mm²]	210000
Hardness HV5 (VPN)	145

[11] Rolling Direction
[12] Transverse Direction